Laser ablation of dentin and its medical application

Quang Tri Le

THÈSE EN COTUTELLE PRÉSENTÉE

POUR OBTENIR LE GRADE DE

DOCTEUR DE

L'UNIVERSITÉ DE BORDEAUX

ET DE ET DE L'INSTITUTO SUPERIOR TÉCNICO DE

L'UNIVERSITÉ DE LISBONNE

ÉCOLE DOCTORALE DES SCIENCES CHIMIQUES

SPÉCIALITÉ PHYSICO-CHIMIE DE LA MATIÈRE CONDENSÉE

Par Quang Tri LE

LASER ABLATION OF DENTIN AND ITS MEDICAL APPLICATION

Sous la direction de Caroline BERTRAND et de Rui VILAR

Soutenue le 21 Mars 2017

Membres du jury :

M.LOPES Luís Miguel Pires	Professeur, Universidade de Lisboa	Président
M. MONTEIRO Fernando Jorge Mendes	Professeur, Universidade do Porto	Rapporteur
M. OLIVEIRA Victor Manuel Barbas	Professeur, Instituto Superior de Engenharia de Lisboa	Rapporteur
Mme BERTRAND Caroline	Professeur, Université de Bordeaux	Directeur de thèse
Mme POULON-QUINTIN Angéline	Professeur, Université de Bordeaux	Examinateur
Mme ALMEIDA Maria Amélia Martins de	Professora Auxiliar, Instituto Superior Técnico, Universidade de Lisboa;	Examinateur
Mme BRULAT-BOUCHARD Nathalie	Maître de Conférences des Universités, , Université Nice Sophia Antipolis	Examinateur

Titre : Ablation laser de la dentine et ses applications medicales

Résumé :

Le développement récent, dans le domaine de la santé, de lasers femtoseconde pompés par diode, délivrant des impulsions de forte énergie et utilisés en chirurgie (en particulier en ophtalmologie), nous amene à chercher de nouveaux domaines d'application dans le secteur de la santé. En effet, la durée très brève de l'interaction laser avec la matière (de l'ordre de 10^{-15}s) et les fortes intensités de radiation délivrées, permettent d'envisager une ablation tissulaire rapide avec des effets thermiques négligeables.

Objectif

Ce travail va un triple objectif:

- Etudier la capacité d'ablation de l'émail dentaire et de la dentine avec un laser femto seconde,
- Mesurer l'accroissement de température généré par l'interaction laser/tissus avec et sans spray d'air + eau, sachant qu'un accroissement de température au delà de 5.5°C engendre des dommages irréversibles (nécrose) du tissu pulpaire.
- Mener une étude comparative de l'adhésion des matériaux de restauration composite sur les surfaces préparées par laser versus l'adhésion sur des surfaces dentinaires préparées de façon conventionnelle avec une fraise et une turbine.

Matériels et méthode

Cette étude est réalisée sur des molaires humaines saines fraichement extraites pour des raisons parodontales. Chaque molaire est découpée sous forme de disques d'émail et de dentine qui sont ensuite traités avec un laser Yb: KYW, à une longueur d'onde de 1030nm et 560fs et à différentes valeurs de fluences.

La caractérisation en microstructure et en composition chimique des surfaces dentaires est étudiée en microscopie électronique à balayage (MEB), en diffraction des rayons X (DRX), en spectroscopie

Raman et en spectroscopie infrarouge à transformée de Fourrier (IRTF). L'accroissement de température généré par le tir laser au sein de la dent, avec puis sans spray d'air et irrigation d'eau, est mesuré à l'aide de thermocouple et d'électrodes placées in situ dans la racine dentaire jusqu'au plafond de la chambre pulpaire.

L'adhésion d'un matériau d'obturation composite sur les surfaces dentaires traitées par laser d'une part et par traitement conventionnel (fraise+turbine) d'autre part, est évaluée par des tests de cisaillement. Un adhésif (Adhese Universal ® de la société Ivoclar-Vivadent ©, Liechtenstein) est appliqué soit directement sur chaque surface dentaire traitée ou immédiatement après l'application d'un gel de mordançage à l'acide orthophosphorique à 32%.

Résultats

La caractérisation en microstructure des surfaces amélaires traitées au laser avec une fluence comprise entre 4 à 14 J/cm^2 et des fréquences de répétition de 1 à 1000Hz révèle une fonte des tissus amélaires en surface. L'épaisseur de cette couche tissulaire solidifiée est très fine (1.5µm). La microstructure et la composition des tissus situés immédiatement sous cette couche solidifiée ne sont pas modifiées.

Les surfaces dentinaires préparées avec des fluences situées entre 2 et 14 J/cm^2 et des fréquences de répétition de 1 à 1000Hz ne présentent aucun signe de matériau re-solidifié en surface. Les tubuli dentinaires sont clairement exposés et visibles. L'analyse en spectroscopie infrarouge (IRTF) ne montre aucune modification de la composition chimique de la dentine par rapport à la dentine non traitée.

La température intra pulpaire mesurée pendant le traitement laser atteint des valeurs de l'ordre de 17.5°C quand le traitement par laser est réalisé avec une fluence de 14 J/cm^2, avec une fréquence de 1kHz pendant une durée de 240s. L'application d'un spray d'air et eau combinés permet de réduire de façon significative la température in situ (6.6°C).

L'absence de boue dentinaire et la préservation des tubuli dentinaires ouverts au cours du traitement laser facilite la pénétration de l'adhésif qu'il y ait eu ou non un mordençage préalable à l'acide ortho-phosphorique. Les valeurs de cisaillement obtenues sont similaires quel que soit le mode de préparation des surfaces (laser ou fraise). Cependant, dans le cas où le mordançage n'a pas été réalisé au préalable sur les surfaces traitées avec une fraise carbure de tungstène sur contre-angle, les valeurs d'adhésion chutent. La persistance de boue dentinaire s'oppose à la formation de la couche hybride faite d'un entrelacement de fibres de collagène et de polymères de résine.

Les résultats de ce travail ont permis une meilleure compréhension du mécanisme d'ablation des tissus durs dentaires par le laser femtoseconde.

Conclusion

L'ablation de l'émail, matériau homogène, se produit grâce à un mécanisme photo-thermique qui produit un échauffement rapide des tissus à haute température puis une phase d'explosion tissulaire. Par contre, l'ablation de la dentine, matériau composite alliant des nanocristaux d'OH apatite et un réseau de fibres collagènes, se traduit, même à basse fluence, par une ablation des fibres collagènes, entrainant une perte de cohésion tissulaire. Le mécanisme qui prévaut dans ce cas n'est plus photo-thermique comme pour l'émail mais photo-mécanique.

Malgré la nature athermique de l'interaction laser femtoseconde - matériau, l'utilisation d'un spray d'air et eau concomitant sera obligatoire pour éviter tout risque d'accroissement de température excessif lors des traitements dentaires et leurs effets délétères.

Mots clefs : laser – femtoseconde – tissus durs – caractérisation – adhésion – température pulpaire.

Title : Laser ablation of dentin and its medical application

Abstract

Recent development has led to the commercialization of high power femtosecond lasers, opening a new perspective into the field of laser surgery. Due to the short laser – material interaction time and the very high radiation intensity achieved with this type of laser, the ablation of a wide range of materials can be achieved with negligible thermal effects.

Objectives

The present work aims at

- Studying the ablation of dental enamel and dentin by femtosecond laser
- Measuring the increase of pulpal temperature generated during the laser treatment without external cooling and with external cooling using an air jet and a combination of the air jet and water irrigation.
- Comparing the adhesion of restorative materials to dentin surface treated by the laser and by the conventional drilling method with a burr.

Materials and methods

This study was performed on human third molars which were recently extracted by clinical procedure. Enamel and dentin disks were cut from the teeth and polished by SiC papers.

A Yb:KYW chirped-pulse-regenerative amplification laser system with 560 fs pulse duration and 1030 nm radiation wavelength was used. The laser experiments were performed with pulse repetition rates and radiation fluences in the ranges 1 – 1000 Hz and 2 – 14 J/cm^2, respectively, in stationary and non-stationary modes. The laser treatments were performed in air without external cooling, and with surface cooling methods with an air jet and with a combination of the air jet and water irrigation. Temperature in the pulpal chamber of the tooth was measured during the laser treatments.

The ablation surfaces were analyzed by scanning electron microscope (SEM), Fourier transform infrared spectroscopy (FTIR), microRaman spectroscopy and grazing incidence X-ray diffraction (GIXRD) methods. The adhesion of dental restorative adhesive to dentin surfaces treated by the femtosecond laser and by the conventional method with a tungsten carbide burr was studied by shear tests. The laser treatments were performed at 1 kHz pulse repetition rate and fluences of 2 and 14 J/cm^2. The adhesive (Adhese Universal ®, Vivoclar Vivadent ©, France) was bonded directly to dentin surfaces or after etching dentin surface by an etchant gel containing 32 wt% phosphoric acid.

Results

The surface characterization shows that laser treated enamel surface is covered by resolidified material, even with fluences just above the ablation threshold. At 1 kHz, the ablation surface is covered by a significant amount of redeposited ablation debris, which could be removed by ultrasonication. The microRaman results indicate that the redeposited debris consist mainly of amorphous calcium phosphate (ACP), probably formed by the rapid resolidification of the calcium phosphate droplets ejected in the liquid state.

On the contrary, dentin surfaces treated within the tested range of processing parameters present no sign of resolidified material. At 1 kHz, a large amount of resolidified droplets is observed on the laser treated surfaces, but the dentin surface exposed after ultrasonication show no signs of resolidified material. In addition, the tubules remain open. FTIR analysis confirms that the chemical constitution of dentin at the treated surface is not significantly affected by the laser treatment. Despite the lack of thermal effects in the ablation of dentin, heating of the tooth bulk was observed by the measurement of pulpal temperature. The tested cooling methods allow reducing significantly the temperature rise without affecting the ablation rate.

The absence of the smear layer and the opening of the tubules allow the infiltration of the adhesive resin in the laser treated dentin surfaces even when bonding was performed without etching.

Comparable shear strength values were obtained for specimens bonded with etching, regardless of the surface preparation method (laser or burr). However, lower shear strength values were obtained when the adhesive was bonded to dentin surfaces prepared with a burr without a prior etching step. This result is explained by the presence of a smear layer at burr-cut dentin surface, which prevents the formation of the smear plugs and a strong hybrid layer.

Conclusion

The results indicate that the ablation of enamel by femtosecond laser is predominated by photothermal mechanism, which involves rapid heating of the tissue to temperatures near its critical point, followed by the ablation by either liquid spallation or phase explosion processes. On the contrary, the ablation of dentin is influenced by the ablation of collagen fibrils at low fluences, leading to a reduction of the cohesive strength of the tissue. Consequently, the ablation of the dentin is predominated by a photomechanical mechanism (solid spallation). Thanks to this ablation mechanism, the constitution and structure of dentin are not significantly affected by the laser treatment. Consequently, the laser treated dentin surfaces can promote strong adhesion to the restorative adhesive even when bonded without etching, on the contrary to the case of dentin surfaces prepared by conventional drilling. Despite the lack of major thermal damage induced in dental tissues during the femtosecond laser treatment, the use of air-water cooling is necessary during prolonged treatment, especially when high fluences and high repetition rates are used, to avoid excessive heating of the tooth.

Keywords: Femtosecond laser; dental hard tissues; laser – induced modifications; adhesion; surface characterization

Résumé :

Les récents développements dans le domaine des lasers femto-secondes ont ouvert la voie de leur utilisation dans le domaine de la santé, en particulier en ophtalmologie et en chirurgie. En effet, la durée très brève de l'interaction laser-matière (de l'ordre de 10^{-15}s) et les fortes intensités de radiation délivrées, permettent d'envisager une ablation tissulaire rapide avec des effets thermiques négligeables.

Objectif

Les objectifs de ce travail de thèse sont :

- Etudier la capacité d'ablation de l'émail dentaire et de la dentine avec un laser femto seconde.
- Mesurer l'accroissement de température générée par l'interaction laser/tissus avec et sans projection du mélange air + eau, sachant qu'un accroissement de température au delà de 5.5°C engendre des dommages irréversibles du tissu pulpaire (nécrose).
- Mener une étude comparative de l'adhésion des matériaux de restauration composite sur les surfaces préparées par laser par rapport à l'adhésion sur des surfaces dentinaires préparées de façon conventionnelle (fraise + turbine).

Matériaux et méthodologie

Cette étude est réalisée sur des molaires humaines saines fraichement extraites pour des raisons parodontales. Le protocole clinique a été approuvé par un comité d'éthique et est enregistré sous la référence DC 2014/04. Les disques d'émail et de dentine ont été séparés des dents et polis à l'aide de papiers SiC.

Un laser Ytterbium femtoseconde avec une durée d'impulsion de 560 fs et une longueur d'onde de 1030 nm a été utilisé durant ce travail de thèse. Les expériences laser ont été effectuées avec des fréquences d'impulsions et de fluences de rayonnement respectivement de 1 à 1000 Hz et de 2 à 14 J/cm^2 en mode stationnaire et non-stationnaire. Les traitements au laser ont été effectués dans l'air ambiant sans refroidissement externe, ainsi qu'avec des méthodes de refroidissement de surface

type « jet d'air » et « jet d'air +eau ». L'élévation de la température, générée par le tir laser au sein de la dent, est mesurée à l'aide de thermocouples et d'électrodes placés in situ dans la racine dentaire jusqu'au plafond de la chambre pulpaire.

Les caractérisations microstructurales et chimiques des surfaces dentaires sont étudiées en microscopie électronique à balayage (MEB), en diffraction des rayons X (DRX), en spectroscopie microRaman et en spectroscopie infrarouge à transformée de Fourrier (IRTF). L'adhésion d'un matériau d'obturation composite sur les surfaces dentaires est évaluée par des tests de cisaillement. Ces matériaux ont été traités par laser d'une part, et par traitement conventionnel (fraise + turbine) d'autre part. Les traitements au laser ont été effectués à une fréquence d'impulsions de 1 kHz et des fluences de 2 et 14 J/cm^2. Un adhésif (Adhese Universal ® de la société Ivoclar-Vivadent ©, Liechtenstein) est appliqué soit directement sur chaque surface dentaire traitée ou immédiatement après l'application d'un gel de mordançage à l'acide phosphorique à 32%. 10 échantillons ont été préparés pour chaque condition de traitement. L'interface adhésif - dentine dans les échantillons collés a été étudiée par MEB.

Résultats

Les valeurs de seuil d'impulsion de 2.72 et 1.49 J / cm^2, calculées par la méthode D^2, sont obtenues respectivement pour l'émail et la dentine. Les seuils d'ablation de ces tissus diminuent avec le nombre croissant d'impulsions laser, ce qui indique l'influence des effets d'incubation pouvant être expliqués par la génération de défauts chimiques et/ou structurels dans le matériau même à des fluences inférieures au seuil d'ablation. Les niveaux d'énergie de ces défauts se situent dans le gap électronique des matériaux et peuvent ainsi augmenter l'absorption des impulsions laser suivantes. Le facteur d'incubation, qui caractérise l'effet d'incubation, a été déterminé dans cette étude respectivement à 0.74 et 0.79 pour l'émail et la dentine.

Les images MEB des surfaces d'émail traitées avec des fluences comprises entre 4 et 14 J/cm^2 à une fréquence d'impulsion de 1 Hz montrent la formation d'une couche de matériau resolidifée. À 1 kHz,

les effets thermiques jouent un rôle plus important dans le processus d'ablation de l'émail, ce qui conduit à l'éjection d'une plus grande quantité de gouttelettes resolidifiées s'accumulant dans des grappes de taille micrométrique, redéposées ensuite à la surface. Les éléments redéposés peuvent être enlevés par ultrasons, révélant la couche de matériau resolidifiée en dessous. Dans l'échantillon traité avec 14 J / cm^2 à 1 kHz, la couche de matériau resolidifiée observée au MEB présente une épaisseur maximale de 1.5 µm. Les résultats de l'analyse microRaman et DRX montrent que la constitution de l'émail sous-jacente à cette couche n'est pas affectée de manière significative. Les résultats de microRaman montrent également que les débris déposés sont principalement constitués de phosphate de calcium amorphe (ACP), probablement formés par la solidification rapide des gouttes de phosphate de calcium éjectées durant l'ablation.

Les surfaces dentinaires préparées avec des fluences entre 2 et 14 J/cm^2 à des fréquences de répétition de 1 à 1000Hz ne présentent quant à elles aucun signes de matériau re-solidifié en surface. A une fréquence d'impulsions de 1 kHz, une grande quantité de gouttelettes resolidifiées et agrégées en grappes de diamètre de plusieurs micromètres est observée sur les surfaces des dentines traitées au laser, Les débris déposés sont à nouveau essentiellement des ACP, tels qu'analysés par IRTF. Dans ce cas, lasurface de la dentine exposée après ultrasons ne présente aucuns signes de matériau resolidifié et les tubuli dentinaires sont clairement exposés et visibles. Les résultats d'IRTF ne montrent aucune modification de la composition chimique de la dentine par rapport à la dentine non traitée.

Malgré le peu d'effet thermique durant l'ablation, la température intra pulpaire mesurée pendant le traitement laser atteint des valeurs de l'ordre de 17.5°C pour des traitements de 14 J/cm^2 à 1kHz pendant une durée de 240s. L'augmentation de la température est significativement réduite par l'utilisation d'un refroidissement de surface de type « jet d'air » (ΔT = 10.5 ° C) ainsi qu'avec une combinaison de jet d'air et d'irrigation d'eau (ΔT = 6.6 ° C). L'utilisation du refroidissement par air conduit à la formation d'une couche compacte formée par les gouttelettes resolidifiées, couvrant la

structure dentaire sous-jacente. Les débris d'ablation redéposés sont également observés dans le cas du refroidissement air-eau, mais avec une quantité nettement inférieure. Pour les deux méthodes de refroidissement externe, les débris peuvent être facilement enlevés par ultrasons et la surface exposée ne montre aucune altération significative que ce soit dans la structure ou dans la constitution de la dentine.

L'absence de boue dentinaire et la préservation de l'ouverture des tubuli dentinaires au cours du traitement laser facilite la pénétration de l'adhésif qu'il y ait eu ou non un mordançage préalable à l'acide ortho-phosphorique. Les valeurs de cisaillement obtenues sont similaires quel que soit le mode de préparation des surfaces (laser ou fraise). Cependant, dans le cas où le mordançage n'a pas été réalisé au préalable sur les surfaces traitées à l'aide d'une fraise, les valeurs d'adhésion chutent. La persistance de boue dentinaire s'oppose donc à la formation de la couche hybride faite d'un entrelacement de fibres de collagène et de polymères de résine.

Conclusion

Les résultats de ce travail de thèse ont permis une meilleure compréhension du mécanisme d'ablation des tissus durs dentaires par laser femtoseconde. L'ablation de l'émail, matériau homogène, se produit grâce à un mécanisme photo-thermique qui produit un échauffement rapide des tissus à haute température puis une phase d'explosion tissulaire. Par contre, l'ablation de la dentine, matériau composite alliant des nanocristaux d'hydroxyapatite et un réseau de fibres collagènes, se traduit, même à basse fluence, par une ablation des fibres de collagènes entrainant une perte de cohésion tissulaire. Le mécanisme qui prévaut dans ce cas n'est plus photo-thermique comme pour l'émail mais photo-mécanique. En raison de ce mécanisme d'ablation, la structure et la constitution de la dentine ne sont pas significativement affectés par le traitement laser. Par conséquent, les surfaces de dentine traitées au laser peuvent favoriser une meilleure adhérence à l'adhésif réparateur, même lorsqu'appliqué sans gravure, contrairement au cas des surfaces de dentines préparées par forage conventionnel. Malgré le manque de dommages thermiques majeurs

induits lors du traitement laser dans les tissus dentaires, l'utilisation du refroidissement air-eau est nécessaire lors d'un traitement prolongé, en particulier lorsque des fluences élevées et des taux de répétition élevés sont utilisés pour éviter un échauffement excessif de la dent.

Mots clefs : laser – femtoseconde – tissus durs – caractérisation – adhésion – température pulpaire.

Acknowledgement

I am truly grateful for the guidance and support from my supervisors Prof. Rui Vilar at the Instituto Superior Tecnico, Universidade de Lisboa and Prof. Caroline Bertrand at the University Bordeaux. I have been able to learn a lot from their knowledge and their passion for research.

I am also grateful for the helps from Dr. Vitor Oliveira for countless help with the femtosecond laser used in the present work, and with the software used to control it.

I would like to thank Prof. Luis Santos for the permission to perform the microRaman and Fourier transform infrared (FTIR) spectroscopy analysis.

I would like to thank Dr. Thierry Cardinal for receiving me in his group at the Institut de Chimie de la Matière Condensée de Bordeaux.

A special thanks to Dr. Angeline Poulon for the countless help with the equipment and for the fruitful discussions during my stay in Bordeaux.

I would also like to thank Prof. Lionel Canioni and Prof. Jean-Luc Battaglia for their advice on the temperature measurements.

I would like to thank Dr. Clemens Hoenninger and Amplitude Systèmes©, France, for the cooperation in this project.

I would like to thank Ms. Isabel Nogueira for the countless help with the scanning electron microscope (SEM) instrument as well as with the sample preparation.

I would like to acknowledge the help from Mrs. Sylvie Zeboulon at 3M Deutschland GmbH, Germany and Mr. Chakik Taleb at Ivoclar Vivadent ©, Liechtenstein, for the supply of the acid etchants, the dental restorative materials and the LED device used in the present work.

I am truly grateful for the opportunities to meet many wonderful friends during the course of my PhD. In particular, I would like to express my gratitude towards my friends Liliana Cangueiro, Bruno Nunes, Eduardo Amaro, Liu Tomin, Nguyen Tuyen, Dao Thi Phuong Tuyen, Lo Nhat Truong as well as to my flatmates.

A huge thanks to my wonderful family, who have always been by my side and showed me great support during my endeavor. I would like to specially thank my parents and my beloved wife, who have always trusted my every decision and allowed me to be myself whenever I am with them.

List of figures

List of tables

List of symbols and abbreviations

α	X-ray beam angle of incidence of radiation in the grazing incidence mode	[°]
λ	Radiation wavelength	[nm]
I_0	Intensity of the incident X-ray beam	W/m^2
θ	Angle of incidence	[°]
w_0	The beam spot radius at $1/e^2$ of its maximum intensity	[μm]
K	Thermal conductivity	$[m^2/s]$
μ_e	Electron mobility	$[cm^2/(Vs)]$
ν_e	Electron collision rate	$[s^{-1}]$
F_a	Average laser radiation fluence	$[J/cm^2]$
F_0	Peak laser fluence	$[J/cm^2]$
τ_{th}	Thermal diffusion time	[s]
τ_p	Laser pulse duration	[s]
c_p	Heat capacity	[J/kg/K]
c_s	Speed of sound in the material	$[ms^{-1}]$
D	Ablation crater´s diameter	[μm]
L_p	Laser penetration depth	[m]
D_T	Thermal diffusivity	$[m^2s^{-1}]$
E_P	Laser pulse energy	[J]
F_e	Electrostatic force	[N]
c	Light velocity	$[3*10^8$ m/s]
n	Refractive index	
f	Laser pulse repetition rate	[Hz]
E_g	Band gap energy	eV

E	Electric field	$V.m^{-1}$
l_s	Thickness of the skin layer	m
k	Extinction coefficient	
ω	Frequency of electromagnetic field	Hz
τ_s	Characteristic time of mechanical equilibration of the absorbing volume	s
N	Number of laser pulses	
S	Incubation coefficient	
dw	Lateral displacement between the linear tracks	μm
l_{focal}	Focal length of lens	mm
r_a	Ablation rate	μm^3/pulse
v	Specimen´s moving velocity	mm/s
V_a	Ablation volume	μm^3
L_{track}	Length of the linear track	μm
d_{hkl}	Interplanar distance between planes in the {hkl} family	nm
λ_{laser}	Wavelength of the excitation laser used for Raman spectroscopy	cm
$\lambda_{scatterd}$	Wavelength of the Raman-scattered radiation	cm
$\Delta\tilde{\nu}_{Raman}$	Raman shift	cm^{-1}
NA	Numerical aperture	
w_{Raman}	Diameter of the excitation laser beam in Raman spectroscopy	μm
$d_{analysis}$	Depth of analysis	μm
rpm	Round per minute	
Nd:YAG	Neodymium-doped Yttrium Aluminium Garnet	

Er:YAG	Erbium-doped Yttrium Aluminium Garnet	
ArF	Argon fluoride	
KrF	Krypton fluoride	
Yb:KYW	Potassium Yttrium Tungstate doped with Ytterbium	
HEMA	Hydroxyethyl Methacrylate	
D3MA	Decandiol Dimethacrylate	
Bis-GMA	Bisphenol A glycidyl methacrylate	
HA	Hydroxyapatite	
ACP	Amorphous calcium phosphate	
CW	Continuous wave	
DTGS – TEC	Deuterated triglycine sulfate – thermoelectricity cooled	
FWHM	Full width at half maximum	
GI-XRD	Grazing incidence X-ray Diffraction	
FTIR	Fourier transform infrared spectroscopy	
IR	Infrared	
RT	Room temperature	[^{o}C]
SEM	Scanning Electron Microscope	
UV	Ultraviolet	
10-MDP	10-methacryloxydecyl dihydrogen phosphate	

Table of contents

Introduction

Since the construction of the first laser by Maiman T.[1] in 1960, many potential application of lasers have been studied, among which, laser dental surgery is one of the most important. The idea was initially suggested recognizing the potential of lasers to drill and cut materials without significant thermal damage to the remaining material, and on the ability to focus the laser beam into a very small spot, suitable for high accuracy operation. The first investigations were performed using pulsed ruby lasers with a radiation wavelength of 0.6943 μm (unspecified pulse duration) in 1964 [2,3]. No sensation of pain or thermal effects were reported[2,3]. Further investigations performed with various types of laser sources with radiation wavelength within the spectral range 0.193 μm (ArF laser[4]) to 10.6 μm (CO_2 laser[5]), and with pulse duration within the range from a few milliseconds (ms) to a few nanoseconds (ns). Among the laser sources tested, CO_2 (wavelength 9.3 – 10.6 μm[5]), Nd:YAG (wavelength 1064 nm[6]), Er:YAG (2.940 μm[7]), and Er, Cr:YSGG (2.780 μm[8]) attracted special attention due to the overlapping of their radiation wavelengths with an absorption band of hydroxyapatite (CO_2, Er:YAG and Er, Cr:YSGG) or water (Nd:YAG, Er:YAG and Er, Cr:YSGG).

For CO_2 and Nd:YAG lasers with pulse duration within the range 10^{-3} – 10^{-9} s, the material removal rates achieved are low and ablation is accompanied by heating, often leading to tissue melting, carbonization, thermomechanical cracking and, in extreme cases, necrosis[6]. These results are explained by the laser – material interaction time sufficiently long to transfer a significant amount of heat to the material. On the contrary, Er:YAG and Er, Cr:YSGG lasers allow achieving relatively high material removal rates while avoiding significant thermal damage, making them the main types of lasers used in clinical applications. The absence of major thermal damage is explained by the fact that their wavelengths are within a very strong absorption band of water. Consequently, their radiation is efficiently absorbed by the water contained in the tissue, which warms up and boils explosively, leading to the mechanical disruption of the tissue[6,8]. With this ablation mechanism, the heat transferred to the tooth bulk is minimal. However, for certain processing parameter ranges, the

shockwave created by the rapid evaporation of water can lead to sub – superficial cracks, which reduce significantly the tissue's mechanical strength[9].

Another approach to reduce thermal effects is by using UV lasers[4,10–12]. The energy of the UV photons is sufficiently high to break the covalent bonds in the organic compounds of the tissues, allowing their ablation by a photochemical mechanism, as opposed to the photothermal mechanism associated with the IR lasers[11,13]. The lack of thermal effects in the ablation of dental tissues was confirmed by the surface characterization results reported for the laser treatment of enamel and dentin by ArF (193 nm radiation wavelength, 10 – 23 ns pulse duration)[4,12] and KrF (248 nm radiation wavelength, 30 ns pulse duration)[11,13] excimer lasers. However, excimer lasers are not suitable for clinical application due to their low ablation rate and the potential health hazard caused by exposure to intense UV radiation.

A more effective method to reduce thermal effects is by using ultrafast lasers. With the development of chirped pulse amplification (CPA) technique, it is possible to achieve laser source with pulse duration in the femtosecond regime and high peak power. For such short pulse durations, the interaction time is shorter than the characteristic energy relaxation times such as the electron-lattice energy transfer time and heat conduction time[14]. Therefore, no energy is transferred to the lattice during the laser pulse and most of the absorbed radiation energy is spent on the ablation process and carried away by the ablated material. Moreover, since absorption of femtosecond pulse duration radiation by the dental hard tissues is highly non-linear, the interaction zone is confined to a very small region, similar to the focal volume, allowing the treatments to be performed with high precision. The characterization of the surface of hard tissues, such as enamel[15,16], dentin[17–21] and bone[14,20,22,23] treated by this type of lasers, shows negligible thermal and thermomechanical degradation of the underlying tissue. Lorenzo et al.[24] report that the enamel surfaces treated by a Ti:sapphire laser with 795 nm radiation wavelength and 120 fs pulse duration can promote higher adhesion strengths to the orthodontic brackets than in the cases of Er:YAG laser treatment. In

addition, the energy efficiency and material removal rates of hard tissues achieved with ultrashort pulse lasers are higher than those obtained with nanosecond pulse duration infrared[15,25] and UV lasers[26]. Even though the results with dental tissues are promising for the application in dental caries removal treatment, detailed studies on the ablation mechanisms and on the laser – induced morphological and constitutional modifications of the hard tissues are still lacking. In addition, the adhesion of dental restorative adhesive to laser – treated tissue surfaces needs to the investigated.

In the present work, the ablation of enamel and dentin, two main components of the human teeth, by a near infrared femtosecond laser was studied for the application in dental caries removal treatments. The surface morphology and chemical constitution of the laser treated tissues surfaces were investigated for a wide range of laser processing conditions, allowing information regarding the ablation mechanisms to be obtained. In addition, the adhesion of dental restorative adhesives to the laser treated dentin surfaces was studied and compared to that of dentin surfaces prepared by the conventional drilling method with the tungsten carbide burr.

The thesis is organized as follows:

- **Chapter 1** introduces the major scientific concepts involved in the present work. The structure and composition of human teeth are described, followed by a review on the methods used in clinical dental caries removal treatments, and on the interaction between dental restorative adhesives and tissues surfaces. The theoretical background of the interaction between the ultrashort pulse laser radiation and dielectric materials as well as organic materials is also described in this chapter.
- **Chapter 2** describes the femtosecond laser set-ups, the methods to determine the laser beam diameter and the ablation threshold of the tissues and the laser processing methods used in this thesis. Finally, the surface characterization techniques and the related instruments used are presented.

- **Chapter 3** presents the experimental results obtained in the present work. The ablation thresholds of enamel and dentin obtained with a Yb:KYW laser (560 fs, 1030 nm) were determined. The morphological and constitutional modifications of enamel and dentin induced by the laser treatments were studied for a wide range of processing parameters. The increase of temperature in the tooth pulpal chamber during the laser treatments and the influence of external cooling were also studied. Finally, the adhesion of a self-etch restorative adhesive to the laser treated dentin surfaces was investigated and compared with the adhesion to dentin surfaces prepared by the tungsten carbide burr.
- **Chapter 4** presents a discussion on the experimental results obtained in this work. The evolution of the ablation thresholds of dentin and enamel with the number of laser pulses is explained and the obtained values are compared with the values reported in the literature. The surface characterization results are interpreted and related to the ablation mechanisms of the tissues. The adhesion tests results are discussed to evaluate the potential of femtosecond laser in dental caries removal treatment. Finally, the influence of external cooling in the ablation of dentin is discussed.
- **Chapter 5** presents the conclusion of this thesis and suggestions for future work.

1. Literature review

In this chapter, scientific knowledge crucial for the understanding of this work is introduced. The major concepts are presented as followed:

- Structure and chemical constitution of human enamel and dentin.
- The formation of dental caries and its effects on human teeth.
- Caries removal methods currently used in clinical practice, with the focus on mechanical drilling and laser – based techniques.
- Adhesion of dental restorative adhesives to dentin surfaces after the caries removal treatment.
- The ablation mechanisms of dielectric materials and organic matters by ultrashort pulse lasers.
- Potential of ultrashort pulse lasers in caries removal treatment.

1.1. Structure and chemical constitution of human teeth

A schematic diagram of the structure of a human molar is presented in Figure 1.1. A human tooth consists of two main parts: a crown, which stays above the gum and protrudes into the mouth, and a root, which extends into the gum and is firmly held in the sockets in the jaw thanks to periodontal ligaments[27]. The crown, the main focus of the present study, has two main components: enamel and dentin. Enamel, which consists mainly of hydroxyapatite, forms a protective coating with high resistance against wear to protect the underlying dentin and the pulp[28]. Dentin contains similar inorganic components as enamel, but with a higher amount of organic matter, mainly type I collagen, and water. This tissue possesses higher toughness than enamel and can provide mechanical support for the outer layer[29]. Deep inside the tooth is the pulp chamber containing mostly odontoblast cells, which are responsible for the biological processes leading to the formation of dentin, nerves and blood vessels[30–32].

In principle, the chemical composition of the inorganic components in dentin and enamel slightly deviates from that of pure hydroxyapatite ($Ca_5(PO_4)_3(OH)$) due to the partial substitution of hydroxyl and phosphate ions by CO_3^{2-}, F^- and Cl^- ions, and of calcium ions by Na^+, K^+ and Mg^{2+} ions in the apatite lattice[33]. The precise constitution of the tissue depends strongly on the complex chemical composition of the environment in which the teeth mineralization takes place. In general, the substitution of hydroxyl ions by carbonate ions is the most abundant in human teeth. Therefore, the mineral phase in human teeth is usually referred to as carbonated hydroxyapatite.

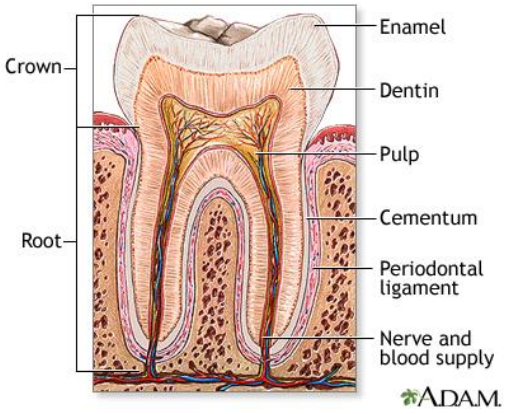

Figure 1.1: Schematic diagram of a human tooth. Adapted from Vorvick[34].

1.1.1. Enamel structure

Enamel consists mostly of carbonated hydroxyapatite (~ 96 wt.%) with minor proportions of organic matter, mainly amelogenin, ameloblastin and enamelin proteins[33]. These proteins are responsible for the growth of hydroxyapatite crystals and, therefore, mainly found in developing enamel. Besides, enamel contains a small amount of water, including water molecules adsorbed on the surface of hydroxyapatite crystals and "structural water", which is integrated in the hydroxyapatite lattice[35].

In enamel, the mineral phase is organized into closely packed bundles of rods (or prisms) 4 – 5 µm in diameter, running from the dentin – enamel junction (DEJ) to the surface of the tooth[33]. The rods

contain crystallites with mean width of 68 nm, mean thickness of 26 nm and length of 150 nm to 1 μm, oriented parallel to the rod axis[36]. The region between the rods is called interrod or rod sheath, which also consists of hydroxyapatite nanocrystals, with significantly different orientation than those at the center of the rods, and is relatively organic – rich[37]. The organization of hydroxyapatite nanocrystals in enamel is demonstrated in Figure 1.2. Due to the dominance of hydroxyapatite in enamel, this tissue presents physical properties typical for dielectrics such as low absorptivity in infrared (IR) and visible optical regimes[38] and low thermal conductivities [39].

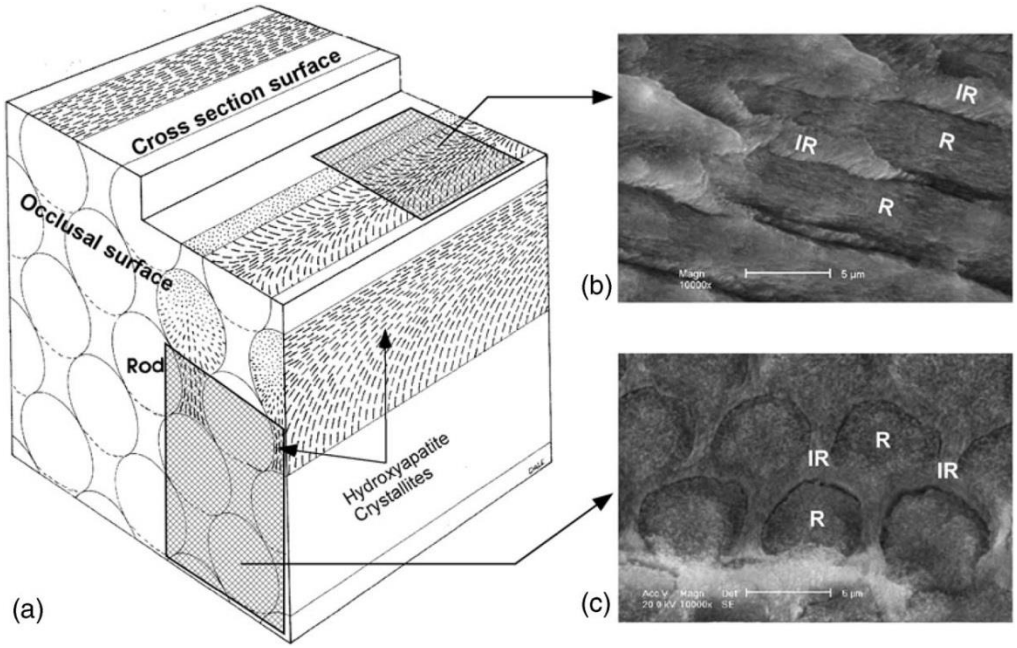

Figure 1.2: Schematic diagram of enamel rods (a) and electron microscopy images of enamel at different faces: parallel to the rods (b) and perpendicular to the rods (c). Adapted from Schneider et al.[40].

1.1.2. Dentin structure

Dentin, the main part of human tooth, contains approximately 70 wt.% carbonated hydroxyapatite, 20 wt.% organic matter, mainly type I collagen, and 10 wt.% water[41]. It is composed of peritubular dentin and intertubular dentin, which can be seen in the SEM micrograph of dentin surface obtained

by mechanical fracture shown in Figure 1.3a. The former component is made of hydroxyapatite nanocrystals, which form relatively dense mineralized cuffs, surrounding 1 – 4 μm diameter channels carrying the extension (also referred to as odontoblast process) of the odontoblast cells in the pulpal chamber and dentinal fluid, a mixture of albumin, transferrin, tenascin and proteoglycans, from the pulp to the dentin – enamel junction (DEJ). The odontoblast cells contained in the dentinal tubules, as shown in Figure 1.3b, are responsible for the formation and growth of dentin[32]. Moreover, these cells can react to compensate for the loss of hydroxyapatite in dentin due to the effects of dental caries by inducing the formation of tertiary dentin.

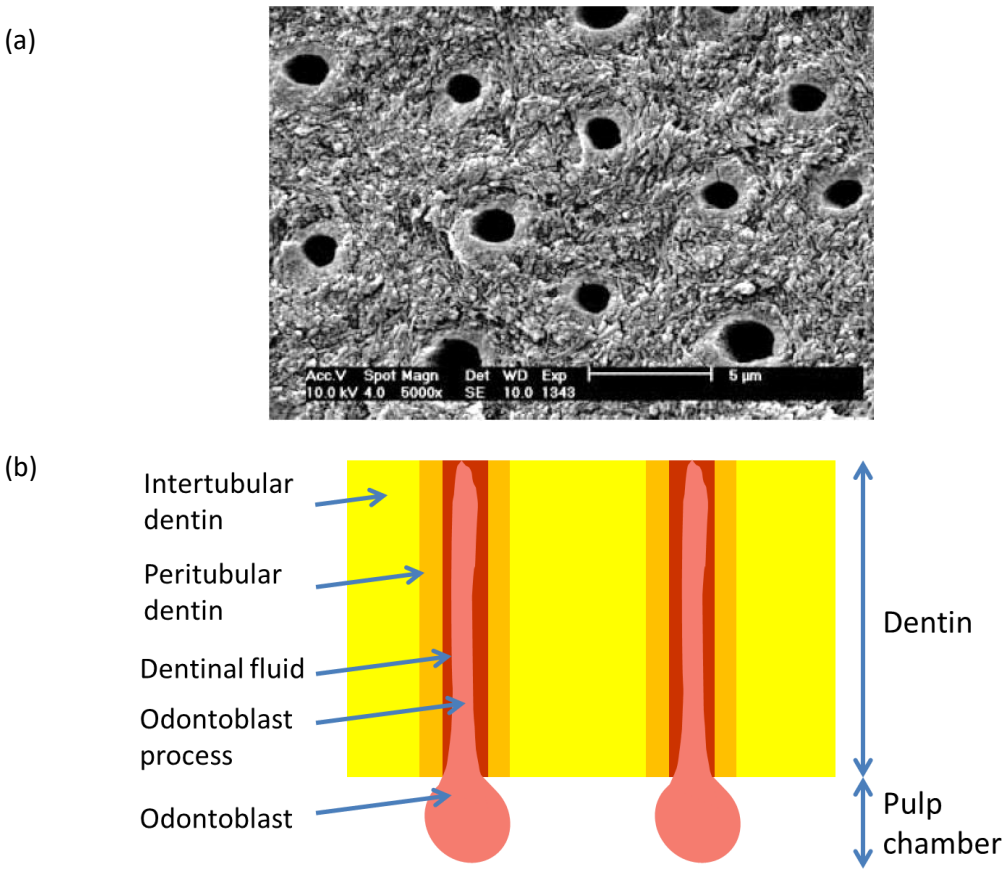

Figure 1.3: (a) A scanning electron microscopy image of dentin surface obtained by mechanical fracture perpendicular to the dentinal tubules, adapted from De Munck et al.[42], and (b) a schematic diagram of the longitudinal view of dentin showing the tubular structure.

While peritubular dentin contains a very small amount of organic matter, mainly proteins, intertubular dentin consists of a network of collagen fibrils reinforced with hydroxyapatite nanocrystals (Figure 1.4a)[43,44]. Collagen fibrils in dentin are formed by staggering 300 nm long collagen molecules (tropocollagen), which have a right–handed triple helical structure, constructed by the intertwining of three left-handed helical strands of polypeptide (procollagen) with repetitive amino acid sequence[45,46]. A periodic band structure is observed along the long axis of the fibrils with periodicity of ~67 nm due to the staggered arrangement of type I collagen, typical for dentin, bone and skin[45,47] (Figure 1.4b). In general, the stability of the triple helix and the fibril is mainly achieved by hydrogen bonds and covalent cross – linking. As the collagen is heated, hydrogen bonds are weakened, leading to an increase in the diameter of collagen fibrils and a shrinkage in the long axis[48]. In extreme cases, the molecular structure is destroyed and an amorphous structure is formed[48,49]. The alteration of collagen induced by heating is called thermal denaturation. The onset of this process strongly depends on the stability of the collagen, i.e. on the constitution of the helical chains, on the surrounding medium[50], and on the heating rate[51]. Bonar et al.[50] reported that the collagen fibrils in bone are stable after heating at 100°C for 30 minutes but shortening of the fibrils is observed in bone specimens demineralized by immersion in acid before the heat treatment. For dentin, collagen denaturation occurs in the temperature range 160 – 180°C at a heating rate of 10°C/min, but it depends on the age of the patient and the hydration of the teeth[52].

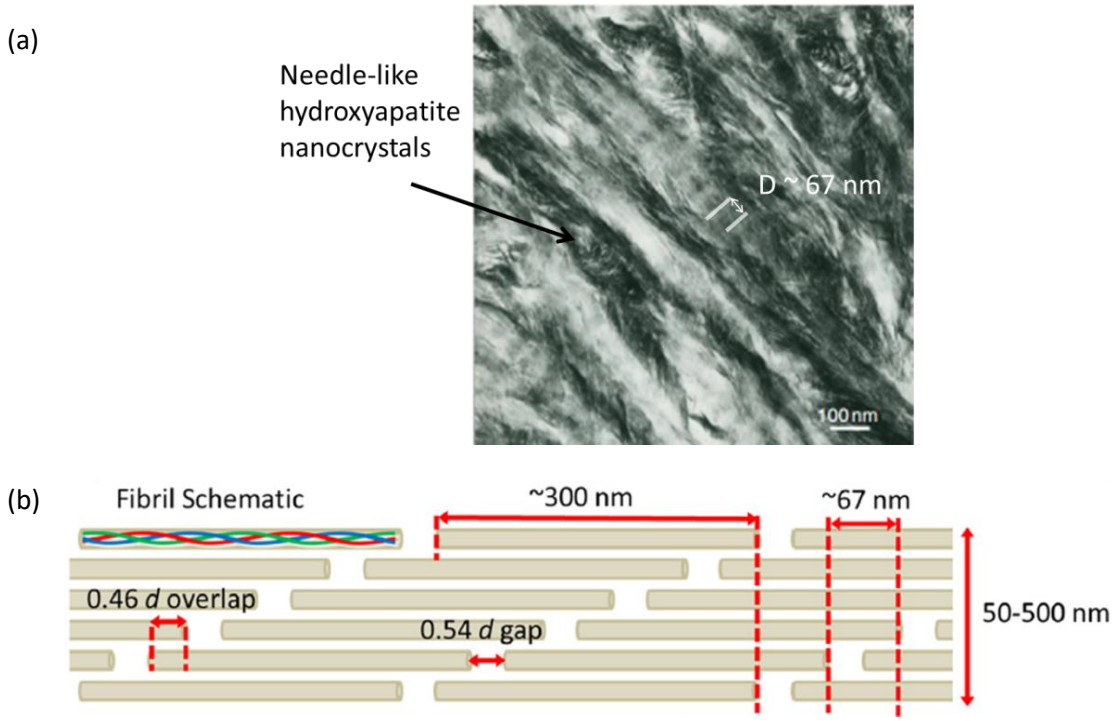

Figure 1.4: Transmission electron microscopy image of collagen in intertubular dentin (a), showing that the crystallites are located along and between the collagen fibrils, and the tructural hierarchy of fibrillar collagen (b). Adapted from Arthur et al.[53].

1.1.3. The formation of dental caries

Shortly after the teeth are cleaned, bacteria deposit on their surfaces. If left undisturbed, the bacteria, mainly streptococcus mutans and anaerobes[54], start to aggregate and form a continuous layer, called dental plaque[55]. The microbial composition of the plaque varies from tooth to tooth in the same individual or even for different locations on the same tooth. As fermentable carbohydrates are consumed, they are metabolized by the bacteria and organic acids such as acetic, lactic, formic and propionic acids are formed as by-products, which can dissolve hydroxyapatite in teeth[56]. It must be emphasized that the partial substitution of hydroxyl groups by carbonate groups in dentin and enamel hydroxyapatite increases significantly the solubility of this phase, as compared to the pure compound. When caries is still limited to enamel layer, its effect can still be counteracted by a remineralization process that occurs by the absorption of calcium and phosphate ions from saliva

and from external sources. The resistance of enamel to carious attack can be improved by the addition of fluoride ions in the constitution of hydroxyapatite on the enamel surface, leading to the formation of fluorapatite. This compound has high resistance against the acid corrosion than the carbonated hydroxyapatite[56–58]. If the demineralization occurs faster than remineralization, caries results and cavity forms at the tooth surface. As the caries progresses into dentin, it not only dissolves hydroxyapatite, but also destroys collagen and the odontoblast cells in the tubules, due to the action of bacteria in the infected layer[59]. The demineralization of dentin by dental caries is schematically described in Figure 1.5. While dissolved hydroxyapatite can be recovered by the supply of calcium and phosphate ions from the pulp, the destruction of the collagen matrix is irreversible. In addition, once the bacteria reach the pulp, they can destroy the organic compounds crucial for the tooth. Therefore, the caries must be removed as soon as it is detected.

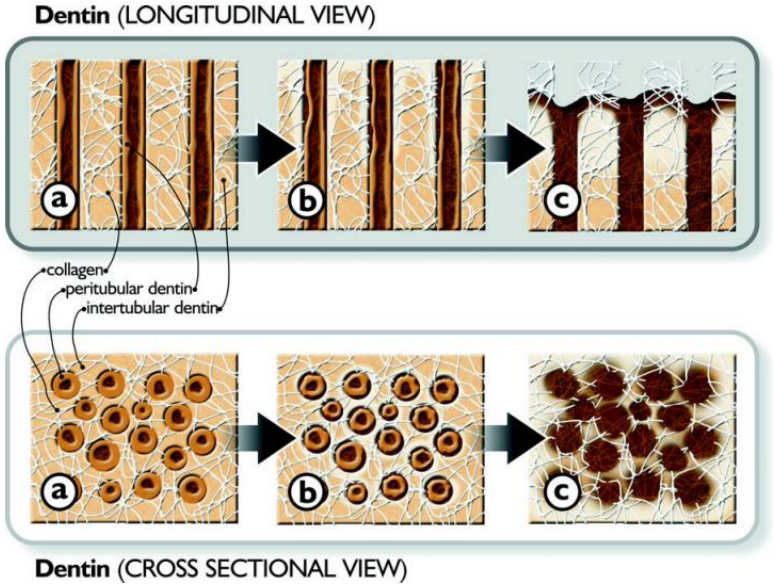

Figure 1.5: Demineralization process in dentin (longitudinal view and cross sectional view): (a) Unaffected dentin, (b) Initial demineralization of the hydroxyapatite in dentin and (c) the exposure of the collagen. Adapted from Magalhaes et al.[60].

1.2. Caries removal methods

Since the demineralization of enamel is hardly visible, dental caries are more frequently detected once they reach the dentin layer, causing pigmentation of the dentin due to the presence of chromophores from various bacteria. Therefore, most of the studies on caries treatment are performed on this part of the teeth. Various methods have been developed for carious dentin removal. They can be classified in three categories: mechanical, chemo-mechanical and laser-based methods[61].

The methods that are clinically approved for the removal of carious tissues are listed in Table 1.1. Among them, mechanical drilling has been thoroughly investigated, and is usually considered as a gold standard for the study of other methods[62,63]. It involves abrading the tissues with diamond or tungsten carbide burrs, rotating at high speed (> 500 rpm [64]) and with abundant cooling water. While this technique allows relatively high material removal rates, it induces high surface temperature and pain during the treatment [61,64,65]. In addition, the vibration and noise caused by the drilling action contribute to the discomfort of the patient.

Table 1.1: A summary of clinically approved excavation methods and their disadvantages. Adapted from Barnejee et al. [61]

Category	Techniques
Mechanical, rotary	Handpieces + burrs
Mechanical, non-rotary	Hand excavators, Air-abrasion, Air-polishing, Ultrasonics, Sono-abrasion
Chemo-mechanical	Caridex™, Carisolv™, Enzymes
Photo-ablation	Lasers

Compared to conventional burr caries removal methods, air – abrasion and sono – abrasion techniques are considered to reduce heat generation and vibration, but have lower material removal rates[61,64]. Similarly, chemo – mechanical removal methods, which involve the application of a chemical to soften the affected tissue followed by excavation with a hand instrument, allows good selectivity for the removal of carious tissue without the need of anesthesia, but this type of caries removal method is significantly more time consuming than the conventional technique[61].

With the requirement of minimally invasive caries removal methods, lasers have also been investigated as an alternative for caries removal. The idea was initially suggested recognizing the potential of lasers to drill and cut materials without significant thermal damage to the remaining material, and on the ability to focus the laser beam into a very small spot, suitable for high accuracy operation. The first investigations were performed using pulsed ruby lasers with a radiation wavelength of 0.6943 μm (unspecified pulse duration) in 1964 [2,3]. No sensation of pain was perceived by the patients[2,3]. Further investigations performed with various types of laser sources with radiation wavelength within the spectral range 0.193 μm (ArF laser [4]) to 10.6 μm (CO_2 laser[5]), and with pulse duration within the range from a few milliseconds (ms) to a few nanoseconds (ns). Among the laser sources tested, CO_2 (9.3 – 10.6 μm[5]), Nd:YAG (1.064 μm[6]), Er:YAG (2.940 μm[7]), and Er, Cr:YSGG (2.780 μm[8]) attracted special attentions due to the overlapping of their radiation wavelengths with an absorption band of hydroxyapatite (CO_2, Er:YAG and Er, Cr:YSGG) or water (Nd:YAG, Er:YAG and Er, Cr:YSGG). For CO_2 and Nd:YAG lasers with pulse duration within the range 10^{-3} – 10^{-9} s, the material removal rates achieved are low and ablation is accompanied by heating, often leading to tissue melting, carbonization, thermomechanical cracking and, in extreme cases, necrosis even when the laser treatment is performed with water cooling [6,66]. These results are explained by the laser – material interaction time sufficiently long for the transfer of a significant amount of heat to the material. On the contrary, the use of Er:YAG and Er, Cr:YSGG lasers with sufficient water spray allow achieving relatively high material removal rates while avoiding

significant thermal damage in the teeth, making them the main types of laser used in clinical applications. The morphology of dentin surface ablated by CO_2 laser and Er:YAG laser is demonstrated in Figure 1.6. The absence of major thermal damage in the case of Er:YAG and Er, Cr:YSGG laser treatment is explained by the fact that their wavelengths are within a very strong absorption band of water. Consequently, the radiation is efficiently absorbed by the water contained in the tissue, which warms up and boils explosively, leading to the mechanical disruption of the tissue[6,8]. With this ablation mechanism, the heat transferred to the tooth bulk is minimal. However, for certain processing parameter ranges, the shockwave created by the rapid evaporation of water can lead to sub – superficial cracks, which reduce significantly the tissue's mechanical strength [9].

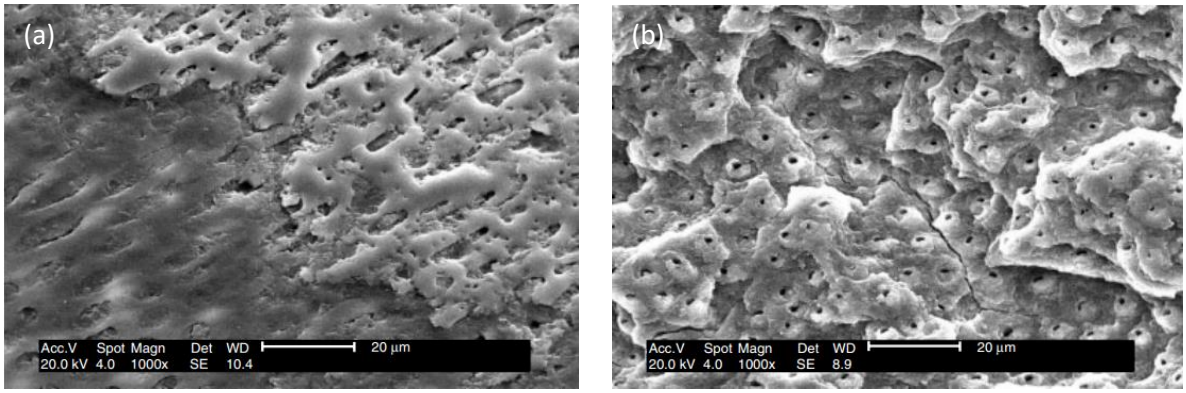

Figure 1.6: Scanning electron microscopy images of dentin surfaces ablated by CO_2 laser (9.6 µm, 20 Hz, 212.2 J/cm^2, 60 µs, 80 pulses) (a) and by Er:YAG laser (2.94 µm, 2 Hz, 25.7 J/cm^2, 200 – 500 µs, 120 pulses). Adapted from Zezell et al.[67].

Another approach to reduce laser – induced thermal effects is by using UV lasers with pulse duration within the nanosecond regime [4,11,68,69]. Sanchez et al.[4] and Eugenio et al.[11] showed that dentin can be ablated without significant melting of the remaining tissue by using ArF and KrF excimer lasers, respectively. On the other hand, Turkmen et al.[69] showed that the treatment with ArF laser leads to a rise of temperature in the pulpal chamber (1°C) significantly lower as compared

to CO_2 (37°C) and Nd:YAG (28°C) lasers. The lack of thermal damage induced by KrF and ArF lasers is explained by the fact that due to their high photon energies (5 eV for KrF and 6.42 eV for ArF) the radiation is preferentially absorbed by collagen in the dentin matrix, leading to breaking of the covalent bonds in collagen molecules[11]. The photochemical ablation of collagen decreases the cohesion of dentin, allowing the ablation of the tissue with minimal thermal damage on the remaining tissues. Despite these advantages, the application of excimer lasers is limited due to the low ablation rate and the exposure of patient to the hazardous UV radiation.

1.3. Adhesion of dental adhesives to treated tissue surface

After the dental caries has been removed, the cavity must be filled to prevent further colonization by bacteria. The filling material usually adheres to the tooth surface by the use of an adhesive (bonding agent). The bonding of dental restorative materials to the tooth structure allows hydroxyapatite content in dental tissues to be partially replaced by a synthetic resin which contain photo-initiators and can be photo-polymerized. Adhesion is usually achieved by mechanical interlocks with the prepared tissue surface[70,71]. With previous generations of dental adhesives, hydroxyapatite in the tissue is partially eliminated by acid etching and the products of the etching reactions are removed by rinsing in water before the application of adhesives[70,72]. Consequently, this type of adhesives is referred to as etch & rinse adhesive. Phosphoric acid H_3PO_4 is commonly used for the etching. On enamel, the acid dissolves the hydroxyapatite, forming etch pits between the enamel prisms, which provide mechanical interlocks to enhance the adhesion[70]. In dentin, the dissolution of hydroxyapatite in the intertubular dentin allows collagen fibers to be infiltrated by the adhesive monomers forming a hybrid layer[70,73,74]. In addition, resin tags are formed in the dentinal tubules, further enhancing the adhesion. The use of acid poses a risk of over – etching leading to the formation of a layer of exposed collagen fibrils which is not completely engulfed by the adhesive[75]. This layer has low mechanical strength and can be hydrolyzed by water trapped in the adhesive

resin or supplied by the oral environment, leading to long term failures of the hybrid layer[75,76]. In order to circumvent the problems associated with the acid etching, another type of adhesive has been developed, which contains acidic monomers and has a pH in the range 0.4 – 4.7[70]. Those adhesives, generally referred to as self - etch adhesives, are capable of etching the dental tissues, allowing them to be applied either with the prior acid etching step (total – etch application mode) or without it (self – etch application mode). In self – etch application mode, this type of adhesive dissolves lower amount of hydroxyapatite than the phosphoric acid based etchants (pH ~ 0.1 – 0.4) and the demineralization is accompanied by the infiltration of the resin, leading to complete envelopment of the exposed collagen fibrils. The extent of demineralization and infiltration depend on the pH of the adhesive mixture and on the structure and chemical constitution of the tissue surface[77,78]. When a dense smear layer is formed on treated surfaces of dentin or enamel, prior acid etching step (total – etch application mode) is still recommended[78]. On the other hand, in order to improve the adhesion strength, phosphate based monomers, such as phenyl-P (2-methacryloxyethyl phenyl hydrogen phosphate), and 10-MDP (10-methacryloxydecyl dihydrogen phosphate), are usually included in the self – etch adhesive mixtures to induce additional chemical bonds with the remaining hydroxyapatite crystals[70]. For both etch & rinse and self – etch adhesives, the adhesion to dental surfaces depends strongly on the chemical composition of the adhesives and the technique used to prepare the surfaces.

1.3.1. Bonding to dentin surfaces prepared by mechanical drilling

In general, the surface of dental tissues after mechanical drilling is covered with a dense layer of calcium phosphate debris, called smear layer. In the case of dentin, the smear layer also contains collagen fibrils which are partially denatured due to the frictional heat induced by the drilling process[77,79,80]. The thickness, morphology and structure of this layer depend on the type of drill, rotating speed and use of water cooling[77,81]. The debris are also detected in the dentinal tubules,

forming smear plugs. The smear layer limits the infiltration of resin in the dental tissue and is weakly attached to the underlying tissue, leading to a significant reduction of the resin-dentin bond strength. To avoid this issue, an etching step is needed in case of the etch & rinse adhesives [70,72]. For self – etch adhesives, their ability to dissolve the smear layer and bond with the underlying tissue depends on the type of drill head and the drilling procedure used, which affect thickness and composition of the smear layer, as well as on the composition of the adhesive mixture [77,78,81]. Mine et al.[77] showed that ultramild self – etch adhesives (pH ~ 2.7) might be unable to penetrate the smear layer to form strong bonding with the underlying dentin if dense smear layer is formed after the surface treatment.

1.3.2. Bonding to dentin surfaces treated by Er:YAG and Er, Cr: YSGG lasers

Dentin surfaces treated by Er:YAG and Er, Cr:YSGG lasers are characterized by the absence of smear layer and resolidified material, apparently making them suitable for the direct application of the adhesive[7,9,74,82,83]. Several authors showed that the bond strength of restorative dental adhesives to dentin treated by these lasers is comparable to or higher than the bond strength obtained for dentin prepared by drilling[84,85]. Unfavorable results have also been reported for the adhesion of adhesive resins to dentin treated by these lasers. They were partially explained by the presence of sub – superficial cracks for a certain range of laser processing conditions, leading to a significant reduction of the mechanical strength of dentin[8,9,74,86,87]. In addition, it was shown that the heat transferred to the remaining tissue during the laser treatment was sufficient to form a collagen depleted layer at the laser treated surface, followed by another layer of unaltered hydroxyapatite and thermally denatured collagen[74,86,88]. Ceballos et al.[74] estimated the thicknesses of those layers to be in the range 3 – 10 μm for a surface treated by an Er:YAG laser with radiation fluence of 23 J/cm^2 and a repetition rate of 2 Hz. Similar surface alterations were observed by Moretto et al.[9] for dentin treated by Er, Cr: YASGG laser with fluences in the range 90 – 181 J/cm^2, pulse repetition rate of 20

Hz and by Er:YAG laser with fluence in the range 53 – 83 J/cm^2 and pulse repetition rate of 4 Hz. The collagen depleted layer is weakly attached to the dentin substrate, causing mechanical failure during the bond tests [86]. This layer can be removed by etching to improve the adhesion, but the bond strength obtained after etching is still lower than the strength obtained with mechanically drilled dentin surfaces [8,9,74,86]. These results are explained by the fact that the partially denatured collagen layer inhibits the formation of a strong hybrid layer by the infiltration of the adhesive. Consequently, both rinse & etch adhesives and self – etch adhesives provide lower adhesion strengths on dentin surface treated with Er:YAG and Er, Cr: YSGG lasers as compared to dentin surface prepared by mechanical drilling [8,9,74].

1.4. The use of ultrashort pulsed laser in caries removal treatment

1.4.1. Ultrashort pulsed laser ablation of dielectric materials

1.4.1.a. Absorption of ultrashort radiation

Dielectric materials are characterized by the existence of a large energy gap between the valence and conduction band (E_g > 2.8 eV). The valance band is completely filled while the conduction band is empty at room temperature. As a result, these materials present low thermal and electrical conductivity. Examples of this type of material are ceramics, diamond and sapphire. Due to their high band gap energies, these materials are transparent for low intensity radiation in the near infrared and visible spectral regions. Consequently, they can only be machined by UV excimer lasers (KrF[89], XeCl[90]) typically with high pulse duration (~ 30 ns). The availability of ultrashort pulse duration lasers (τ < 10 ps [91]) allowed high peak intensity to be obtained, leading to the possibility of radiation absorption in dielectrics by multiphoton excitation [91–94]. This process allows electrons in the valence band to absorb the energy of several photons to be promoted through the band gap into the conduction band. Once in the conduction band, these electrons can continue to absorb radiation energy by inverse Bremstrahlung to further increase their energy[94]. The electronic processes that

take place in dielectrics irradiated by ultrashort pulsed laser are schematically demonstrated in Figure 1.7.

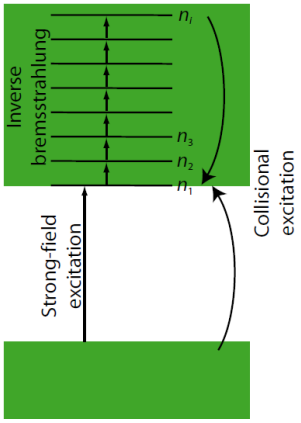

Figure 1.7: A schematic description for the electronic processes in dielectrics irradiated by ultrashort pulsed laser, which lead to the generation of electrons in the conducting band. Adapted from Balling et al.[94].

When the density of electrons in the conduction band is sufficiently high, collisional ionization mechanism also contributes to the generation of free electrons. When the density of excited electrons is high, the solid presents metal – like behavior and optical properties, with high reflectivity and high absorption coefficient [94,95]. The penetration of the laser pulse can be described by the normal skin effect where the electric field of the radiation decreases exponentially with increasing depth into the material[95]:

$$\mathbf{E(x) = E(0) * exp(-\frac{x}{l_s})} \quad (1.1),$$

where l_s is the thickness of the skin layer and can be expressed as

$$\mathbf{l_s = \frac{c}{\omega k} = \frac{\lambda}{2\pi k}} \quad (1.2).$$

The parameters ω and k in equation 1.2 represent the frequency of the electromagnetic field associated with the laser radiation and the extinction coefficient of the skin layer, respectively. Consequently, as a sufficient amount of free electrons is generated, the extinction coefficient

changes from values lower than 1 for dielectrics to higher than 1, typical for metals, and the radiation energy is absorbed in a surface layer with a thickness of a fraction of the radiation wavelength.

1.4.1.b. Ablation processes

Among the electrons promoted to the conduction band by the radiation, those with energies surpassing the work function of the material can be ejected from the surface. In dielectric materials, the emitted electrons are not compensated by electron diffusion from the bulk due to the low mobility of electrons in this type of materials, leading to a breakdown of charge neutrality in the surface region[96,97]. The buildup of positive charge in the surface layer causes an increasing electric field in this region. When the electrostatic repulsion force, which is proportional to the electric field, exceeds the binding forces of the ions in the lattice, the ions are ejected due to the intrinsic repulsive forces, a mechanism usually referred to as Coulomb explosion[98]. This ablation mechanism was firstly observed for the ablation of sapphire by radiation with a wavelength of 800 nm, pulse duration of 100 – 200 fs and a fluence of 4 J/cm^2 [97,98]. Figure 1.8 displays the evolution of charge density and electric field on the irradiated surfaces of gold, silicon and sapphire as calculated by Bulgakova et al.[97]. The authors demonstrate that a transient electric field exceeding the value needed to break atomic bonds in sapphire is formed in the subsurface region of the specimen several hundred femtoseconds after the laser pulse. The density of accumulated charge in Si and Au is much lower than in sapphire, probably due to the higher mobility of free carriers in those materials, allowing electrons to diffuse to the electron depleted region. By using time – of – flight technique, Stoian et al.[98] showed that electrons with eV energy order of magnitude (prompt electrons) are ejected from the irradiated sapphire surface, followed by slow electrons (with energies on the order of meV) and ions, as shown in Figure 1.9a. The ejected Al^+ and O^+ ions present similar momenta but different kinetic energies, suggesting that the acceleration mechanism is mass

independent, with well – defined momentum transfer, consistent with the transient electric field proposed by Bulgakova et al.[97]. The argument is further supported by the fact that the velocity of double charged oxygen ions is approximately twice the velocity of single charge oxygen ions[98]. The timescale for the Coulomb explosion is within 1 ps after the absorption of radiation energy by the electrons, too fast for the transfer of energy from the excited electrons to surrounding lattice to occur (~ 10 – 100 ps in defect – free solids [99]). As a result the ablation process does not involve thermal effects and Coulomb explosion is usually referred to as a "cold" ablation mechanism.

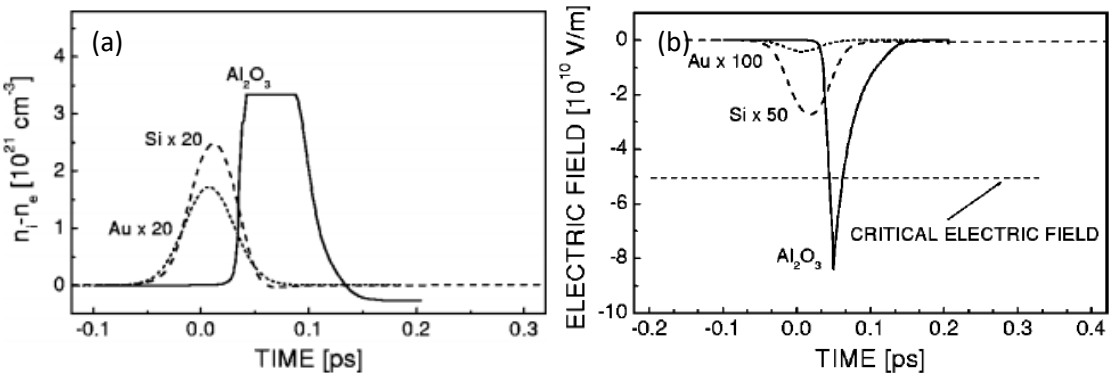

Figure 1.8: Simulated time evolutions of charge density (a) and electric field (b) in the surface region of Au, Si and Al_sO_3 irradiated by single laser pulse with pulse duration of 100 fs, wavelength of 800 nm and radiation fluences just above the ablation thresholds of corresponding materials. Adapted from Bulgakova et al. [97].

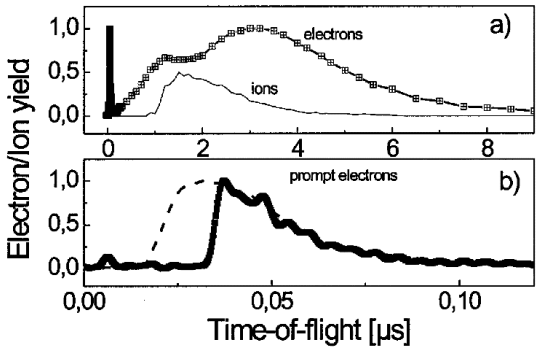

Figure 1.9: Time of flight spectra of electrons and ions ejected from Al_2O_3 after irradiation with a laser with 200 fs pulse duration, 800 nm radiation wavelength and radiation fluence of 4 J/cm^2. (a) full range. Squares: both prompt electrons and slow plasma electrons; solid line: time of flight of the corresponding ions (O^++Al^+). (b) Expanded scale showing prompt electrons. Thick line: from Al_2O_3; dashed line: from Al. Adapted from Stoian et al. [100].

Another ablation mechanism that typically occurs several picoseconds after the electron excitation by the laser radiation, involves energy transfer from the excited electrons to the lattice in the form of heat. The heating rate depends essentially on the electron – phonon coupling rate and the thermal diffusivity of the material and ablation occurs once the thermomechanical stability limit of the material is reached. With pulse durations in the picosecond and femtosecond ranges, the laser – material interaction occurs in thermal confinement conditions, which require that [101]

$$\tau_p \leq \tau_{th} \approx L_p^2 / D_T \tag{1.3}$$

where τ_p, τ_{th}, L_p and D_T are the pulse duration, the thermal diffusion time, the radiation penetration depth and the material thermal diffusivity, respectively.

In these conditions, the energy transferred concentrates in the absorbing region. This confinement induces an isochoric heating process. As a result, the surface layer is transformed into a liquid that is rapidly heated up to a temperature near the spinodal temperature of the material [94,102,103]. This overheated liquid is metastable and decomposes rapidly into a mixture of vapor and liquid droplets, a process called phase explosion.

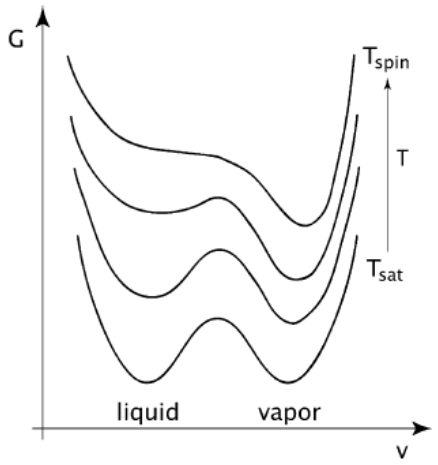

Figure 1.10: The evolution of Gibbs free energies of a pure substance in liquid and vapor states as the temperature approaches critical point [104].

As shown in Figure 1.10, at the normal boiling temperature, there are two local minima in the Gibbs free energy of a substance corresponding to the liquid and vapor states, which exist in equilibrium with one another. The liquid – to – vapor transformation is a nucleation and growth process which requires an activation energy for nuclei with radius higher than the critical value for homogeneous nucleation to form[104]. As the temperature approaches the critical temperature, the minimum becomes shallower and the liquid state becomes increasing unstable. At the spinodal temperature this local minimum vanishes and the liquid – to – vapor transformation occurs spontaneously without the need of an activation energy[104]. Phase explosion results in a sudden decomposition of the unstable liquid near the spinodal temperature into a mixture of extremely fine liquid droplets and vapor (Figure 1.11). The proportion of gas in the mixture depends on the overheating, which, in turn, depends on the radiation fluence [101].

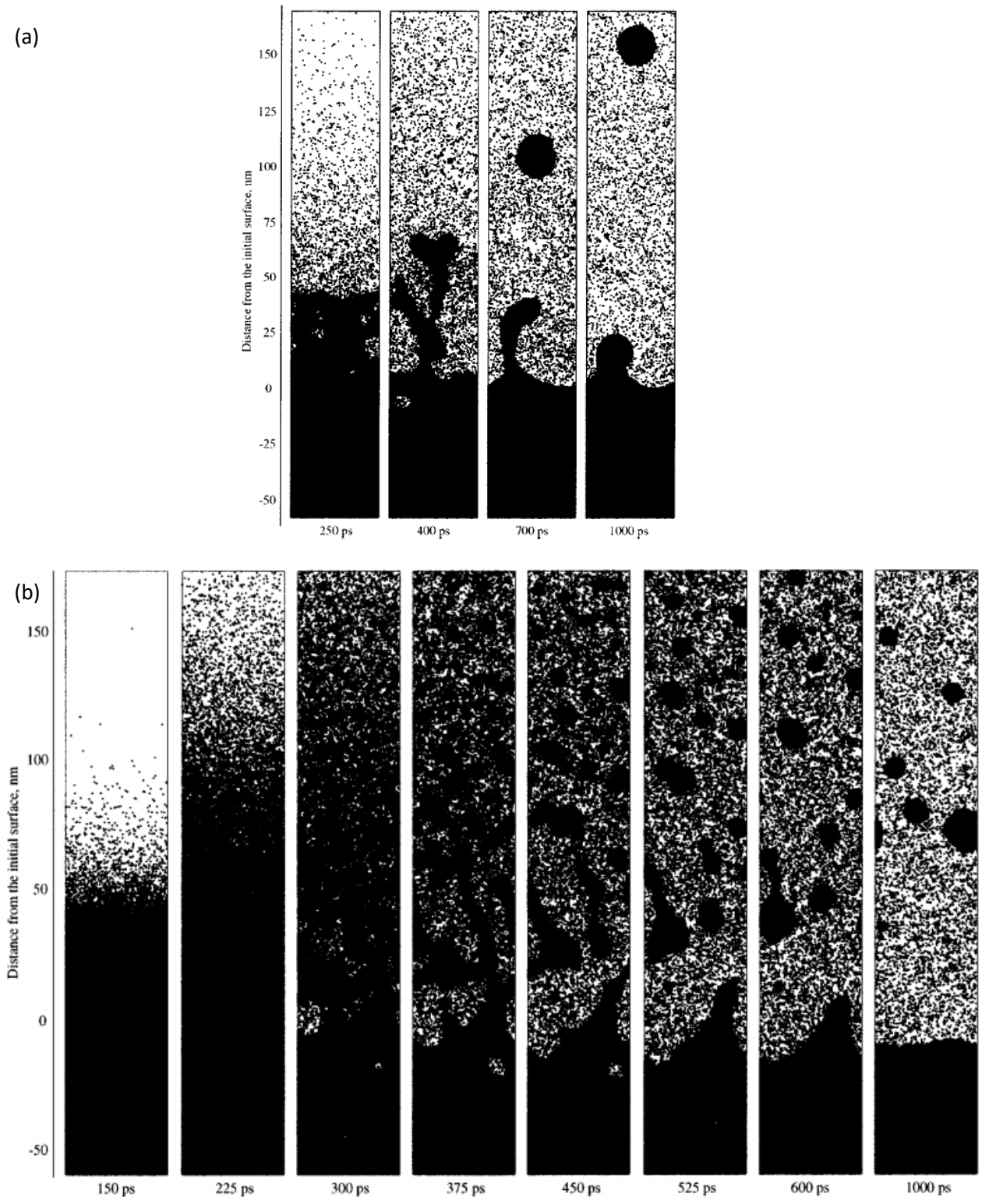

Figure 1.11: Snapshots from the MD simulation of a molecular surface irradiated by radiation with pulse duration of 150 ps, fulfilling the thermal confinement condition, and radiation fluence of 39 J/m^2 (a) and 61 J/m^2 (b). Adapted from Zhigilei et al.[101]

Besides the rapid increase of temperature in the absorbing region, the ultrafast deposition of radiation energy induces compressive stress in this region[103]. If the pulse duration is shorter or of the same order as the time required for the mechanical relaxation of the heated material, the heating occurs at a constant volume, generating significant compressive stresses in the absorbing region. This condition, referred to as stress confinement, is generally fulfilled for pulse duration in the femtosecond regime and can be expressed by [101]

$$\tau_p \leq \tau_s \approx L_p / c_s \quad (1.4)$$

where τ_S and c_s are the characteristic time of mechanical equilibration of the absorbing volume and the speed of sound in the irradiated material, respectively. Once sufficient compressive stresses are generated, they can promote mechanical fracture of the material and cavitation/fragmentation in the metastable liquid, leading to ablation the material by a spallation mechanism, as demonstrated in Figure 1.12a[101]. The depth at which voids nucleate depends on the tensile strength of the material and on the laser-induced pressure. If the radiation fluence is sufficiently high, ablation starts with the phase explosion of the surface volume heated up to temperatures near the critical temperature (Figure 1.12b). The underlying layers are also heated but remain in metastable condition. Voids are created because of the accumulated stresses and ablation proceeds by a spallation mechanism.

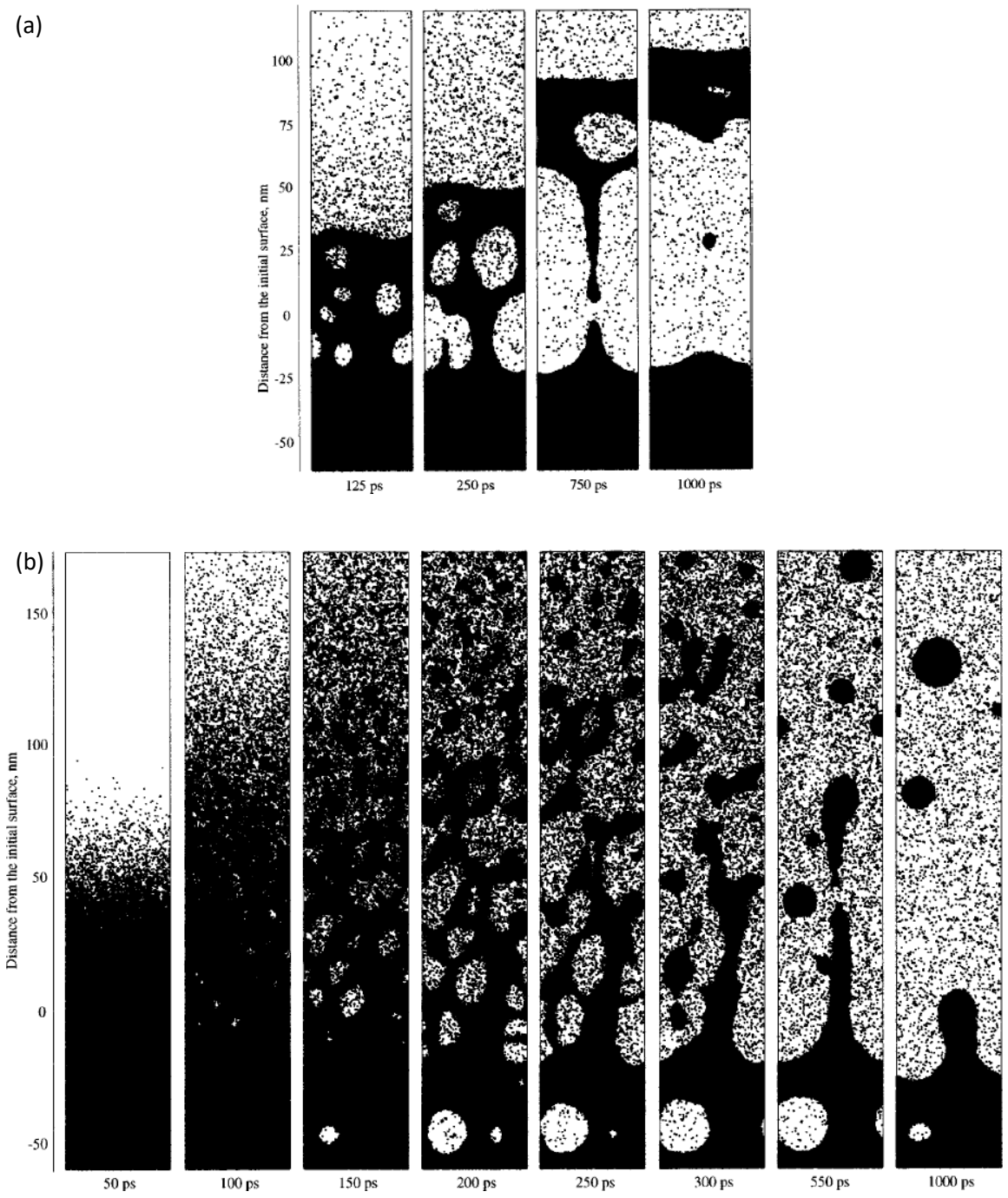

Figure 1.12: Snapshots from the MD simulation of a molecular surface irradiated by radiation with pulse duration of 15 ps, fulfilling the stress confinement condition, and radiation fluence of 34 J/m^2 (a) and 61 J/m^2 (b). Adapted from Zhigilei et al.[101].

The time scales of different events that can happen during the interaction between ultrashort laser and dielectrics are demonstrated in Figure 1.13. In principle, the ablation of dielectrics can involve Coulomb explosion, liquid spallation and phase explosion. Coulomb explosion occurs within a few hundred femtoseconds since the onset of the electron excitation process. After the Coulomb explosion, the remaining excited electrons transfer their energy to the lattice, initiating thermal ablation processes. The energy transfer is done via electron – phonon coupling, which, in defect-free dielectrics, only occurs several picoseconds after the laser pulse. The presence of defects in the dielectric facilitates energy transfer from the electrons to the lattice and, as shown by Stoian et al.[98] in the case of sapphire, leading to the increasing importance of thermal processes in ablation. The defects can be native or generated by the irradiation even for radiation fluences below the ablation threshold[94,98]. These defects usually have energy levels within the band gap and can also enhance the absorption of radiation by enabling lower order multiphoton absorption, leading to a decrease of the ablation threshold. This dependence of the ablation threshold on the number of laser pulses, referred to as the incubation effect [14,105], is due to the creation of defects by laser irradiation, and can be expressed by [106]:

$$F_{th}(N) = F_{th}(1)N^{S-1} \tag{1.5}$$

where N, $F_{th}(1)$, $F_{th}(N)$ and S are the number of pulses, the ablation threshold for single pulse ablation, the ablation threshold for N-pulse ablation and the incubation coefficient, respectively.

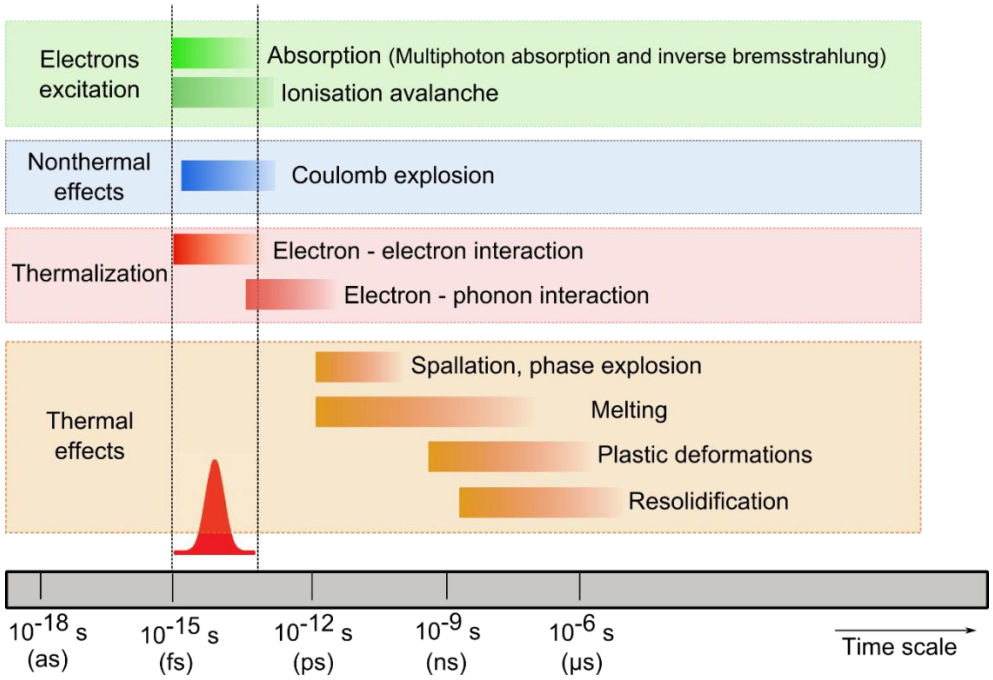

Figure 1.13: Time scale of different events that happen in a dielectric material after the irradiation with ultrashort laser pulse. Adapted from Cangueiro et al. [107].

1.4.2. Ultrashort pulsed laser ablation of organic materials

Organic materials consist mainly of carbon atoms, forming the backbone of the molecular structure, bonded with atoms of various elements such as H, O, N, F and Cl. They are abundant in biological soft tissues such as cornea, tendons and ligaments. In hard tissues, even though hydroxyapatite is the dominant phase, the cohesion of the tissue, especially bone and dentin, is ensured by the presence of organic matters, mainly type I collagen. Organic materials can be ablated by infrared pulse lasers with wavelength of several micrometers. Photon energy corresponding to this spectral range can only induce transition of the molecules to a higher order vibration mode in the ground electronic state[108]. Absorbed energy is coupled to the lattice as the molecules relax to lower order vibration mode, leading to heating, followed by thermal decomposition of the material. Organic compounds can also be ablated by UV lasers with wavelength in the range 193 – 308 nm and pulse duration in the nanosecond range. In contrary to the case of IR lasers, energy of photons in the UV

spectral range is sufficiently high to induce a transition of the organic molecule to an excited electronic state, from which the molecules can be decomposed by breaking of the chemical bonds[108]. Since the dissociation of the molecules follows a purely chemical reaction pathway, thermal effects were observed in the remaining material. Eugenio et al.[11] suggested that for KrF excimer laser ablation of dentin, the photochemical ablation mechanism results in breaking of the covalent bonds in collagen molecules, facilitating the ablation of the tissue without significant thermal damage.

With the development of ultrashort pulsed lasers high radiation intensity is achieved, which facilitates multiphoton absorption processes allowing electronic excitation in organic materials even for radiation in the near infrared range[109]. Serrano et al.[110] showed that species emitted during the ablation of organic compounds by femtosecond pulse lasers contain more fragments of the native molecules than the case of nanosecond pulse lasers, indicating the dominance of chemical bond breaking processes in the interaction with femtosecond duration radiation. In another study, Hovhannisyan et al.[111] showed that type I collagens were ablated by femtosecond lasers without significant thermal damage. New species formed by the disintegration of collagen molecules were observed in the vicinity of the laser-modified regions, supporting the predominant photochemical ablation mechanism. This ablation mechanism was also reported for the ablation of other biological soft tissues by ultrashort pulse lasers[109]. Besides, thermal processes leading to the ablation of organic solid material by liquid spallation and phase explosion can play increasing role in the ablation of organic compounds if high radiation fluences are used[101,109]. Nevertheless, thermal damage in the remaining material is always negligible with this type of lasers.

1.4.3. Ultrashort pulsed laser ablation of dental hard tissues

The ablation of dentin and enamel by lasers with radiation wavelength in the near infrared region and for pulse duration in the picosecond and femtosecond regions was the object of a number of publications[16–18,112–116]. In general, these lasers allow accurate removal of dental tissues with

significantly lower thermal and mechanical damage to the remaining materials as compared to lasers with longer pulse duration[16,112,115,117]. The values of ablation threshold for these tissues are summarized in Table 1.2. In general, for similar experimental conditions, the ablation threshold of enamel is higher than the ablation threshold of dentin. This result can be explained by the higher content of collagen in dentin as compared to enamel; the stability of the molecular structure of collagen is ensured by weak intermolecular Van der Waal bonds. The values of the ablation threshold determined by different authors cannot be directly compared due to the differences of the lasers employed and processing conditions such as wavelength, pulse duration, number of laser pulses, pulse repetition rate and diameter of the laser spot, which can significantly affect the ablation behavior of the tissue [93,106,118]. Differences in the specimen preparation methods and storage conditions must also be considered, since they can influence the optical properties and the constitution of the specimens. Unfortunately, this information is not always mentioned in the publications.

Table 1.2: Reported values for the ablation thresholds of dental hard tissues by ultrashort pulsed lasers

Dental tissue	Wavelength (nm)	Pulse duration (fs)	Number of pulses	Ablation threshold (J/cm^2)	Authors
Enamel	1053	350	100	0.7	Neev et al. [114]
Enamel	615	300	100	0.6	Kruger et al. [16]
Enamel	800	85	1	0.57	Ji et al. [18]
Enamel	800	95 & 150	1	2.2 ± 0.1	Rode et al. [15]
Enamel	400	95	1	1.0 ± 0.2	Rode et al. [15]
Enamel	1045	500	unspecified	1.6	Bello – Silva et al. [117]
Dentin	1045	500	unspecified	1.1	Bello – Silva et al. [117]
Dentin	800	85	1	0.43	Ji et al. [18]
Dentin	615	300	100	0.3	Kruger et al. [16]
Dentin	1053	350	100	0.5	Neev et al. [114]
Dentin	1030	500	1	0.6 ± 0.2	Alves et al. [17]

Despite many studies on the ablation threshold of dental hard tissues, only a limited effort was dedicated to the study of the ablation mechanisms of dental hard tissues and to the characterization of the surface morphology and constitutions of the surface layers of material after the laser treatment[17,18,119]. Alves et al.[17] and Bello-Silva[120] showed that the morphology of irradiated dentin surface is similar to the morphology of mechanically fractured surface. Alves et al.[17] also reported that the structure and constitution of dentin were preserved after the laser treatment, as

investigated by x-ray photoelectron spectroscopy (XPS), Fourier transform infrared (FTIR) spectroscopy and x-ray diffraction (XRD). The absence of resolidified material and of other thermal effects after the laser treatment was explained by a predominant electrostatic ablation mechanism. A similar mechanism was proposed by Rode et al.[15] for the ablation of enamel by femtosecond laser. On the contrary, traces of melting and the presence of resolidified materials on the surface of dental enamel after laser ablation by femtosecond lasers were reported by Krüger et al. [16] (300 fs, 615 nm, 3 Hz, 100 pulses, 2 J/cm^2) and Shaheen et al.[121] (130 fs, 785 nm, 20 Hz, 5 pulses, 6.2 J/cm^2) but those authors did not perform any chemical or structural analysis.

Despite the potential of ultrashort pulse lasers in caries removal treatment, the adhesion of restorative adhesives to dentin surfaces treated with this type of lasers has only been reported by Bello – Silva[120] and Portillo et al.[87]. By using a laser with pulse duration of 500 fs, wavelength of 1045 nm operating at a repetition rate of 100 kHz and with fluences of up to 4.9 J/cm^2, Bello – Silva[120] showed that the adhesion strengths to laser treated dentin surfaces are similar or higher, depending on the adhesive systems, than the adhesion strengths obtained with reference specimens. On the contrary, reduced bond strengths for irradiated dentin surfaces were observed by Portillo et al. (120 fs, 795 nm, 1 kHz, 39.8 J/cm^2) [87]. In both studies, the reference specimens were prepared by polishing dentin surface with SiC papers with grit sizes of 800[120] and 600[87]. The reduction of bond strengths obtained with dentin surfaces irradiated by ultrashort pulsed laser observed by Portillo et al.[87] might be caused by the structural and chemical modifications induced in the laser treated dentin surfaces by the very high radiation fluence used in that study (39.8 J/cm^2), which were unfortunately not characterized in detail.

2. Experimental methods

The content of this chapter is organized as follows:

- Sample preparation.
- Femtosecond laser system and optical setup for laser beam delivery.
- Laser ablation experiments in stationary and scanning conditions.
- Set-ups used for the measurement of temperature in the pulpal chamber during laser treatment and for testing the influence of external cooling.
- Techniques used to characterize morphology, structure and chemical constitution of laser treated surfaces.
- Dental restorative adhesive system and mechanical test used to evaluate the bond strengths obtained with laser treated dentin surfaces.

2.1. Sample preparation

Human third molars were extracted from patients with informed consents following a clinical protocol approved by the Ethics Committee in Bordeaux, France (process DC 2014/04). The extraction was performed, at most, six months before the laser experiments and the teeth were stored in saline solution at 4°C. Enamel and dentin disks were cut from the teeth by using a low speed diamond saw (Accutom-50 ®, Struers ©, Denmark) at an advancing speed of 0.5 mm/s, as indicated in Figure 2.1. One of their faces was polished under flowing water using a 600 - 1000 - 2500 grit sequence of SiC papers. The samples were prepared, at most, one week before the laser experiments and stored in distilled water at 4°C. Prior to the laser treatment, they were extracted from the liquid and gently wiped with a clean paper tissue to remove the water excess.

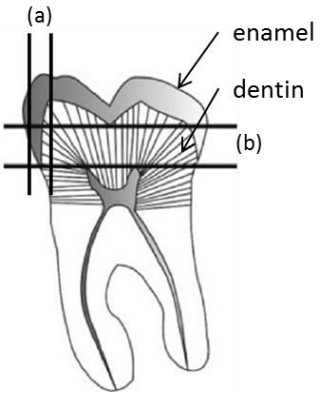

Figure 2.1: Schematic for preparation of enamel (a) and dentin (b) disks

(adapted from Yalçin et al.[122]).

2.2. Femtosecond laser processing

2.2.1. Yb:KYW laser system and the set-up used for laser ablation experiments

The ablation experiments were performed in the Laser Materials Processing Laboratory of CeFEMA, Instituto Superior Tecnico. A Yb:KYW chirped-pulse-regenerative amplification laser system (model s-Pulse HP, Amplitude Systemes ©, France) with 560 fs pulse duration and 1030 nm radiation wavelength was used. The laser beam had a Gaussian profile and was linearly polarized. Specifications of the system, as provided by the manufacturer, are listed in Table 2.1. In order to achieve a pulse repetition rate lower than 1 kHz, an external frequency generator was used to fix the repetition rate of the laser amplifier.

Table 2.1: Specifications of the Yb:KYW femtosecond laser system

s-Pulse HP model	
Pulse duration	~ 560 fs
Maximum pulse energy	~ 1 mJ
Pulse repetition rate	1 - 100 kHz
Central wavelength	1030 nm
Laser beam quality	TEM_{00}

The setup employed for laser experiments is presented in Figure 2.2. The emitted laser beam was guided by a set of highly reflective mirrors to a converging lens (l_{focal} = 100 mm), which focused the beam perpendicularly to the specimen surface. Before the laser experiments, a power meter (model 10A-SH-V1.1 RoHS, Ophir Photonics ©, Israel) was placed in the optical path of the laser beam and before the mirror system to measure the average laser power. The laser power delivered at the specimen surface was varied in the range 40 – 560 mW with the use of an optical filter as indicated in Figure 2.2, assuming a loss of 15% of the laser power due to the mirror system. The position of the specimen surface was precisely controlled by a computer-controlled XYZ stage (PI miCos ©, Germany) with a positioning accuracy higher than 0.5 μm and a repeatability of 0.1 μm.

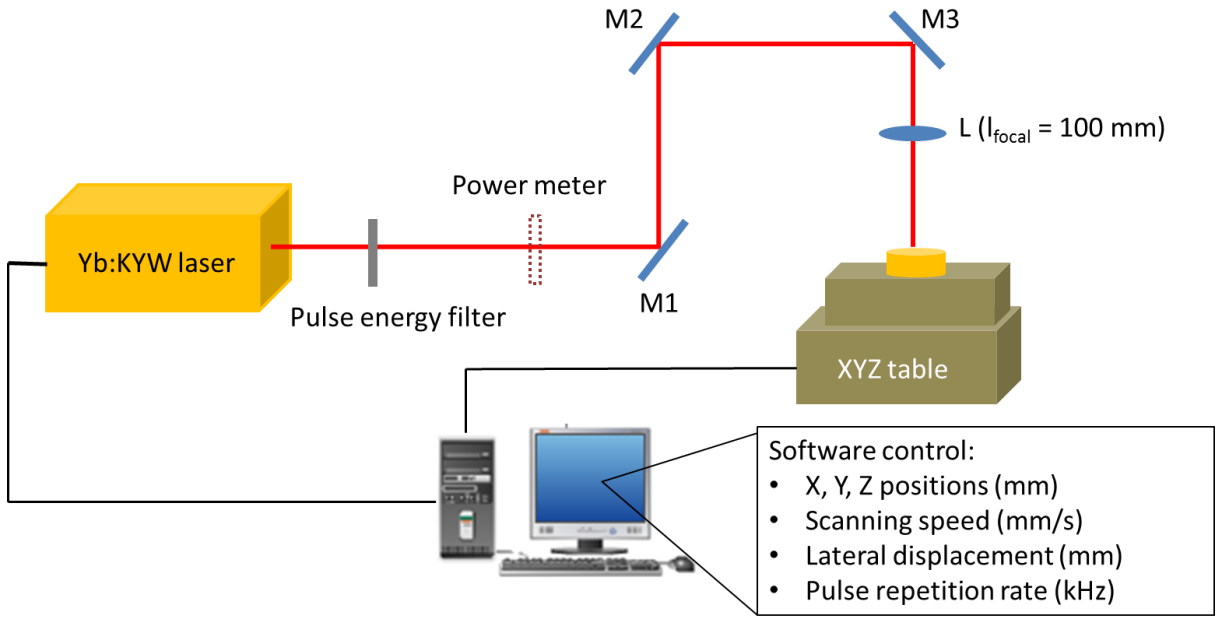

Figure 2.2: Schematic of the optical setup used for the laser experiments.

2.2.2. Laser experiments

2.2.2.a. D^2 method for determination of laser beam diameter and ablation threshold

In the present work, the D^2 method, proposed by Liu[123], was used to determine the diameter of the laser beam on specimen's surface and ablation threshold of the specimen. This method is based on the assumption of spatial Gaussian intensity distribution of the laser beam, which allows the radiation fluence in a plane perpendicular to the beam to be expressed by

$$\mathbf{F(r) = F_0 exp(-\frac{2r^2}{w_0^2})} \quad (2.1),$$

where r is the distance to the beam axis, w_0 the beam spot radius at $1/e^2$ of the maximum intensity and F_0 the maximum fluence. Consequently, the diameter D of an ablation crater produced by single or multiple laser pulses can be expressed by

$$D^2 = 2w_0^2 \ln(\frac{F_0}{F_{th}}) \quad (2.2),$$

where F_{th} is the ablation threshold of the specimen. On the other hand, F_0 and the pulse peak energy E_P can be related by

$$\mathbf{F_0} = \frac{\mathbf{2E_P}}{\boldsymbol{\pi} \mathbf{w_0^2}} \quad (2.3).$$

The pulse energy can be calculated from the average laser power by

$$\mathbf{E_P} = \frac{\mathbf{P}}{\mathbf{f}} \quad (2.4),$$

where f is the pulse repetition rate and P is the average power of laser beam delivered on the specimen surface. In the present work, the average laser power was measured before the mirror system (Figure 2.2) and average power P of the laser beam incident on the specimen surface was estimated by assuming a loss of approximately 15% of the radiation intensity due to the mirror system. The power measurement was mostly performed at 1 kHz pulse repetition rate.

Equations 2.2 and 2.3 show that D^2 is linearly dependent on $\ln(E_p)$ and w_0 can be estimated from a plot of D^2 versus $\ln(E_P)$. w_0 is calculated from the slope of a straight line obtained by fitting a linear function to the experimental data as follows:

$$w_0 = \sqrt{\frac{slope}{2}}. \quad (2.5)$$

From the calculated value of w_0, the average radiation fluence can be determined by

$$F_a = \frac{E_P}{\pi w_0^2} \quad (2.6).$$

The threshold fluence F_{th} can be derived from a plot of D^2 versus $\ln(F_a)$ (equations 2.2 and 2.3) by extrapolating D^2 to zero.

In most materials, the ablation threshold F_{th} decreases with increasing number of incident laser pulses, an effect known as incubation. It is explained by the formation of defects in the irradiated material even for sub-threshold fluences, which create electronic energy states within the energy gap, facilitating radiation absorption for subsequent laser pulses. The dependence of the ablation threshold F_{th} on the number of laser pulses N, can be expressed by the following equation proposed by Jee et al.[106]

$$F_{th}(N) = F_{th}(1).N^{S-1} \quad (2.7),$$

or

$$N.F_{th}(N) = F_{th}(1).N^{S} \quad (2.8),$$

where $F_{th}(N)$ and $F_{th}(1)$ are the ablation threshold values for N pulse and a single pulse, respectively, and S is the incubation factor of the material. According to equation 2.8, a straight line can be fitted to the plot of $\ln(N.F_{th}(N))$ versus $\ln(N)$, whose slope and intercept represent the incubation factor S and the logarithm of the single pulse ablation threshold, respectively.

2.2.2.b. Laser processing methods

In the present study, the laser experiments were performed using two irradiation strategies with stationary and non-stationary laser beam, respectively. In stationary conditions, craters were created at the surface of dentin and enamel specimens with numbers of laser pulses up to 150, pulse energies in the range 80 - 560 μJ and at 1 Hz pulse repetition rate. The measurement of the craters' diameter allowed determining the laser beam diameter at the surface of the specimen as well as the single pulse ablation threshold and the incubation factor of the tissue by the D^2 method. The evolution of the surface morphology as a function of the radiation fluence and number of laser pulses was also studied.

In non-stationary conditions, linear tracks were created by moving the specimens in the XX direction at a constant velocity in relation to the stationary laser beam, operated at high pulse repetition rates. In order to achieve large treated surface area for chemical analysis, the produced tracks were overlapped with a displacement dw in the YY direction between the linear scans. The scanning procedure is schematically described in Figure 2.3.

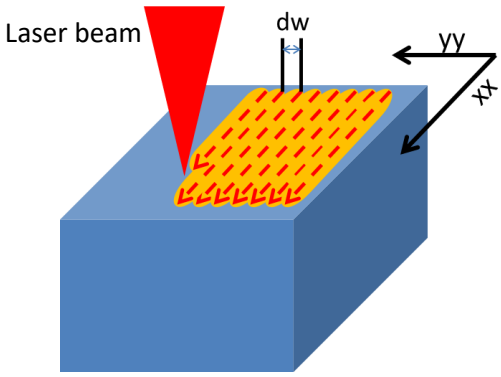

Figure 2.3: Schematic of the scanning procedure performed in non-stationary conditions.

For individual linear scans, the number of laser pulses incident on a particular surface position can be estimated by

$$N_{track} = \frac{2w_0 f}{v} \quad (2.9).$$

For the processing of large areas, the number of laser pulses per surface position must be calculated taking into consideration the overlapping of consecutive linear tracks. It is given by

$$N_{area} = \frac{4w_0^2 f}{v.dw} \quad (2.10).$$

In the present study, area treatments were performed with 5 mm/s scanning velocities, pulse energies in the range 80 - 560 mJ, 0.01 mm lateral displacement and 1 kHz pulse repetition rate. Most of the laser treatments were performed in air, except for some experiments on dentin which were performed with external cooling with lateral air jet and a combination of air jet and water irrigation. These external cooling methods were tested since they are commonly used to reduce heating of the teeth during clinical treatments for caries removal by mechanical drilling[63] and by Er:YAG and Er, Cr:YSGG lasers[124,125]. The air jet was provided by a 0.5 mm diameter nozzle, which directed air at a flow rate of $5*10^{-6}$ l/s to the laser spot location at the surface. The nozzle was at a distance of 1.5 mm from the laser spot and a 30º angle with the surface. The water irrigation system was similar to the one described by Cangueiro et al.[23], which allowed covering the specimens' surface with a 0.5 mm thick water layer. The water average flow rate and temperature were

$167*10^{-6}$ l/s and 23.5° C, respectively. To minimize the absorption of radiation by the water, during the ablation experiments water was blown away from the irradiated spot by the air jet but the surrounding area remained covered by the water film to ensure efficient cooling. A schematic diagram of the air and water-cooling systems is depicted in Figure 2.4. The laser processing conditions tested in the present work are summarized in Table 2.2.

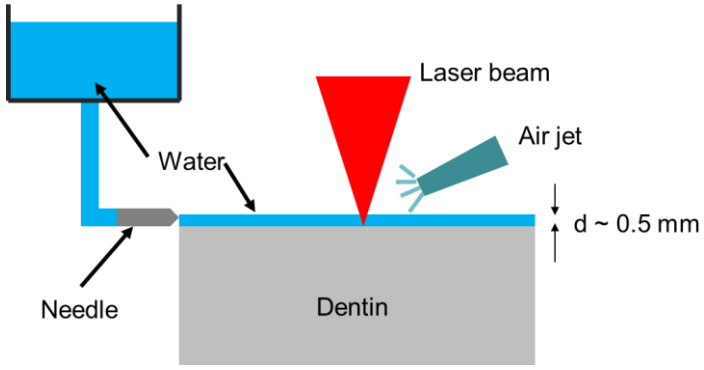

Figure 2.4: Schematic diagram of the external cooling set-ups tested.

Table 2.2: A summary of laser processing conditions tested in the present work

Laser processing parameters and conditions	
Average laser beam power	40 – 560 mW
Average pulse energy (E_p)	40 – 560 µJ
Lens – surface distance	9.7 cm
Average fluence ($F_{average}$)	2 – 14 J/cm^2
Pulse repetition rate (f)	1 and 1000 Hz
Scanning speed	5 mm/s
Lateral displacement	0.01 mm
Processing conditions	In air and with external cooling using air jet and water irrigation

2.2.2.c. Set-up for measurement of pulpal temperature during laser treatments

The temperature increase in the pulpal chamber during laser ablation of dentin was investigated by performing the laser treatments on healthy molars whose occlusal surfaces were polished up to a distance of 2 mm from the pulpal chamber. A K-type thermocouple with a tip diameter of 0.1 mm was inserted via one of the root canals until touching the pulp chamber wall directly below the treated surface. The thermocouple signal was measured by a digital thermometer (EL – USB – 1, Lascar Electronic ©, USA) once every 5 s. One tooth was laser treated without external cooling using fluences varying in the range 2 - 14 J/cm^2 to investigate the influence of the fluence on the temperature rise. The effect of external cooling was compared using a second tooth which was treated with an average fluence of 14 J/cm^2, without cooling and with external cooling by the air jet and water irrigation. The tested external cooling methods were described in Section 2.2.2.b. After each laser treatment the tooth was cooled to its initial temperature and rehydrated by irrigation with flowing water. The excess of water was removed with a clean absorbing paper tissue before the following laser treatment. The room temperature during these experiments was 23.5 ^{o}C.

2.2.2.d. Ablation rate measurement methods

In the present study, the ablation rate of enamel and dentin was measured in non-stationary mode. Linear tracks were created on the specimen surface with different pulse energies while keeping the same pulse repetition rate and scanning velocity. A white light interferometer (model WYKO NT1100, Veeco ©, USA) was used to measure volumes of the created tracks. The ablation rate r_a was determined by

$$r_a = v * \frac{V_a}{f * L_{track}} \quad (2.11),$$

where v is the scanning velocity, f the pulse repetition rate, V_a the ablation volume and L_{track} is the length of the track. In order to improve the precision of the ablation rate calculation, the ablation volume was measured at three areas along the linear tracks and the average value calculated.

2.3. Material characterization methods

The laser treated surfaces were characterized in terms of morphology, chemical constitution and crystallographic structure. The morphology of ablation surfaces was analyzed by scanning electron microscopy (SEM). The chemical constitution of laser treated surfaces was investigated by microRaman spectroscopy and Fourier transform infrared (FTIR) spectroscopy techniques. The crystallographic structure was studied by grazing incidence X-ray diffraction (GI-XRD) technique.

2.3.1. Scanning electron microscopy

Scanning electron microscopy (SEM) allows studying the morphology and the microstructure of material surface with high resolution. Therefore, it is a main technique used for analyzing the surface morphology of the laser treated surfaces. An intense electron beam is generated by the electron gun and focused on the specimen surface. The beam is scanned in a raster fashion across the surface of the specimen. A variety of signals is generated due to the interaction of the primary electron beam with matter, in particular secondary electrons, backscattered electrons and X-rays (Figure 2.5). Different signals have their origin in different regions of the sample and give specific information about the topography of the specimen surface and its chemical composition. Secondary electrons are produced when loosely bound atomic electrons are released due to interaction with the primary electrons. Secondary electrons have a small mean free path in the material due to their low energy. Therefore, they provide information from a shallow depth (10-100 nm) of the material. Backscattered electrons are formed by the scattering of primary electrons by nuclei of atoms in the specimen. The number of backscattered electrons increases with the atomic number of the atoms in the target and, hence, the resulting signal contains information on the target´s elemental composition. Because of the higher escape depth of backscattered electrons (up to several microns), this imaging mode provides lower resolution than the secondary electron imaging mode. Elemental microanalysis can also be carried out using the SEM. This relies on the detection of X-rays of

characteristic energy, which are emitted due to the interaction of the electron beam with atoms of different species. Since the incident beam has a large penetration depth and the X-rays have a large escape depth, this method of chemical analysis is significantly less surface sensitive than other techniques such as XPS, SIMS and AFM.

In this work, the scanning electron micrographs were acquired in the secondary electron imaging mode using a JEOL 7001F (JEOL ©, Tokyo, Japan) field-emission gun scanning electron microscope operated at an electron acceleration voltage of 10 kV. To avoid charging effects, the samples were coated with a gold-palladium film by direct current sputtering prior to observation. Electron micrographs were taken at magnifications in the range 50 – 10000 in order to visualize the surface morphology at different scales and at different positions on the specimen surface. For each laser processing condition three specimens were analyzed to confirm the reproducibility of the laser process. The EDX analysis was performed at 10 kV acceleration voltage and the generated X-ray was acquired with a light element EDX detector (Oxford Instrument ©, United Kingdom) to obtain reliable analysis results for light elements such as C and O. The ZAF correction was performed on the acquired EDX spectra by the integrated INCA software (Oxford Instrument ©, United Kingdom).

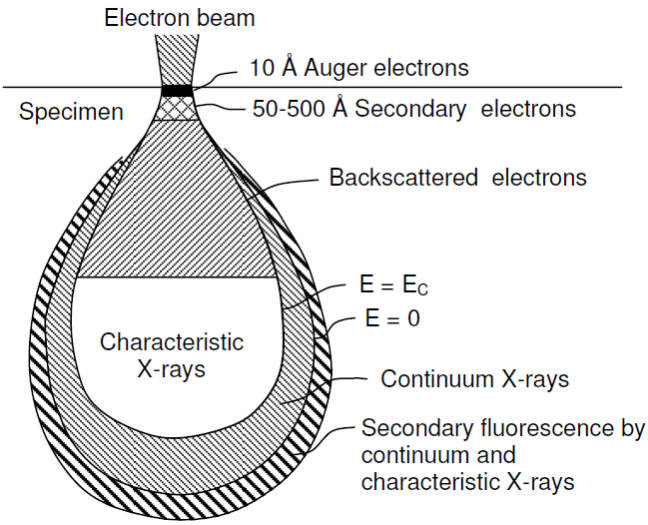

Figure 2.5: Generalized illustration of various electron- specimen interactions and the corresponding interaction volumes. Adapted from Lloyd[126].

2.3.2. X-ray diffraction

X-ray diffraction (XRD) is a non-destructive technique that allows identifying the crystallographic structure of a material based on the diffraction of X-rays by the crystallographic planes. As the incident X-ray radiation interacts with atoms in a material, it can be scattered by elastic scattering mechanism, forming spherical waves. Constructive interference of the scattered waves occurs if the Bragg law of diffraction is fulfilled, which can be expressed by the following equation

$$\mathbf{2d_{hkl}\sin\theta = n\lambda} \quad (2.12),$$

where d_{hkl} is the interplanar distance of planes in the {hkl} family, θ and λ the incident angle and wavelength, respectively, of the X-ray radiation, n is an integer number defining the order of the reflection.

The value of θ_{hkl} for which the diffraction occurs depend on the interplanar distances characteristic for the crystalline structure of the phases that constitute the material. On the other hand, the intensity of the diffracted beam depends on several factors including the atomic species present and the localization of atoms in the unit cell[127]. Consequently, constituent phases in a specimen can be identified by comparing diffraction peaks in its diffractograms with those of known materials. A compilation of diffractograms of a vast amount of materials can be found in ICDD cards (International Center for Diffraction Data).

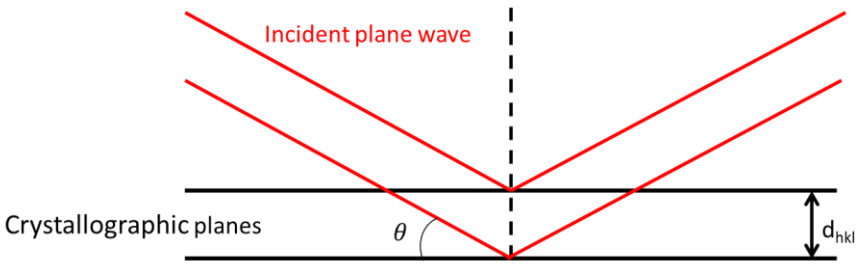

Figure 2.6: Diffraction of X-ray radiation by crystallographic planes with interplanar distance of d_{hkl}. The diffractive waves form constructive interference if the Bragg condition is satisfied.

In the present work, the grazing-incidence configuration was used for X-ray diffraction analysis due to its high sensitivity to the specimen surface region. The X-ray radiation was incident to the specimen surface at a small angle, which was fixed during the analysis while scanning the detector over a range of 2θ diffraction angle Figure 2.7. The intensity of the scattered signal can be expressed by[128]

$$I(z) = I_0 \exp(-\mu \left(\frac{z}{\sin \alpha} + \frac{z}{\sin(2\theta - \alpha)}\right) \quad (2.13),$$

where I_0 is the intensity of incident radiation, μ the absorption coefficient of the material, z the depth at which the diffracted radiation was generated, and α is the angle of incidence.

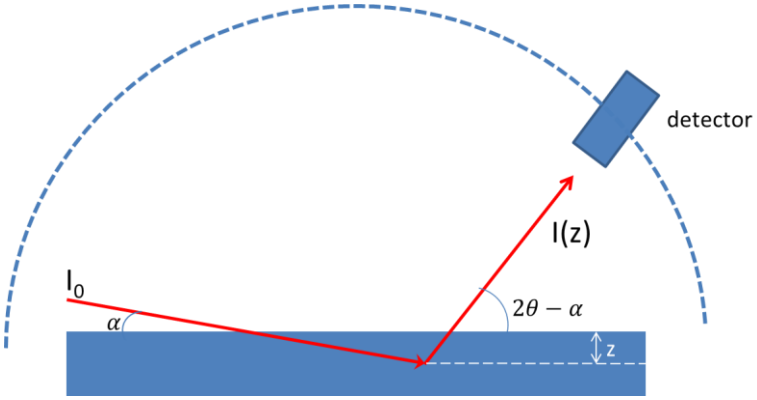

Figure 2.7: Configuration for grazing incidence X-ray diffraction analysis.

In the present work, the grazing incidence X-ray diffraction (GI-XRD) analysis was performed with Bruker D8 Advance diffractometer equipped with a Goebel mirror, using Cu Kα radiation (λ = 0.15418 nm), a mixture of two characteristic X-ray emission lines of Cu Kα1 (λ = 0.154056 nm) and Kα2 (λ = 0.154439 nm). The angle of incidence was fixed at 0.2°. The 2θ angle was varied in the range 10 to 80° with a step of 0.02° and acquisition time of 10 seconds per step. The evolution of scattered intensity with penetration depth with these experimental conditions is plotted in Figure 2.8. The calculation was performed using the absorption coefficient of cortical bone, a tissue with

similar chemical constitution as dental hard tissues, at 0.15418 nm (28.773 cm^{-1} [129]), and 2θ value of 31.73°, the angle at which the most intense diffraction peak of hydroxyapatite appears. Figure 2.8 indicates that intensity of the diffracted signal decreases rapidly with increasing depth and, therefore, most of the detected intensity is originated from a surface region of less than 5 μm thick with the aforementioned experimental conditions. For each laser processing condition two specimens were analyzed by the GI-XRD method.

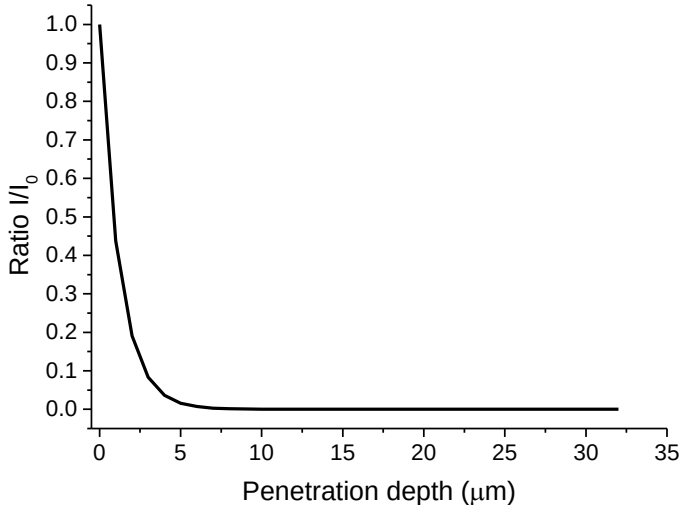

Figure 2.8: Evolution of scattered intensity with penetration depth in XRD analysis using grazing incidence configuration.

2.3.3. Vibrational spectroscopies

2.3.3.a. Raman spectroscopy

As radiation interacts with molecular structures in a material, it can excite the molecules to a virtual state, followed by their relaxation to the ground state leading to emission of photons with similar energies as the incident ones. Due to the conservation of the photon energy, the process is categorized as elastic scattering, which happens to a majority of incident photons. Besides, inelastic scatterings of photons, known as Stokes and anti-Stokes scattering, can take place with the involvement of phonons or change in vibrational state of the molecules. Stokes scattering leads to relaxation of the molecules to a higher vibrational state and, hence, emission of photon with lower

energy than the incident photon. On the contrary, for anti – Stokes scattering, the molecules are excited from a high vibrational state before relaxing to the ground state and the emitted photon has higher energy than the incident one. In principle, Stokes scattering has higher probability than anti-Stokes. Scattering phenomena in material is summarized in Figure 2.9.

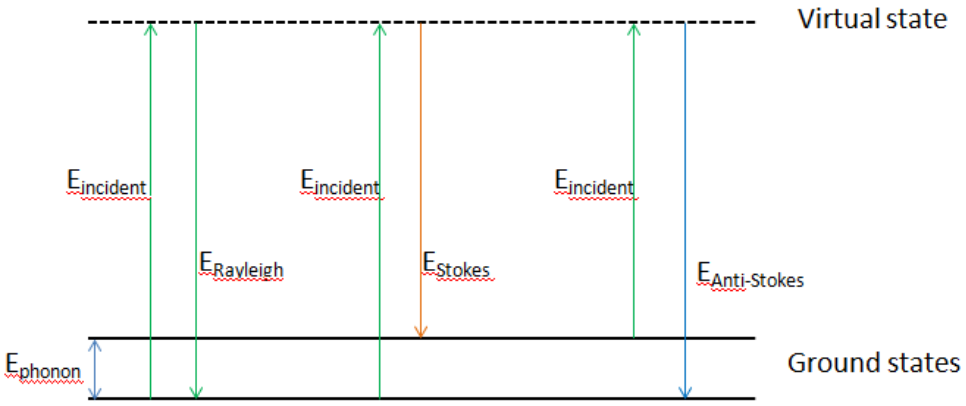

Figure 2.9: Possible scattering processes between incident photons and material.

In Raman spectroscopy, the molecules are excited by laser radiation and the scattered radiations are collected and analysed by a spectrometer. The radiation generated by Rayleigh scattering radiation is filtered out because of the lack of molecular information it contains and of its very high intensity. The difference in terms of photon energy between scattered photons and incident ones allows vibration energy states in a material to be determined. Compounds existing in a specimen can be identified by comparing the peaks observed in its Raman spectra with the spectra of known substances. Even though the Raman shift can be expressed in various units, wavenumber is the most commonly used. The wavenumber of the Raman shift is calculated as

$$\Delta\tilde{\nu}_{Raman} = \frac{1}{\lambda_{laser}} - \frac{1}{\lambda_{scattered}} \quad (2.14),$$

where λ_{laser}, $\lambda_{scattered}$ are the wavelengths of the laser source and of the scattered radiation, respectively.

In the present work, microRaman analysis was performed using a Horiba LabRAM HR800 Evolution (Jobin-Yvon ©, France) spectrometer. The instrument was coupled with a confocal optical microscopy system, allowing higher spatial resolution than conventional Raman systems. Radius of the laser spot on the specimen surface can be calculated by

$$w_{Raman} = 0.61\frac{\lambda}{\mathrm{NA}} \quad (2.15),$$

where λ and NA are wavelength of the excitation laser and numerical aperture of the microscope objective used, respectively. The depth of analysis is given by

$$\mathrm{d_{analysis}} = \frac{8w_{Raman}}{\mathrm{NA}} \quad (2.16).$$

A 50X objective with NA = 0.75 and a laser source with radiation wavelength of 532 nm were used in the present work, leading to a laser spot diameter of 0.87 μm and a depth of analysis of 4.62 μm. A 600 lines/mm grating spectrograph was used, allowing a resolution of 2 cm^{-1} to be achieved. Raman spectra were acquired with duration of 40 s and 20 accumulations. Several surface locations in each laser treated specimen were analysed to confirm the reproducibility of the laser treatment and of the analysis.

2.3.3.b. Infrared spectroscopy

Contrarily to Raman spectroscopy, infrared vibrational spectroscopy is based on the absorption of infrared radiation by molecules in a material. Due to the low photon energy in this spectral region, radiation absorption can only induce transitions between vibrational levels of a molecule. Consequently, information about the vibrational energy levels of a material can be obtained from its IR spectra.

In the present work, Fourier transform infrared spectroscopy (FTIR) analysis was performed in attenuated total reflectance (ATR) configuration. The IR beam is directed into a crystal with high refractive index, whose surface is in close contact with the sample's surface. The beam is reflected at the internal surface of the crystal, creating an evanescent wave travelling into the sample. The

evanescent wave is attenuated exponentially with increasing propagating distance. Some of its energy is absorbed by the sample and the reflected radiation is collected by a detector. Solid samples are usually clamped against the ATR crystal to minimize the presence of air trapped at the interface and enhance the propagation of evanescent wave in the samples.

In the present work, the FTIR analysis was performed with a Nicolet 5700 FTIR spectrometer (Thermo Electron Corporation ©, USA) equipped with a solid-substrate beam splitter and a deuterated triglycine sulfate thermoelectrically cooled detector. A diamond/ZnSe ATR crystal (n = 2.4) was used. The spectra were acquired in the mid-infrared region (400 – 4000 cm^{-1}) with a spectral resolution of 4 cm^{-1}. The final spectra were averaged from 512 accumulations. A schematic diagram of the ATR configuration used is displayed in Figure 2.10.

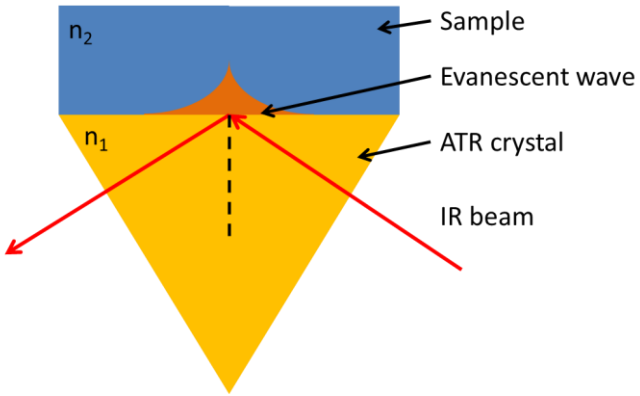

Figure 2.10: Schematic diagram of the ATR setup used in the present work.

Depth of penetration of the IR beam into the sample, defined as the distance required for the electric field amplitude to fall to e^{-1} of its value at the surface, can be calculated by

$$d_{analysis} = \frac{\lambda}{2\pi(n_1^2 sin^2\theta - n_2^2)^{1/2}} \quad (2.17),$$

where λ is the radiation wavelength, n_1 and n_2 the refractive indexes of the ATR crystal and sample, respectively, and θ is the incidence angle of the IR beam for the configuration used (θ = 42°).The evolution of the depth of penetration of the IR beam in dentin with wavenumber in the range 400 –

4000 cm^{-1} is plotted in Figure 2.11. The refractive index value for dentin of 1.54[130] was used and this value was assumed to be constant within the wavenumber range used. For each laser processing condition, three specimens were analyzed by the FTIR method.

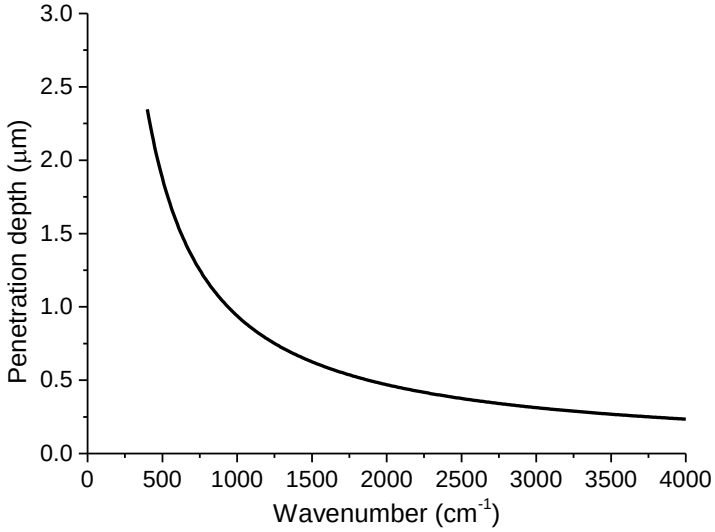

Figure 2.11: The evolution of IR beam penetration depth with wavenumber of the ATR configuration used in the present work.

2.4. Adhesion to laser-treated dentin surfaces

2.4.1. Sample preparation

Sixty non-carious human molars were selected, cleaned and embedded in epoxy resin (MA2+ ®, Presi ©, France), which could be hardened at room temperature. Plane dentin surface was obtained by cutting parallel to the occlusal surface and at a distance of approximately 3 mm with a low speed diamond saw (Accutom-50, Struers ©, Denmark). The exposed surface was polished using a 600 - 1000 - 2500 grit sequence of SiC papers. Polished specimens were stored at 4°C in sealed plastic bags with wet tissue papers to keep the teeth moist up to the surface preparation experiments.

The samples were randomly assigned into six groups (n=10) and three sets of surface treatment conditions were tested. The surface of the specimens in groups 1 and 2 were prepared by a tungsten carbide burr with a tip diameter of 1 mm rotating at 11000 rpm without water cooling. The burr

was linearly translated while being pressed on the specimen surface to create linear tracks, which were overlapped until full surface coverage was achieved. This drilling procedure was performed twice for the translation of the burr in xx and yy directions. Specimens in the remaining groups were treated with the femtosecond laser using the treatment procedure described in Section 2.2.2.b. Laser pulse energy of 80 μJ, corresponding to average fluence of 2 J/cm^2, was used for groups 3 and 4 while pulse energy of 560 μJ, corresponding to average fluence of 14 J/cm^2, was used for groups 5 and 6, representative of the range of average fluence tested in the present work. Treated specimens were rinsed in copious water flow; those treated with the laser were also ultrasonicated to remove redeposited ablation debris.

In the present study, the self-etch adhesive product Adhese Universal ® (Ivoclar Vivadent ©, Liechtenstein) was used for the adhesion test. The adhesive system contains a mixture of hydroxyethyl methacrylate (HEMA), decandiol dimethacrylate (D3MA), bisphenol A glycidyl methacrylate (bis-GMA), methacryloyloxydecyl dihydrogen phosphate (MDP) and methacrylated carboxylic acid polymer (MCAP) monomers. The adhesive resin has a pH value in the range 2.5 – 3.0, allowing it to be applied directly on dentin surfaces (self-etch mode) or with prior etching step (total-etch mode). Both application modes were tested in the present work. Groups 1, 3 and 5 were subject to self-etch mode and groups 2, 4 and 6 to total-etch mode. Etching of dentin surface was performed with a silica – thickened etching gel product (Scotchbond Universal Etchant ®, 3M Deutschland GmbH ©, Germany), which contains 32 wt.% phosphoric acid and has a pH value of approximately 0.1. The etchant was left on specimen surface for 15 s, according to the supplier's instructions, and rinsed with copious water flow. The adhesive liquid was firmly applied on the tooth surface with a brush tip, which was then rubbed on the specimen surface for 20 s. Excessive water in the adhesive layer was removed by drying with gentle oil – free air stream for 5 s. Polymerization was performed by using a LED device (Bluephase Style ®, Ivoclar Vivadent ©, Liechtenstein), which emits within the spectral range 385 – 515 nm and with power approximately

1000 mW, for 10 s. Afterwards, a vinyl ring with internal diameter and height of approximately 5 and 4 mm, respectively, was placed on the adhesive surface, filled with composite resin (Tetric Evoceram Bulk Fill ®, Ivoclar Vivadent ©, Liechtenstein). The composite resin was cured by the Bluephase Style LED device for 20s. The bonded specimens were stored again at 4°C in tightly sealed plastic bags containing a wet tissue paper to maintain a moist storage environment for 24 hours before the adhesion tests. The surface preparation and bonding procedures performed in the present study are presented in Figure 2.12. A digital photo of specimens prepared for adhesion tests is displayed in Figure 2.13.

Besides, the aforementioned surface treatment and bonding procedures were performed on dentin disks to investigate the adhesive – dentin interaction. Slices were extracted by cutting, with the diamond saw, bonded specimens in a plane perpendicular to the adhesive – dentin interface. They were polished with a 1000 – 4000 grit sequence of SiC papers and, then, with an alumina suspension (particle diameter ~ 0.04 μm). The slices were ultrasonicated to remove the abrasion debris and dehydrated before SEM observations.

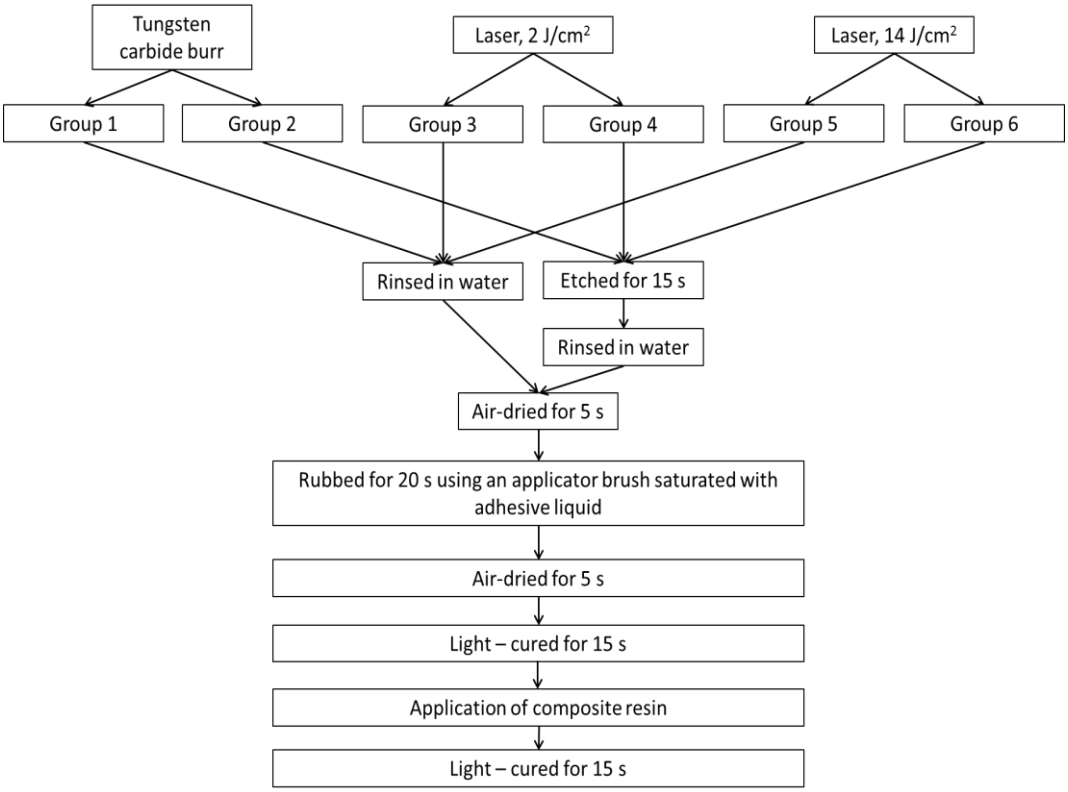

Figure 2.12: Schematic diagram for the surface preparation and bonding procedure performed for the adhesion test.

Figure 2.13: Photo of bonded specimens used for shear tests.

2.4.2. Shear tests and failure mechanism analysis

Bond strengths of the adhesive to treated dentin surfaces were evaluated by shear tests performed using a universal testing instrument (Model 5567, Instron Corp.©, USA). A 4 mm thick metallic plate was firmly fixed to the cross head of the testing instrument, and connected to the composite block bonded to dentin surfaces via a 5.5 mm diameter hole drilled in the plate (Figure 2.14). The metallic plate was moved at a constant velocity of 0.02 mm/s in a plane parallel to the bonded surface with increasing force applied by the instrument. The experiment was stopped once mechanical failures occurred in the specimens and the bond strength σ was determined by

$$\boldsymbol{\sigma = \frac{F_{failure}}{A}} \qquad (2.18),$$

where $F_{failure}$ is the applied force recorded when the failure occurs and A is the bonded area. Photos of the setup employed for the shear tests are displayed in Figure 2.15.

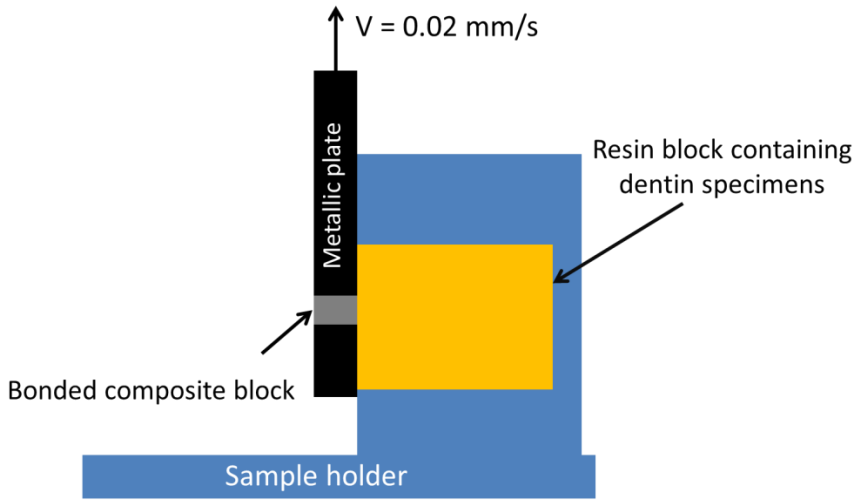

Figure 2.14: Schematic diagram of the setup used for shear tests.

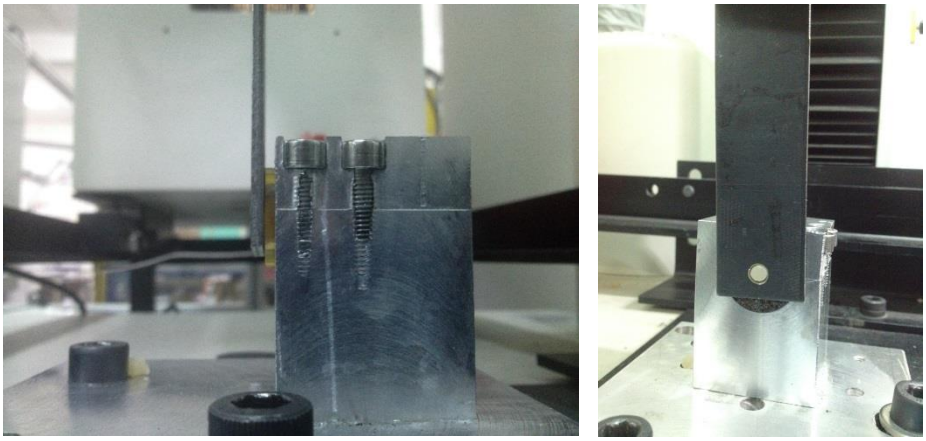

Figure 2.15: Digital photos of the setup used for shear tests.

After the shear tests, dentin disks were extracted from the tested specimens by cutting in a plane parallel to the fracture surface and at a distance of 2 mm. Morphology of fractured surfaces was investigated by SEM to study the predominant failure mechanisms. Failure mechanism was classified as cohesive (exclusive within dentin or resin composite), adhesive (mostly at the adhesive – dentin interface) or mixed[131].

3. Experimental results

In this chapter, major results obtained in this thesis are presented as follows:

- Characterization of craters created on enamel surface with stationary laser beam at 1 Hz pulse repetition rate, average fluence and number of laser pulses in the ranges 4 – 14 J/cm^2 and 5 – 75, respectively.
- Determination of the ablation threshold and of the incubation coefficient of enamel.
- Characterization of enamel surfaces treated by scanning the laser beam over the surface while pulsing the laser at 1 kHz pulse repetition rate, average fluences of 4, 9 and 14 J/cm^2 and scanning velocity of 5 mm/s.
- Characterization of craters created on dentin surface with stationary laser beam at 1 Hz pulse repetition rate, average fluence and number of laser pulses in the range 2 – 14 J/cm^2 and 5 – 150, respectively.
- Determination of the ablation threshold and of the incubation coefficient of dentin.
- Characterization of dentin surfaces treated by scanning the laser beam over the surface while pulsing the laser at 1 kHz pulse repetition rate, average fluences of 2, 7 and 14 J/cm^2 and scanning velocity of 5 mm/s.
- Measurement of pulpal temperature during laser treatment on dentin with 1 kHz pulse repetition rate, average fluences of 2, 7 and 14 J/cm^2, scanning velocity of 5 mm/s and treatment duration of 240s.
- Influence of external cooling on the increase of pulpal temperature and on morphology and chemical constitutions of laser treated dentin surfaces.
- Characterization of dentin surfaces prepared by a conventional tungsten carbide burr.
- Comparison of the adhesion of dental restorative materials to dentin surfaces prepared by femtosecond laser or carbide burr.

3.1. Ablation behavior of dental enamel

3.1.1 Laser experiments in stationary conditions

Craters were created on enamel surfaces with laser pulse energies and numbers of laser pulses varying in the ranges 160 – 560 μJ and 5 – 75, respectively. Diameters of the craters were measured on their SEM images and used for the determination of the ablation threshold of enamel by the D^2 method (Section 2.2.2.a). The morphology of the ablation surfaces was observed by SEM as well.

3.1.1a Ablation threshold and incubation coefficient

Figure 3.1 displays representative SEM images of craters created on enamel surfaces with laser pulse energies and numbers of laser pulses varying in the ranges 160 - 560 μJ and 5 – 75, respectively. The cracks occasionally observed on enamel surface are due to the dehydration process performed before SEM observation of the specimen and did not result from the laser treatment. Diameter of the craters was measured on these micrographs using ImageJ software (Bethesda, Maryland, USA)[132]. The laser spot diameter at $1/e^2$ the maximum intensity was determined from plots of the square of the craters' diameter as a function of the logarithm of laser pulse energy according to equations 2.2 and 2.5 (Section 2.2.2.a), leading to a value of 71 μm. Knowing this diameter, the average fluence could be calculated according to equation 2.6. The plots of the square of craters' diameter versus the average fluence for different numbers of laser pulses are depicted in Figure 3.2. The ablation thresholds were determined by extrapolating the D^2 to zero for each number of laser pulses. The evolution of ablation threshold with number of laser pulses is presented in Figure 3.3a. The observed decrease of ablation threshold with increasing number of laser pulses indicates the existence of an incubation effect, as described in Section 2.2.2.a. The relationship between the accumulated fluence $N*F_{th}(N)$ and number of pulses N, as expressed by equation 2.8, is depicted in Figure 3.3b. The slope of the line represents the incubation factor S. The

values of the single pulse ablation threshold and of the incubation coefficient of enamel determined are 2.72 ± 0.30 J/cm^2 and 0.74 ± 0.03, respectively.

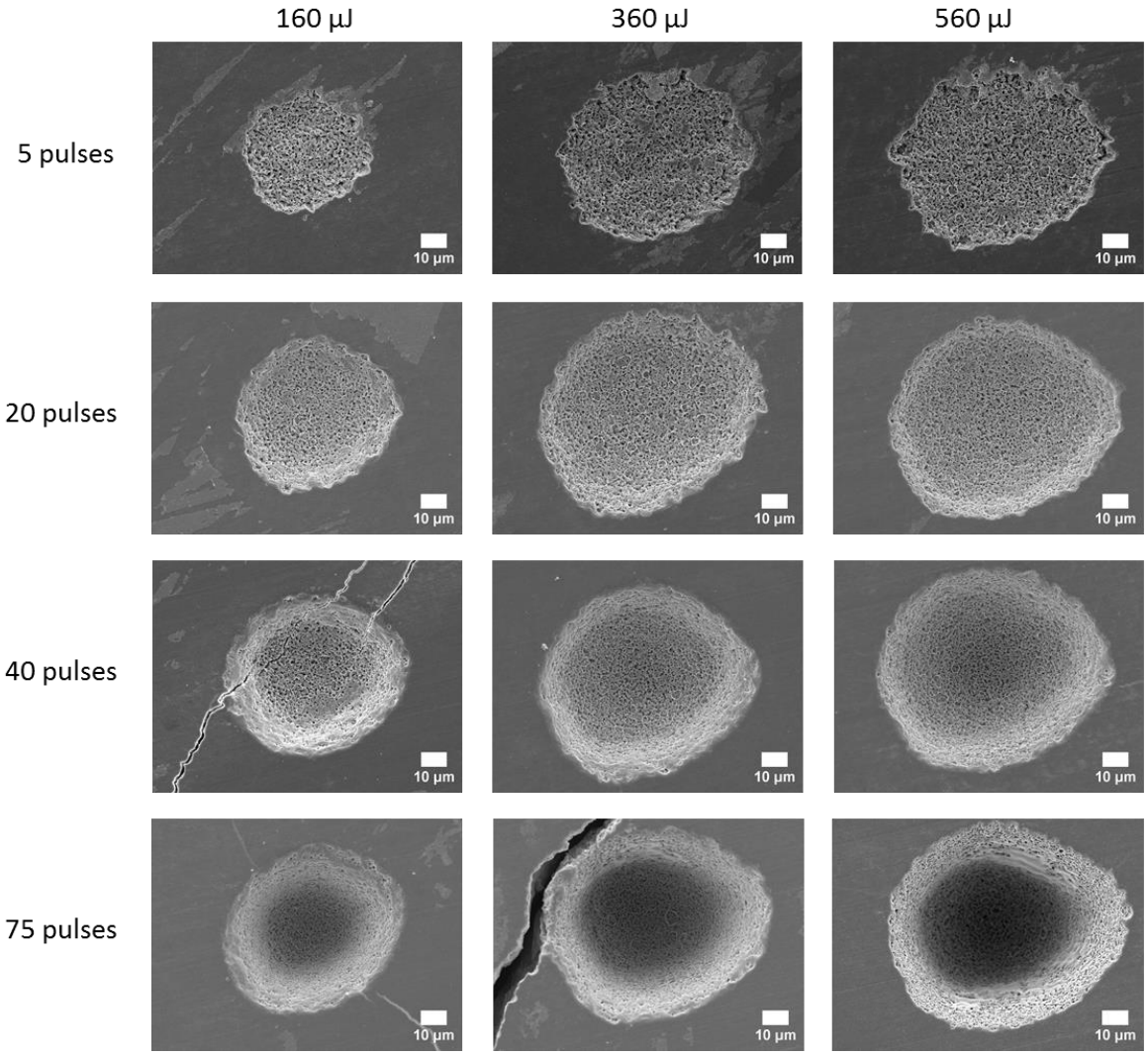

Figure 3.1: SEM images of craters created on enamel surface. The laser pulse energy and number of laser pulses were in the ranges 160 - 560 µJ and 5 – 75, respectively.

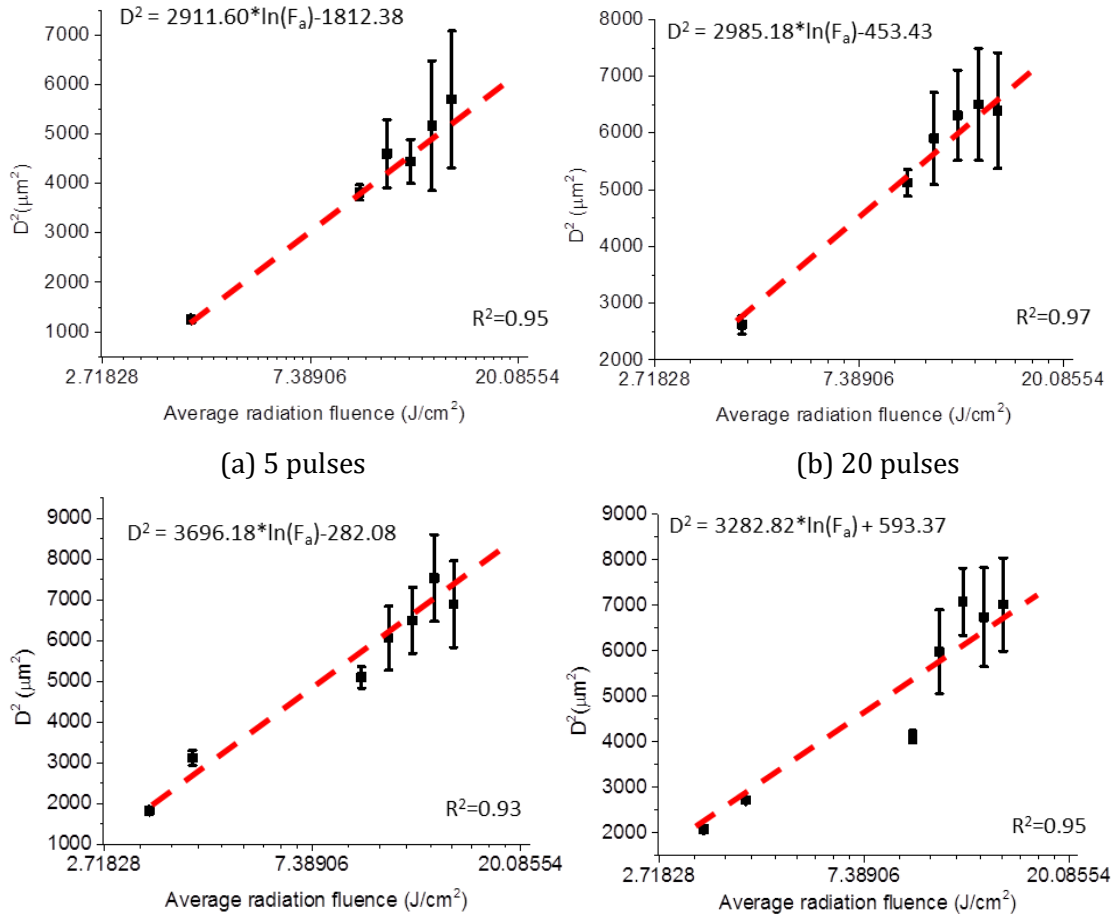

Figure 3.2: Semilogarithmic plot of D^2 as a function of the average fluence for each value of number of pulses. The lines are linear fitting of the experimental data. The R^2, slopes and intersection values resulting from each fitting are indicated.

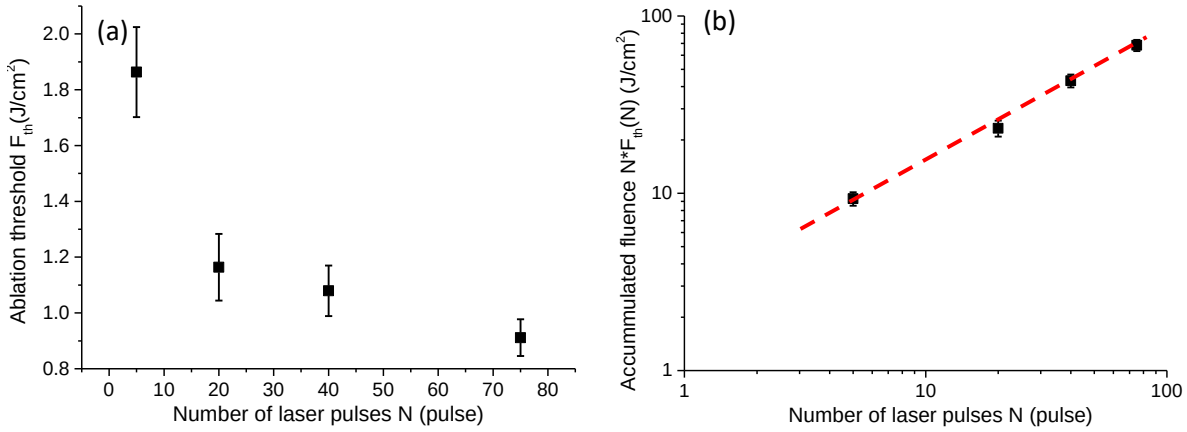

Figure 3.3: (a) Variation of the ablation threshold of enamel with number of pulses and (b) plot of the accumulated fluence versus number of pulses.

3.1.1b Morphology of ablation surfaces

High magnification SEM images of the craters created with a stationary laser beam are depicted in Figure 3.4 – 3.7. The craters are well-defined, with no significant alteration in the surrounding material. The ablation surface both at the center and at the periphery of the craters, is covered by a layer of resolidified material, indicating that melting of the hydroxyapatite in enamel occurred. This is true even for an average fluence as low as 4 J/cm^2 and 5 laser pulses (Figure 3.4a and b). It is worth emphasizing that this fluence is approximately two times higher than the ablation threshold, which is 1.86 ± 0.16 J/cm^2 for 5 laser pulses, as indicated in Figure 3.3. The layer of resolidified material presents round pores opening at the surface and traces of collapsed gas bubbles, showing that gases were released from the melted material, leading to the formation of bubbles that collapsed upon reaching the surface. It is likely that the released gas consisted of CO_2 and gaseous H_2O, generated by the decomposition of the carbonated hydroxyapatite present in dental enamel[133,134]. The morphology of the ablation surface is not significantly affected by the average fluence and the number of laser pulses.

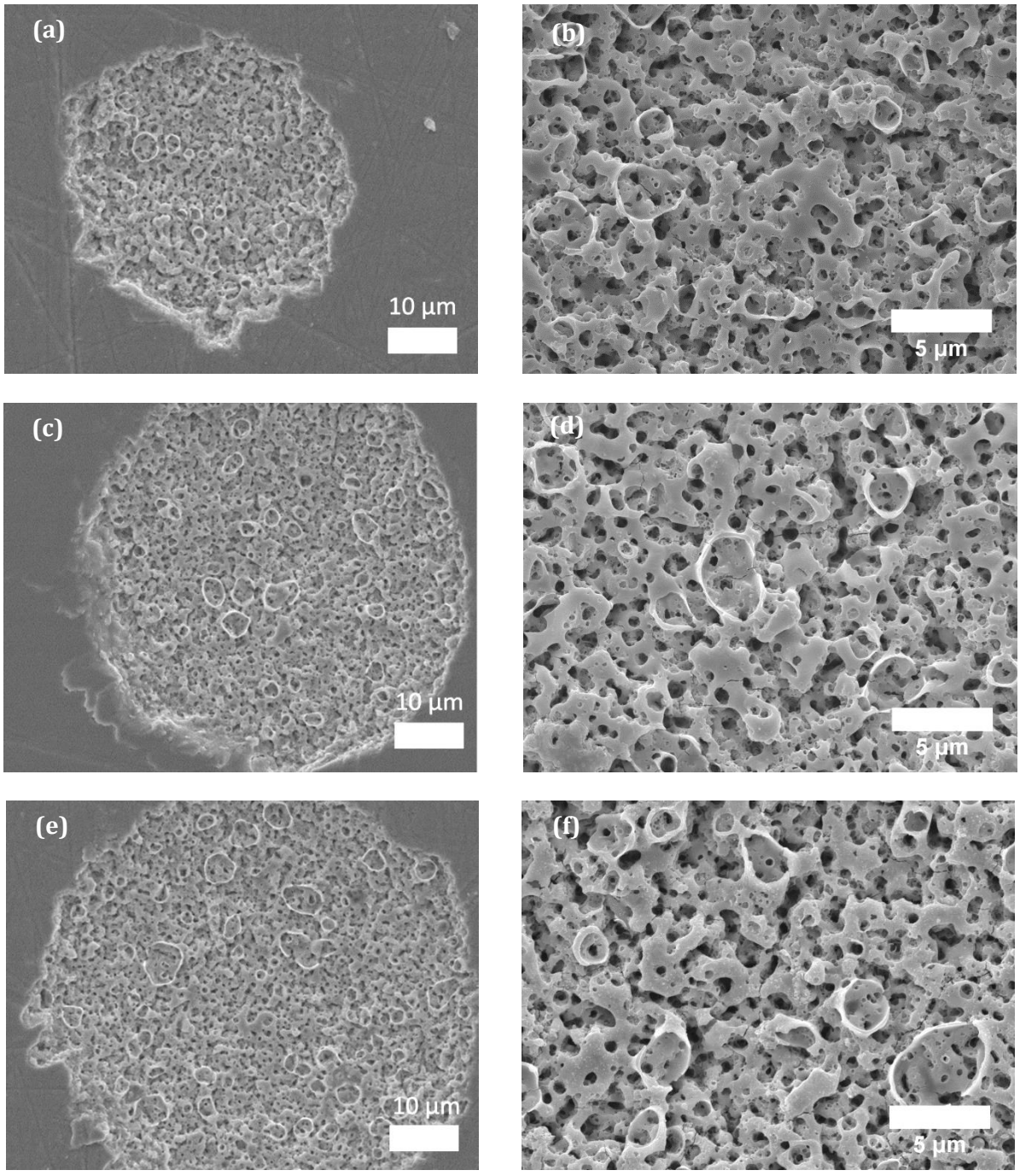

Figure 3.4: Morphology of craters created on enamel surface using 5 laser pulses with average fluences of 4 J/cm^2 (a, b), 9 J/cm^2 (c, d) and 14 J/cm^2 (e, f).

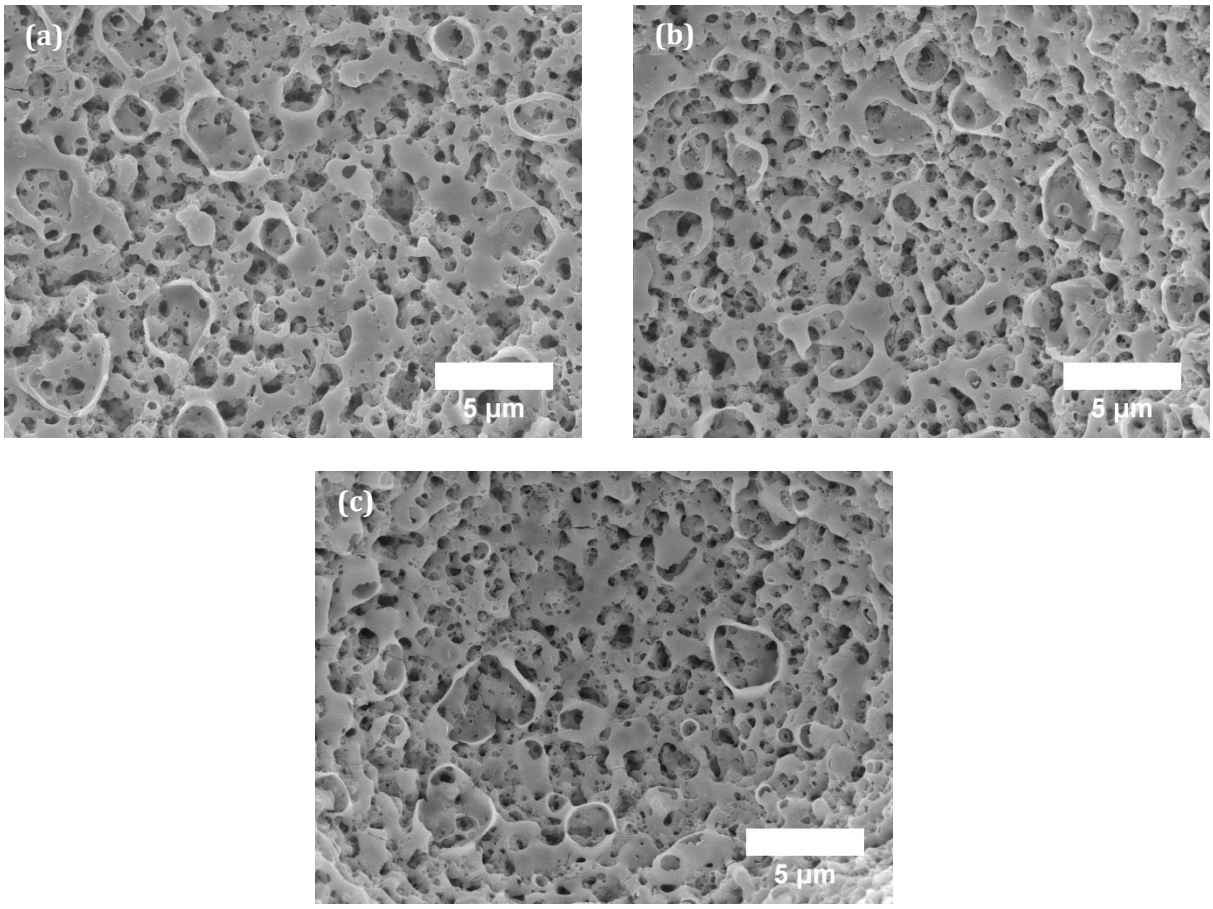

Figure 3.5: Morphology of craters created on enamel surface with average fluence of 4 J/cm^2 using 20 (a), 40 (b) and 75 (c) laser pulses.

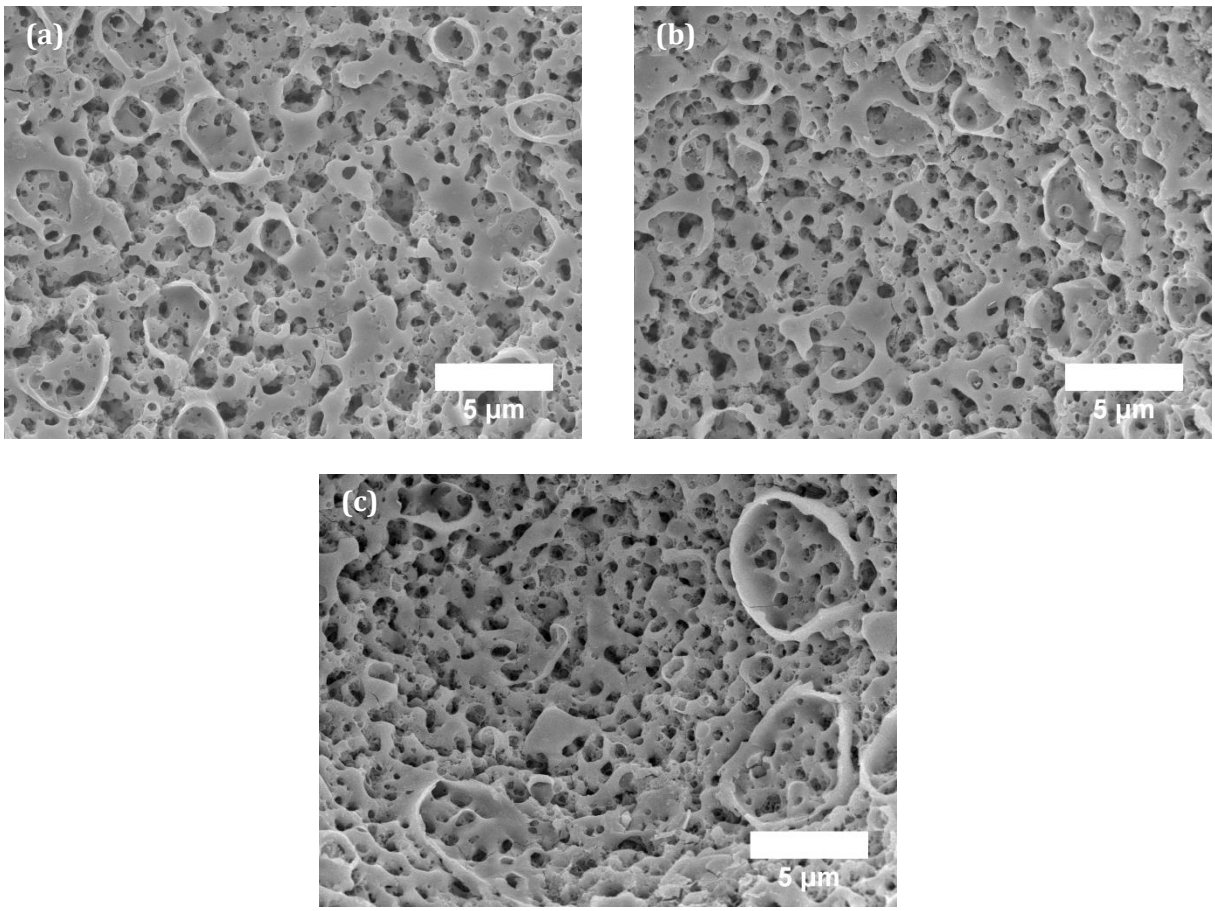

Figure 3.6: Morphology of craters created on enamel surface with average fluence of 9 J/cm^2 using 20 (a), 40 (b) and 75 (c) laser pulses.

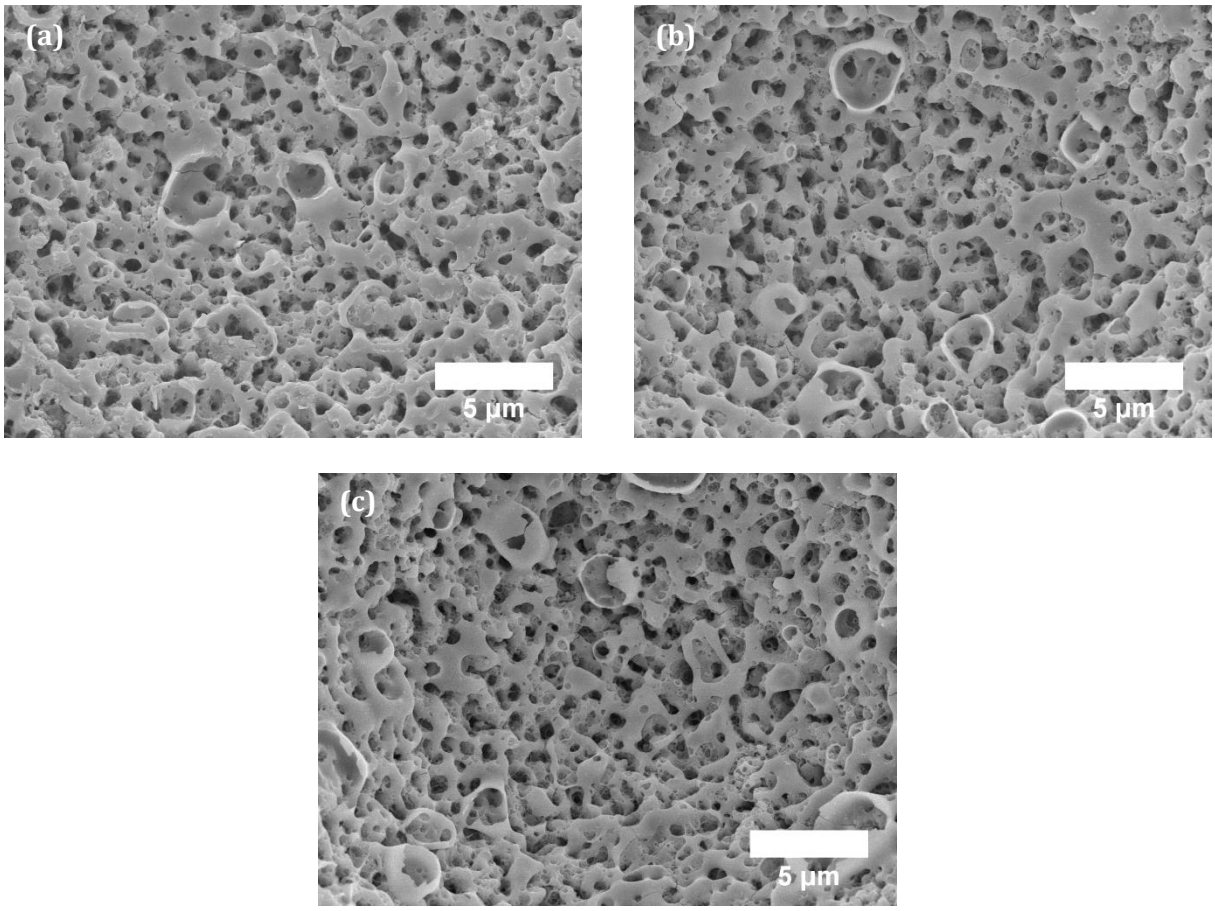

Figure 3.7: Morphology of craters created on enamel surface with average fluence of 14 J/cm^2 using 20 (a), 40 (b) and 75 (c) laser pulses.

3.1.2 Laser experiments in non-stationary conditions

This part of the study concerns laser experiments performed on enamel surfaces by moving the specimens at a velocity of 5 mm/s, while pulsing the stationary laser beam at a pulse repetition rate of 1 kHz. The ablation rate of enamel in these processing conditions was determined by calculating the volume of the linear tracks created on the specimen surface with different radiation fluences on the basis of white light interferometer surface profiles (Section 2.2.2.d). In this experiment, each surface location received 14 laser pulses. Large treated areas were also prepared for surface morphology and chemical constitution analysis by SEM and microRaman spectroscopy, respectively, by overlapping the linear tracks with a lateral displacement of 0.01 mm (Section 2.2.2.b). In these

conditions, the consecutive linear tracks were overlapped by 86%, taking into consideration that $2w_0$ equals 71 μm (Section 3.1.1), and each surface location received 100 laser pulses (equation 2.10).

3.1.2a Ablation rate

The evolution of the track's width with average fluence in the range 3 – 14 J/cm² is presented in Figure 3.8a in a semilogarithmic plot. The data show good agreement with equations 2.2 and 2.3 (Section 2.2.2.a), which describe the dependence of the diameter of craters ablated by a laser beam with a Gaussian intensity distribution on the average fluence. On the contrary, the variation of the track depth (Figure 3.8b) and of the ablated volume per laser pulse (Figure 3.9) with fluence show a rapid increase in the range 3 – 6 J/cm², followed by saturation at higher fluences. With the tested range of fluence, a maximum ablation rate of 25 * 10² μm³ per laser pulse is achieved for a fluence of 14 J/cm².

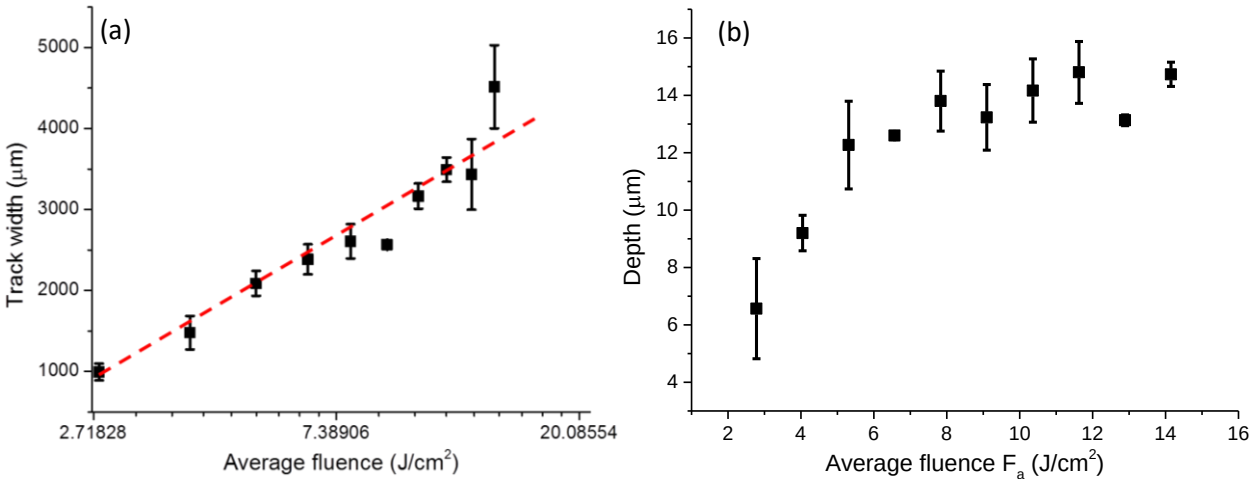

Figure 3.8: Widths (a) and depths (b) of the linear tracks created on enamel surface at 1 kHz pulse repetition rate, 5 mm/s scanning speed and fluences in the range 4 – 14 J/cm².

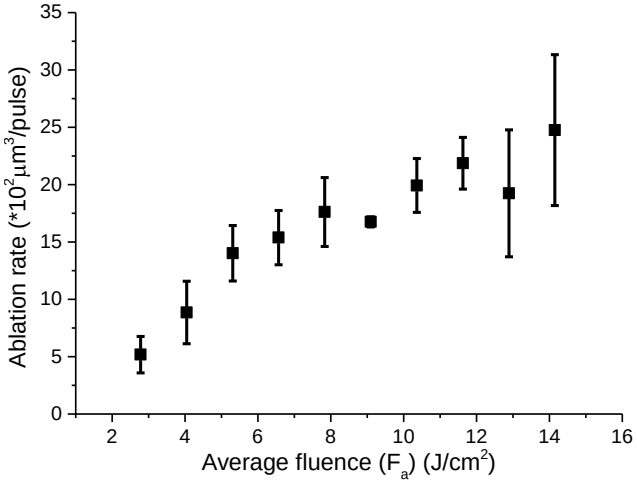

Figure 3.9: Evolution of ablation rate of enamel with radiation fluence.

3.1.2b Surface morphology

SEM micrographs of enamel surfaces treated with average fluence of 4, 9 and 14 J/cm^2, pulse repetition rate of 1 kHz and scanning velocity of 5 mm/s are depicted in Figure 3.10. Contrarily to the ablation surfaces produced at 1 Hz repetition rate (Figure 3.4 – 3.7), the morphology varies considerably when the laser beam is scanned continuously while pulsing at 1 kHz pulse repetition rate. In particular, the ablation surfaces produced at 1 kHz pulse repetition rate are covered by a large amount of redeposited resolidified droplets and ablation debris (Figure 3.10). The amount of redeposited material increases with increasing radiation fluence and aggregates with 3 – 4 µm, approximately, in diameter are observed in specimen treated with 14 J/cm^2 (Figure 3.10c). The layer of redeposited material is poorly adhered to the surface and can be easily removed by ultrasonication, exposing areas of resolidified material underneath (Figure 3.11). The observed morphology indicates that thermal effects play a more important role in the ablation of enamel in these processing conditions, leading to the ejection of a large amount of resolidified droplets and ablation debris, which aggregate into clusters and redeposit at the ablation surfaces.

Thickness of the molten layer that covers the laser treated surfaces was evaluated by fracturing the specimens in liquid nitrogen and observing their cross section by scanning electron microscopy. The

SEM micrographs are presented in Figure 3.12. In the specimens treated with 4 and 9 J/cm^2, the layer of resolidified material cannot be clearly distinguished and the enamel rods are observed at the proximity of the laser treated surface (Figure 3.12a and b). On the contrary, a surface layer of resolidified material can be clearly observed in the specimen treated with 14 J/cm^2 (Figure 3.12c). This layer presents a uniform structure and traces of bubbles of gas as a result of the decomposition of hydroxyapatite during laser treatment. The thickness of the resolidified layer varies significantly from place to place, reaching a maximum value of 1.5 μm in some locations.

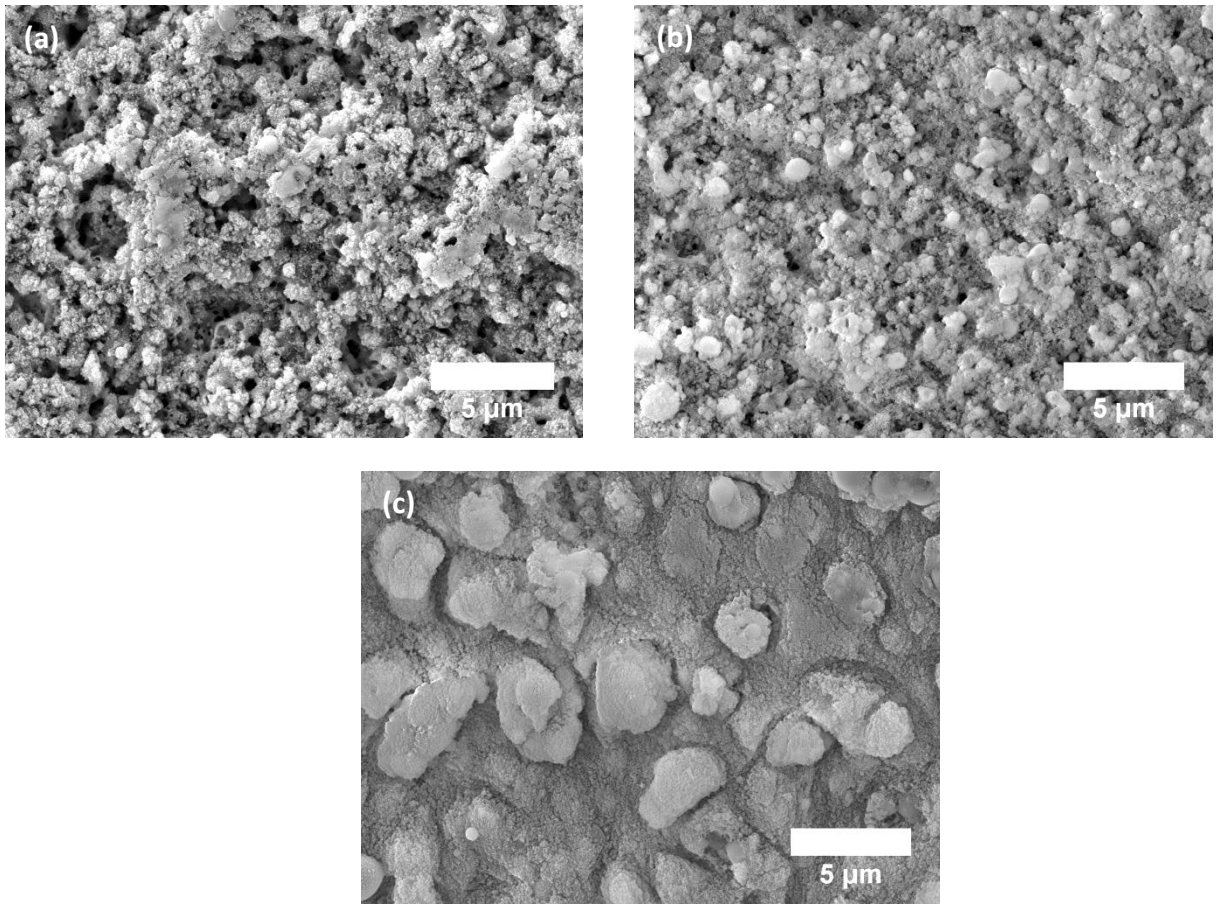

Figure 3.10: SEM micrographs of enamel surface treated with 1 kHz pulse repetition rate, 5 mm/s scanning velocity and fluences of 4 J/cm^2 (a), 9 J/cm^2 (b) and 14J/cm^2 (c).

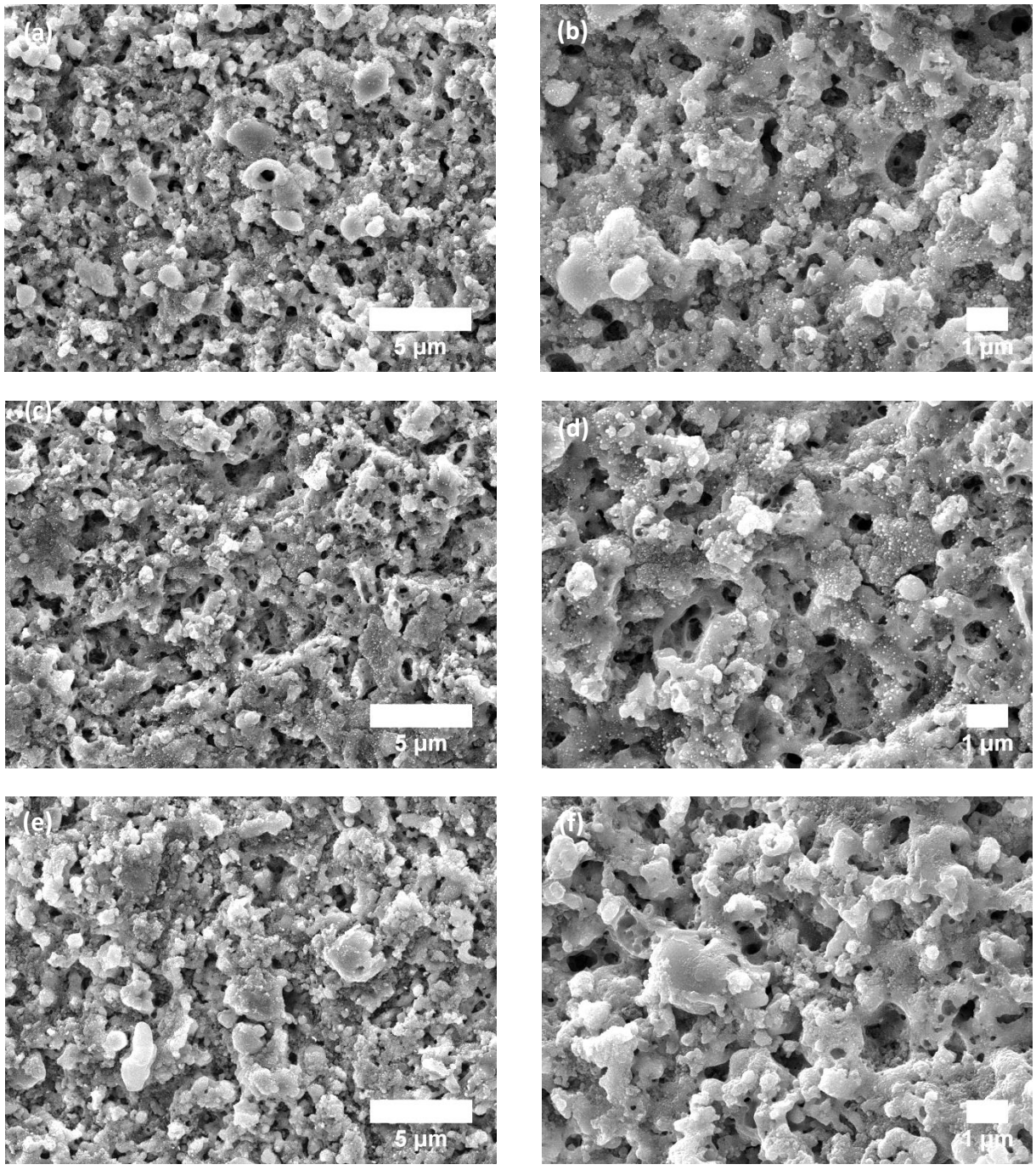

Figure 3.11: Morphology of laser treated enamel surfaces after ultrasonication. The laser treatment were performed with pulse repetition rate of 1 kHz, scanning velocity of 5 mm/s and fluences of 4 J/cm^2 (a, b), 9 J/cm^2 (c, d) and 14 J/cm^2 (e, f).

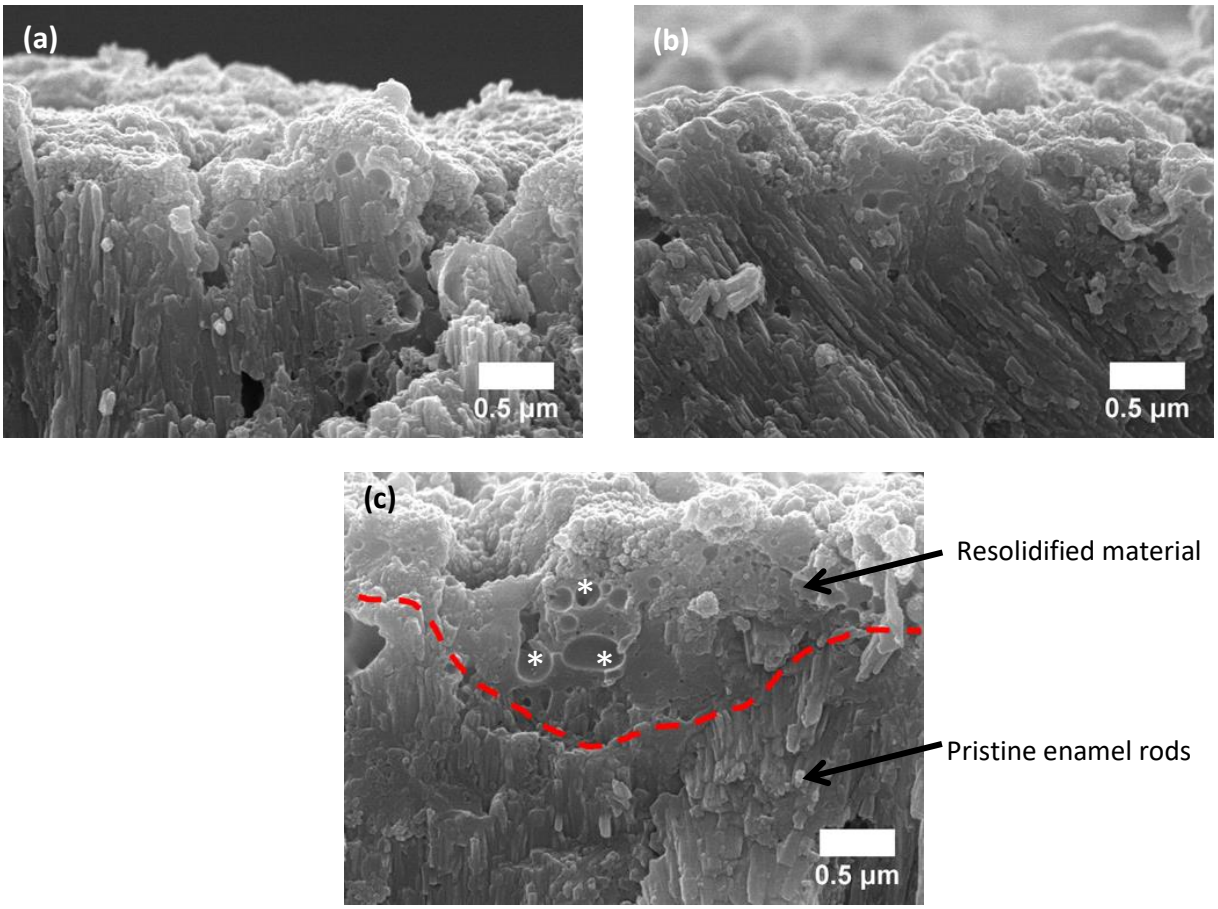

Figure 3.12: SEM micrographs of the cross section of enamel surfaces treated with 1 kHz pulse repetition rate, scanning velocity of 5 mm/s and average fluences of 4 J/cm^2 (a), 9 J/cm^2 (b) and 14 J/cm^2 (c). The border between the resolidified material layer and unaltered enamel structure observed in specimen treated with 14 J/cm^2 is indicated by a red dashed line. Traces of bubbles formed during melting of hydroxyapatite are marked by asterisks (*).

3.1.2c X-ray diffraction

The phases present in the laser treated enamel surfaces were analyzed by grazing incident X-ray diffraction. The diffractograms of polished and laser treated enamel surfaces are shown in Figure 3.13. All the peaks observed in the diffractogram of the polished specimen can be indexed as belonging to a non-stoichiometric hydroxyapatite, according to ICDD card number 9-432[135]. No new peaks are observed in the diffractograms of the laser treated specimens despite the presence of the

resolidified material layer formed by melting of the hydroxyapatite. All the peaks observed can be assigned to non-stoichiometric hydroxyapatite. No peaks that correspond to phases resulting from the thermal decomposition of hydroxyapatite are observed. This result does not mean that no decomposition of hydroxyapatite occurred. The absence of the new phases can be explained by the fact that the thickness of the resolidified material, < 1.5 μm as depicted in Figure 3.12, is much lower than the depth of analysis of the GI-XRD technique used, which was estimated to be 5 μm (Section 2.3.2).

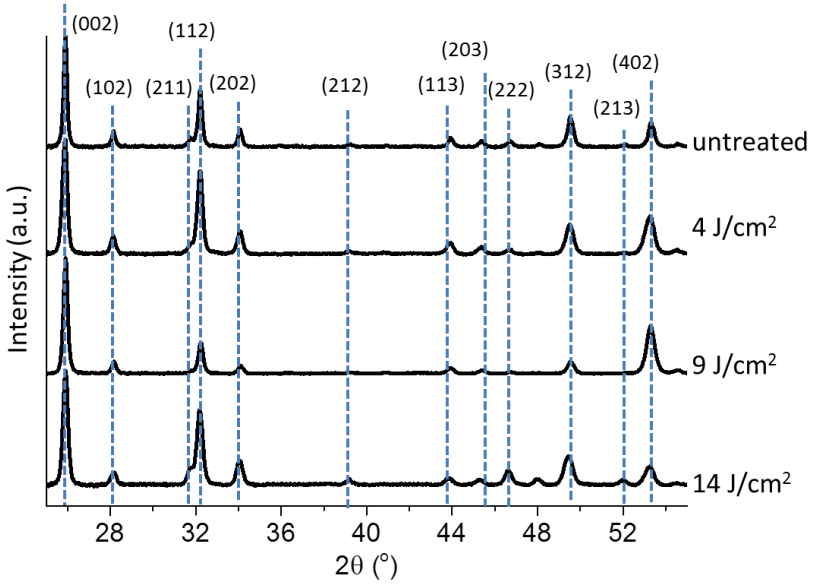

Figure 3.13: Diffractograms of polished and laser treated enamel. Angle of incidence: 0.2°. The indexed peaks correspond to hydroxyapatite.

3.1.2d Chemical constitution

The chemical constitution of the laser treated enamel surfaces was investigated by microRaman spectroscopy. The Raman spectra of the laser treated specimens and the spectrum of a polished sample, all normalized to the largest amplitude peak, at 960 cm^{-1}, are shown in Figure 3.14. The peak at 960 cm^{-1} corresponds to the ν_1 vibration of the phosphate group in hydroxyapatite[14]. The bands at 440, 580 and 1025 – 1085 cm^{-1} can be assigned to the ν_2, ν_4 and ν_3 vibrational modes of the phosphate group[136–138]. A peak at 1070 cm^{-1}, which corresponds to the ν_1 vibration of the carbonate

group [14,33], is also observed due to the partial replacement of the hydroxyl and phosphate anions in the hydroxyapatite lattice by carbonate anions. The band assignments for the Raman spectrum of enamel are summarized in Table 3.1.

Table 3.1: Band assignments of enamel Raman spectra[137]

Peak position (cm^{-1})	Assignment
440	ν_2 mode of PO_4^{3-}
580	ν_4 mode of PO_4^{3-}
960	ν_1 mode of PO_4^{3-}
1033	ν_3 mode of PO_4^{3-}
1070	ν_1 mode of CO_3^{2-}

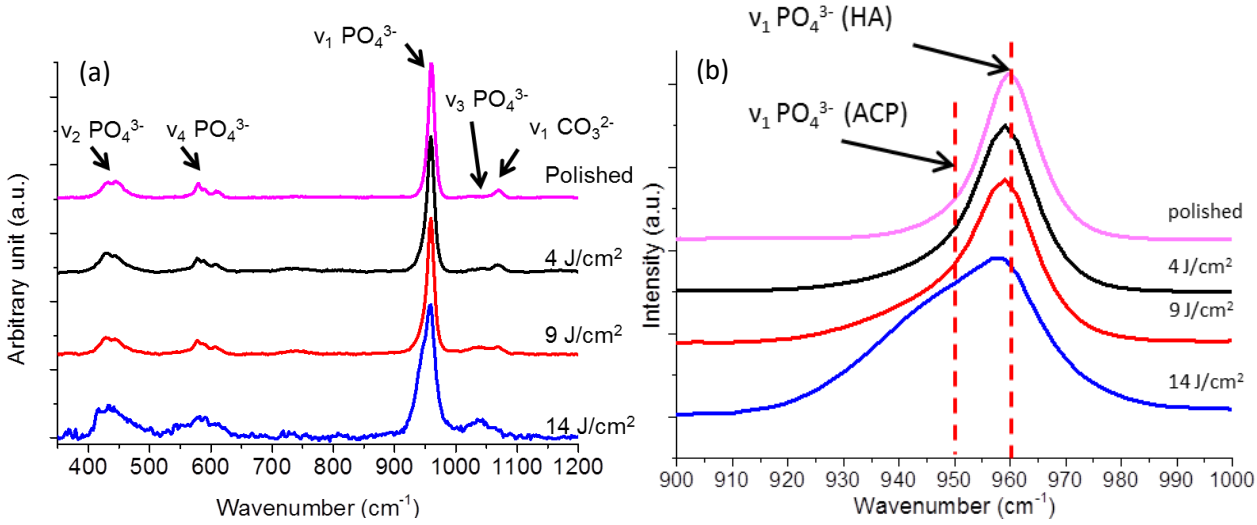

Figure 3.14: Raman spectra of polished and laser treated enamel (a) and a magnified view of the spectral range 900 – 1000 cm^{-1}. Positions of the peaks corresponding to ν_1 mode of PO_4^{3-} in hydroxyapatite (HA) and amorphous calcium phosphate (ACP) are indicated.

Figure 3.14a reveals that the relative intensity of the ν_1 peak of PO_4^{3-} decreases with increasing fluence, indicating that nanocrystalline and/or amorphous calcium phosphate (ACP) is formed in the enamel surfaces due to the laser treatment[139,140]. The presence of ACP is confirmed by an increase of the relative intensity in the region around 950 cm^{-1} in the laser treated specimens, especially with 14 J/cm^2 as compared to the untreated specimen spectrum (Figure 3.14b). After ultrasonication, Raman spectra of laser treated specimens become similar to the spectrum of polished specimen, as depicted in Figure 3.15. This result indicates that ACP is mainly concentrated in the redeposited ablation debris, which were removed by the ultrasonication (Figure 3.11), and that the chemical constitution of underlying structure is similar to that of pristine enamel. The chemical constitution of the layer of resolidified material could not be successfully analyzed due to its very low thickness (< 1.5 µm) as compared to the probing depth of the microRaman technique used (4.62 µm, Section 2.3.3.a).

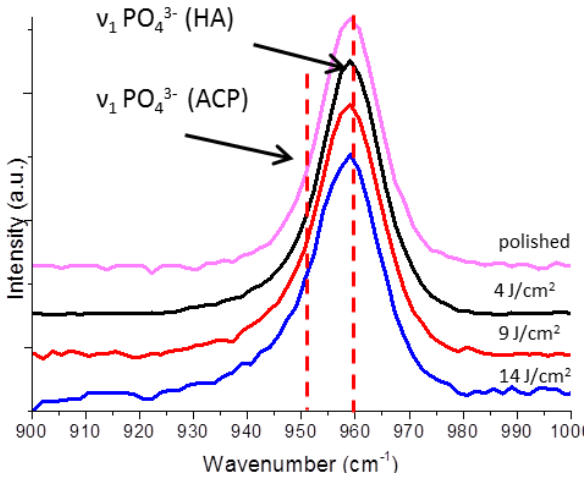

Figure 3.15: Raman spectra of polished and laser treated specimens after ultrasonication.

3.2. Femtosecond laser ablation of dentin

3.2.1. Laser experiments in stationary conditions

Craters were created on dentin surfaces with laser pulse energies and numbers of laser pulses varying in the ranges 40 - 560 µJ and 5 – 150, respectively. The pulse repetition rate of 1 Hz was

used. SEM observations were performed to analyze the morphology of the ablation surfaces as well as to measure the craters' diameters for the determination of dentin ablation threshold and incubation coefficient.

3.2.1.a. Ablation threshold

SEM micrographs of craters created on dentin surface with the stationary beam are presented in Figure 3.16, which allow the craters diameter to be measured. The average fluence was determined from the laser pulse energy using equation 2.6 with a value of laser spot diameter at its $1/e^2$ maximum intensity of 71 μm, this value is similar to the one calculated for enamel because the focusing lens – specimen distance was similar in both cases. The plots of the square of craters' diameter versus the average fluence for different numbers of laser pulses are depicted in Figure 3.17. A linear dependence can be observed at low average fluences (F_a = 1 – 4 J/cm^2), whose slope is compatible with a laser spot diameter of 71 μm. On the contrary, the craters produced with high average fluences (F_a > 4.5 J/cm^2) and high number of pulses (N>40) present diameters smaller than the values predicted by equation 2.2. This deviation is not due to the difference in ablation mechanism since the SEM micrographs of the perimeter of the craters produced at high fluences and high number of pulses present a morphology similar to the morphology of craters produced at lower fluences and lower number of laser pulses. Instead, it might be explained by the influence of ablation debris, which are ejected by the laser ablation and redeposit on the surface surrounding the craters at the end of each ablation process. The redeposited debris can absorb the subsequent laser pulse, reducing the radiation fluence available for the ablation of the underlying dentin. The absence of this effect for low fluences and low numbers of laser pulses is probably due to the negligible amount of redeposited material in this case. The amount of redeposited ablation debris only becomes significant with high fluence and high number of laser pulses.

Due to this inconsistency, the linear functions displayed in Figure 3.17 were only fitted for data points within the average fluence range 1 – 4 J/cm^2. The ablation thresholds values were determined by extrapolating plot of D^2 versus fluence to zero. The evolution of ablation threshold with the number of laser pulses is presented in Figure 3.18a. The ablation threshold decreases for increasing number of laser pulses, indicating the existence of an incubation effect in dentin. The relationship between the accumulated fluence $N*F_{th}(N)$ and the number of laser pulses N, as expressed by equation 2.8 (Section 2.2.2.a), is depicted in Figure 3.18b. The values of the single pulse ablation threshold and of the incubation coefficient of dentin determined from this equation are 1.49 ± 0.13 J/cm^2 and 0.79 ± 0.01, respectively.

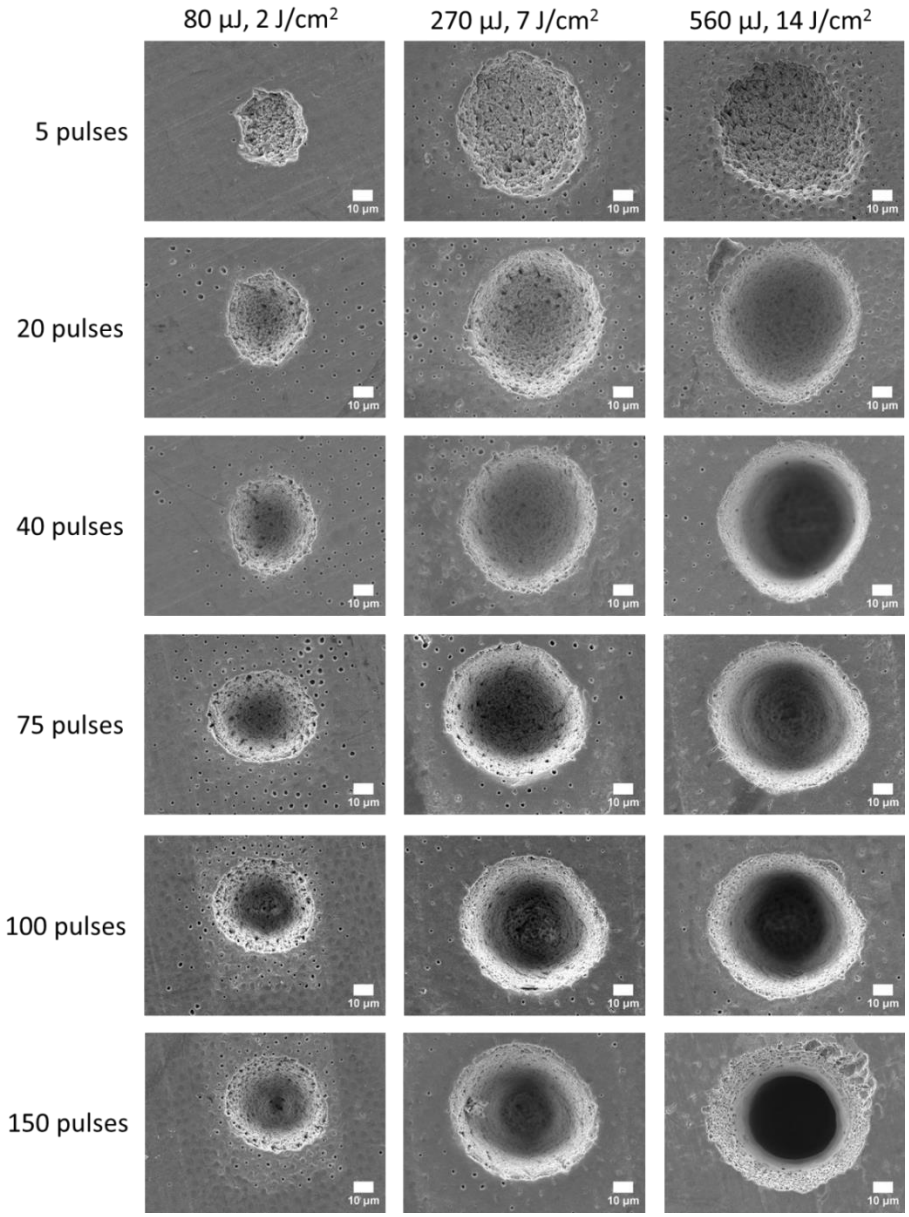

Figure 3.16: SEM micrographs of craters ablated on dentin surface at 1 Hz pulse repetition rate.

Number of laser pulses, laser pulse energy and corresponding average fluences are indicated.

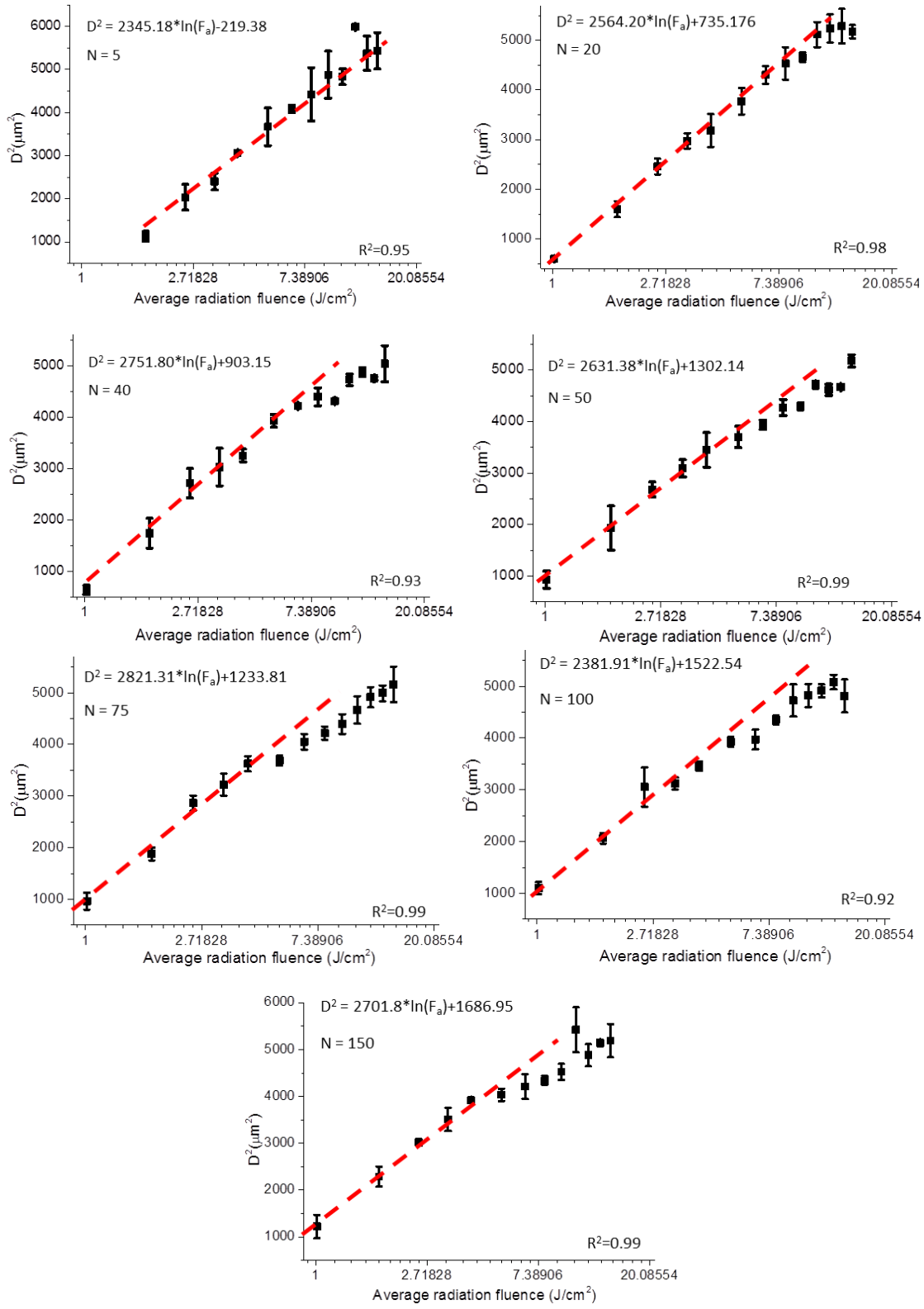

Figure 3.17: Semilogarithmic plot of D^2 as a function of the average pulse energy for each number of pulses. The lines are linear fitting of the experimental data. The R^2, slopes and intersection values resulting from each fitting are indicated.

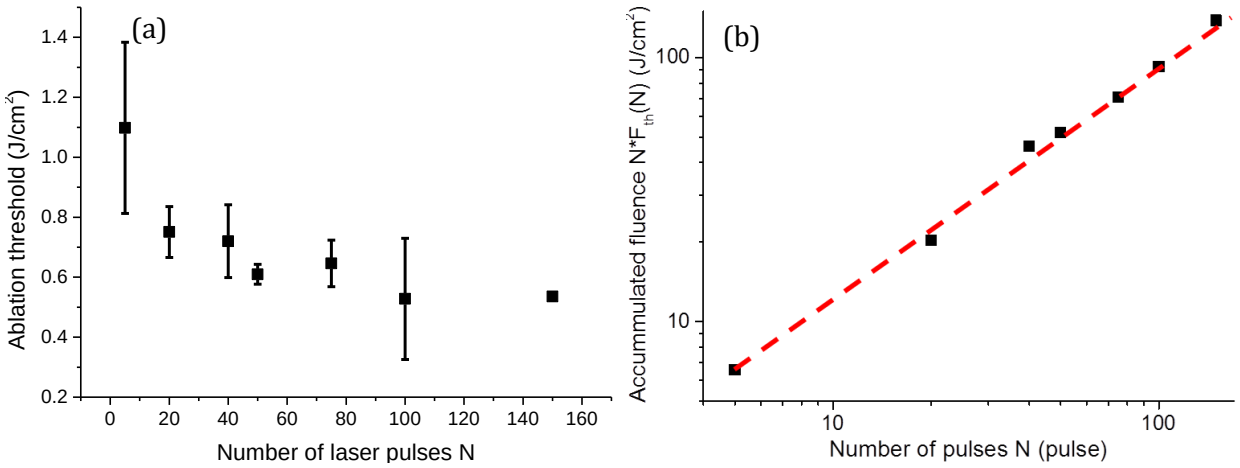

Figure 3.18: (a) Variation of the ablation threshold with number of pulses and (b) plot of the accumulated fluence versus number of pulses.

3.2.1.b. Surface morphology

SEM micrographs of the craters produced on dentin surface with 5, 20 and 40 laser pulses, average fluences of 2, 7 and 14 J/cm^2 and at a pulse repetition rate of 1 Hz are depicted in Figure 3.19– 3.21. The ablation surfaces show no sign of resolidified material. The original structure of dentin, with hydroxyapatite nanocrystals and open dentinal tubules can be clearly observed, regardless of the radiation fluence and number of laser pulses used. The result indicates that the influence of thermal effects on the ablation of dentin is negligible, contrarily to the ablation of enamel, which involves melting of the surface for the same fluence range, as presented in Section 3.1.1b. In addition, no mechanical damage of the tissue is observed. The sub-micron sized cracks occasionally observed in the peritubular dentin are probably due to the dehydration process performed before SEM observation.

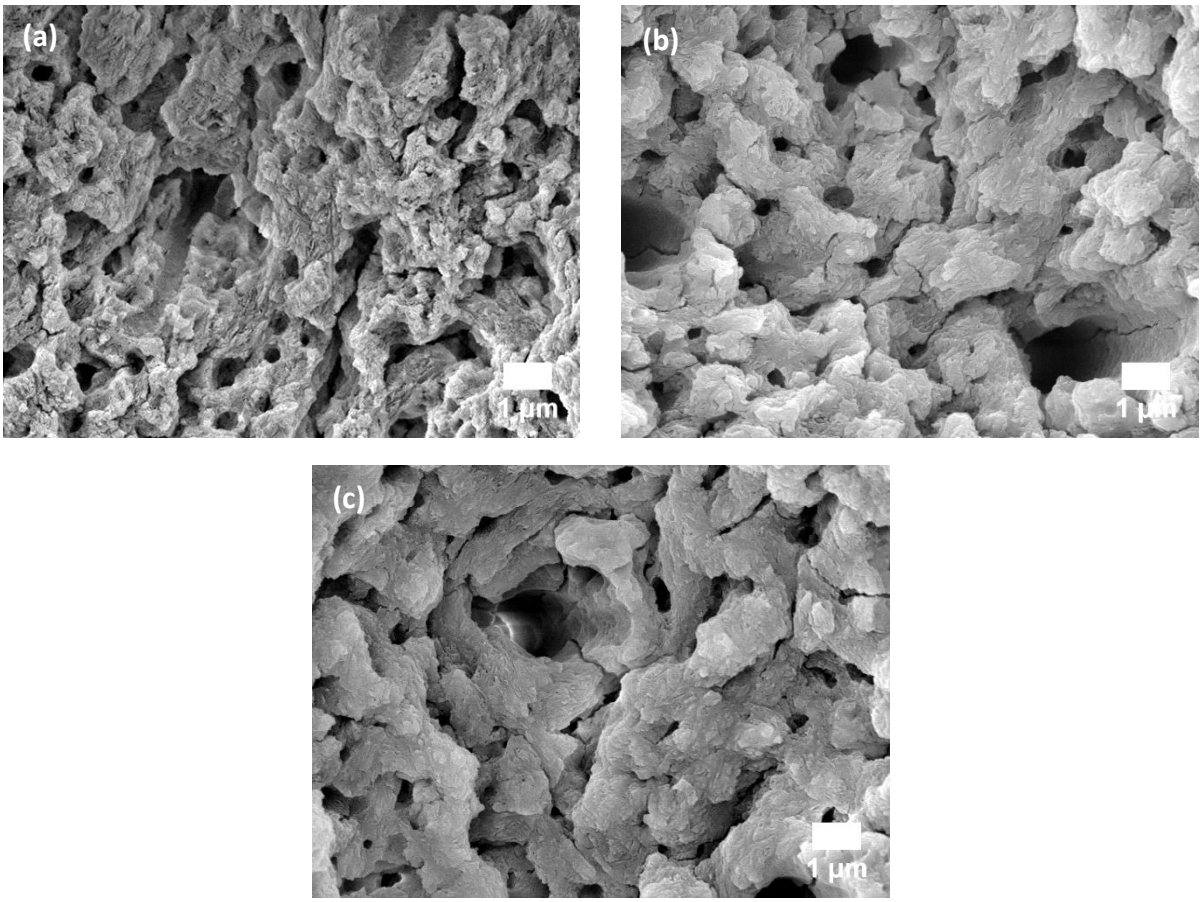

Figure 3.19: Morphology of craters created on dentin surface with fluence of 2 J/cm^2 and with 5 (a), 20 (b) and 40 (c) laser pulses.

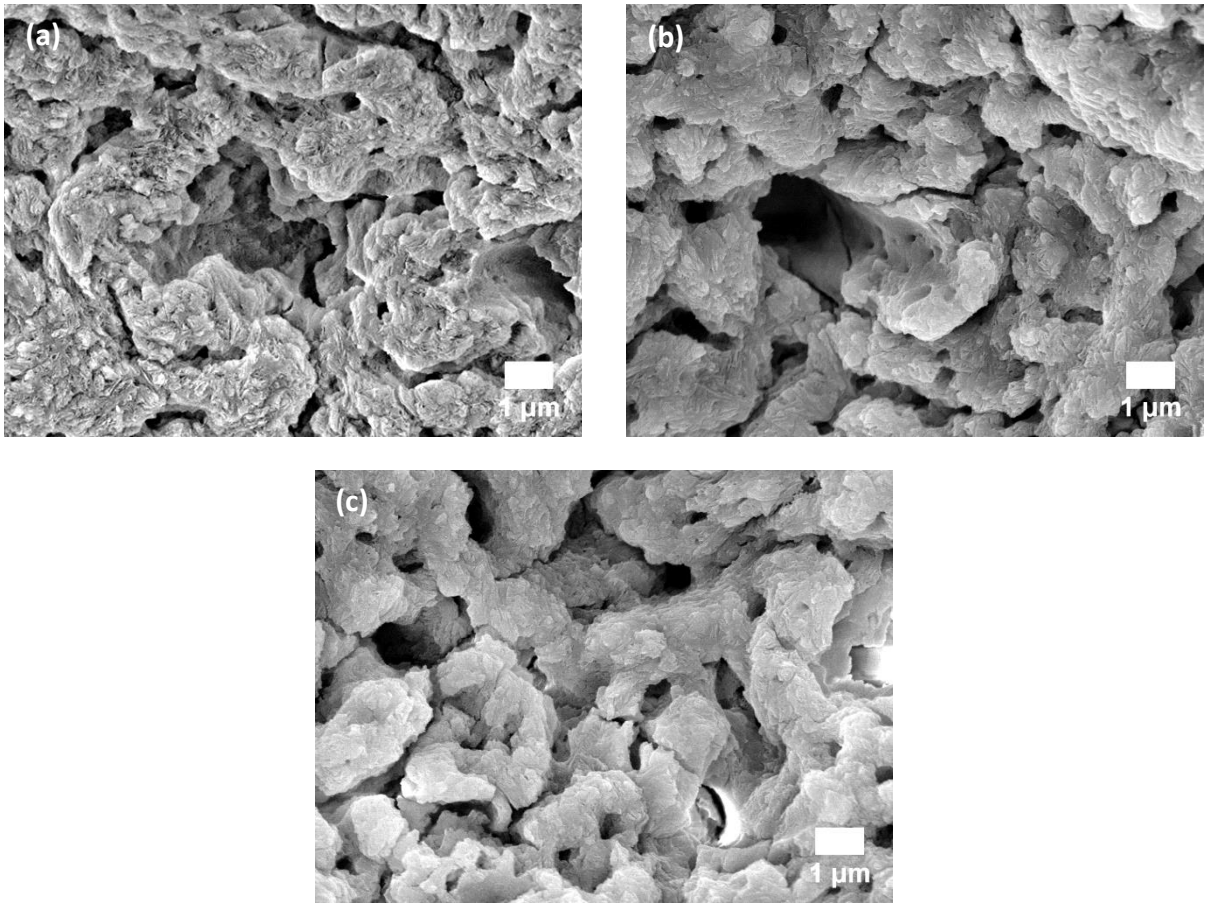

Figure 3.20: Morphology of craters created on dentin surface with fluence of 7 J/cm^2 and with 5 (a), 20 (b) and 40 (c) laser pulses.

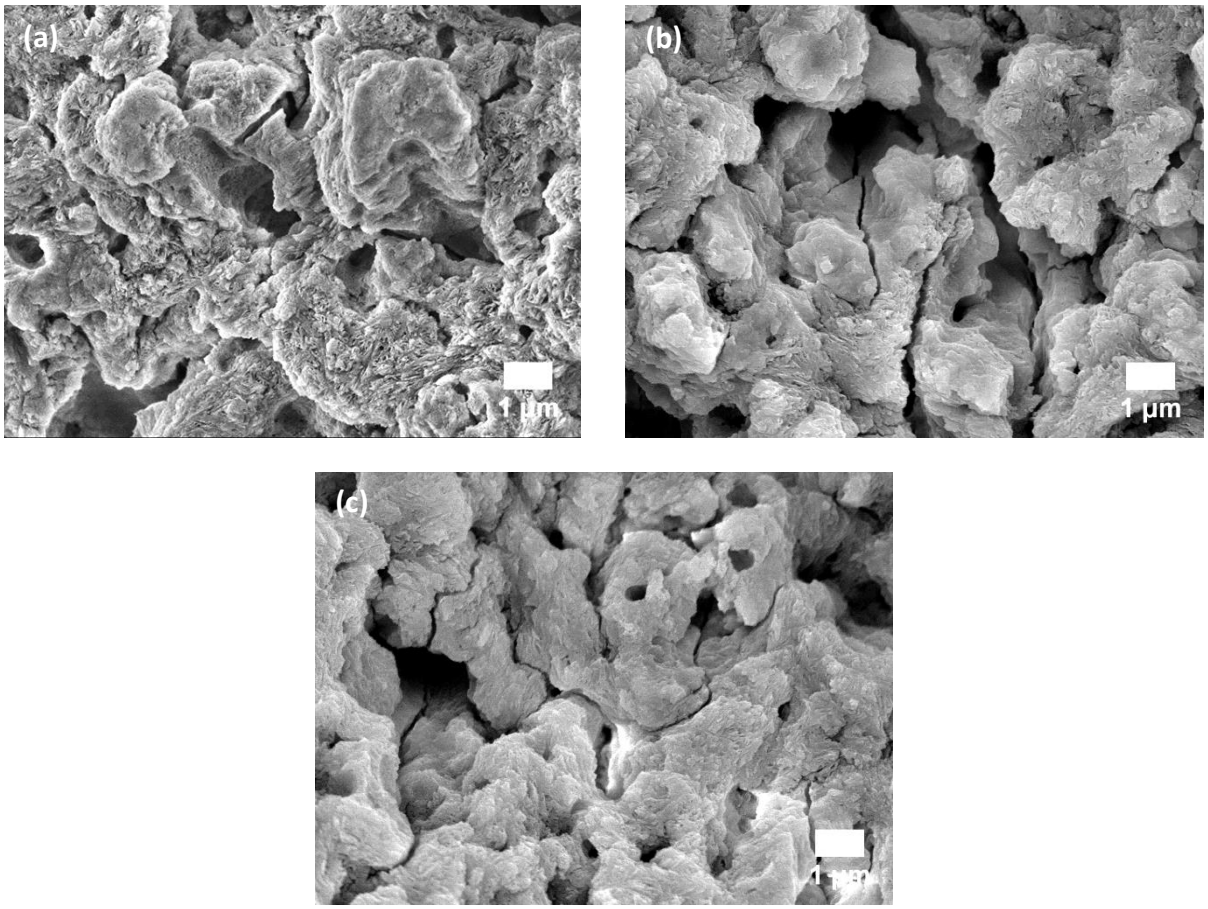

Figure 3.21: Morphology of craters created on dentin surface with fluence of 14 J/cm^2 and with 5 (a), 20 (b) and 40 (c) laser pulses.

3.2.1.c. Influence of collagen content in the ablation of dentin

The absence of resolidified material on the ablation surfaces of dentin, as opposed to that of enamel, suggests that their predominant ablation mechanisms are different. Such differences might be due to the presence of collagen molecules in dentin, which can be ablated at low fluences[102,141] by photochemical or photothermal mechanisms, leading to a reduction of dentin's cohesive strength and facilitating the tissue removal. The influence of collagen on the ablation of dentin was studied by performing laser experiments on a dentin specimen pre-treated with a 10 wt.% NaOCl solution for 1 hour to partially remove the collagen molecules in the surface region. Craters were created with average fluence of 2, 7 and 14 J/cm^2, 5 laser pulses and 1 Hz pulse repetition rate, parameters

that are similar to those applied to produce the craters presented in Figure 3.19 – 3.21. SEM observations were performed to study the surface morphology and to measure the craters.

The ablation threshold of the dentin specimens pretreated with NaOCl, determined by the D^2 method, was 1.25 ± 0.12 J/cm^2, a value similar to the ablation threshold of dentin (1.1 ± 0.3 J/cm^2, Figure 3.18a). On the other hand, the ablation surfaces (Figure 3.22) present traces of resolidified material and sub-micron collapsed bubbles, a morphology that resembles the morphology of the ablated enamel surface (Figure 3.4). The resolidified material was observed even in craters produced with a fluence as low as 2 J/cm^2, contrarily to what happens for pristine dentin. The presence of resolidified material in the specimens treated with NaOCl suggests that the role of thermal effects is more important when ablation occurs in specimens that contain less collagen molecules in the surface region.

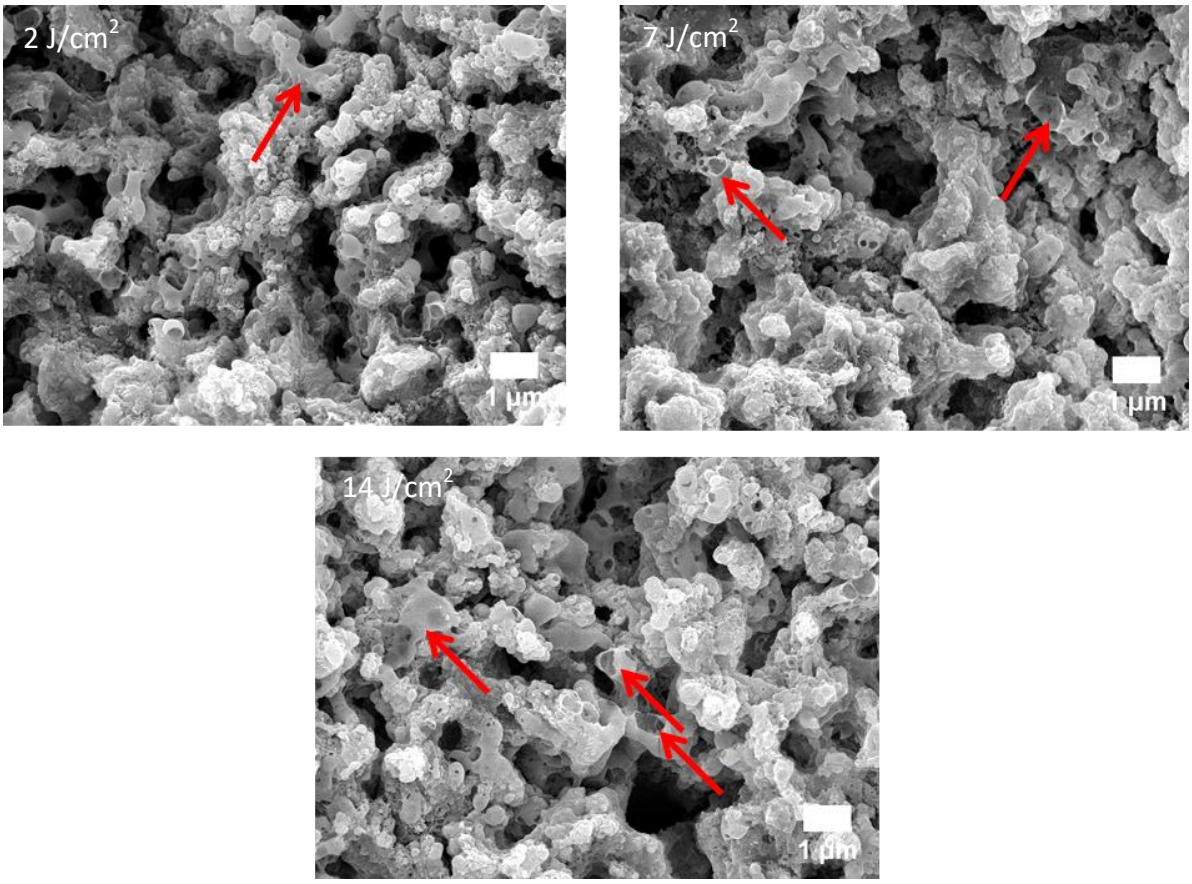

Figure 3.22: SEM images of craters created with 5 laser pulses and average fluence of 2, 7 and 14 J/cm² on a dentin disk pre-treated with NaOCl. Traces of resolidified material are indicated by red arrows.

3.2.2. Laser experiments in non-stationary conditions

Due to the relatively low ablation rate per pulse of dentin for femtosecond lasers, high pulse repetition rates and high radiation fluences are necessary for caries removal treatment in clinics. In this part of the study, the influence of high pulse repetition rates and radiation fluences on the morphology and chemical constitution of dentin was investigated. The laser treatment of dentin surfaces was performed by moving the specimens at a velocity of 5 mm/s while pulsing the laser beam at 1 kHz pulse repetition rate. Firstly, linear tracks were produced on the dentin surfaces with average fluences in the range 2 – 14 J/cm². The tracks were analyzed by a white light interferometer

(Section 2.2.2.d) to evaluate the ablation rate. The ablation rate per laser pulse was calculated by equation 2.11. Secondly, large areas were treated by overlapping the consecutive linear tracks created on dentin surface with similar scanning parameters and with a lateral displacement of 0.01 mm between the tracks. These treated specimens were used for the characterization of morphology and chemical constitution of laser treated dentin. The second set of experiments was performed with average fluences of 2, 7, and 14 J/cm^2.

3.2.2.a. Ablation rate

The evolution of the track width with the average fluence in the range 2 – 14 J/cm^2 is presented in Figure 3.23a by a semilogarithmic plot. The plot is in good agreement with the prediction of equation 2.2. The ablation depth increases linearly with increasing fluence (Figure 3.23b), contrarily to what was observed for enamel (Figure 3.8). This discrepancy was also reported by Ji et al.[18] for the ablation of dentin and enamel by a Ti:sapphire femtosecond laser (800 nm radiation wavelength, 85 fs pulse duration). The plot of the resulting ablation rate versus radiation fluence is presented in Figure 3.24. The ablated volume per laser pulse of dentin increases with fluence in the tested range and reaches the value of 44*10^2 µm^3/pulse with 14 J/cm^2.

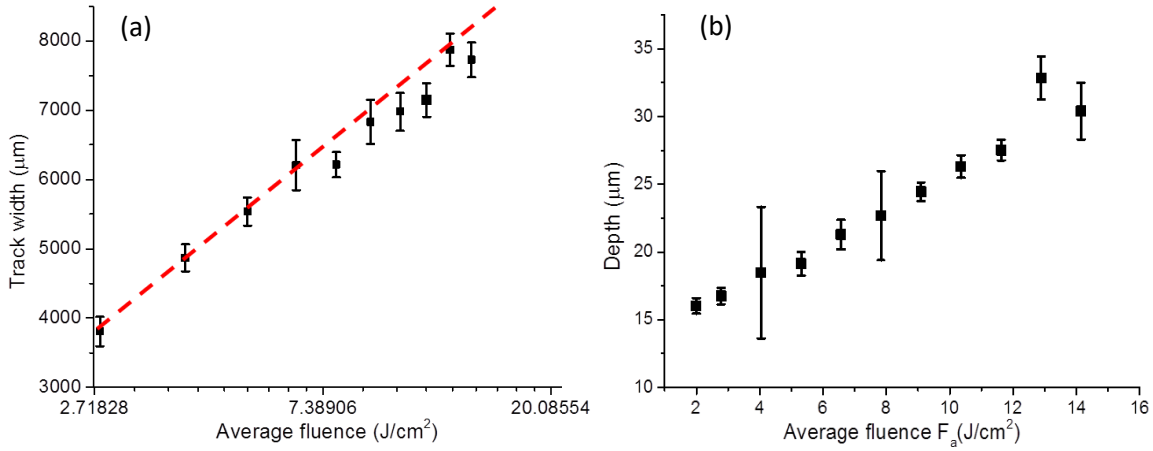

Figure 3.23: The evolution of width (a) and depth (b) of the linear tracks created on dentin surface with radiation fluence in the range 2 – 14 J/cm^2.

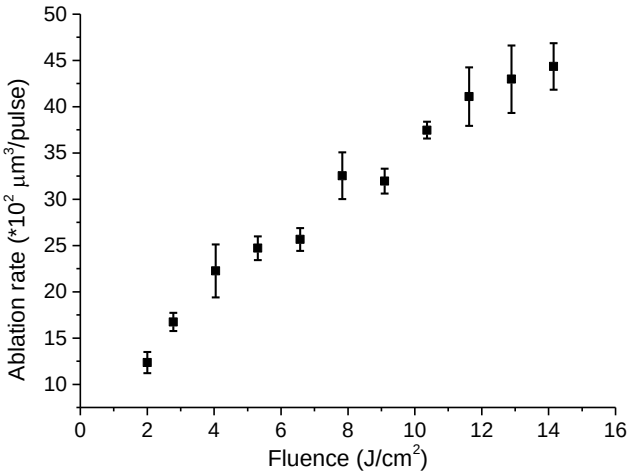

Figure 3.24: Evolution of the ablation rate of dentin with radiation fluence in the range 2 – 14 J/cm².

3.2.2.b. Surface morphology

The morphology of dentin surfaces treated with average fluences of 2, 7 and 14 J/cm² is depicted in the SEM micrographs of Figure 3.25. The surface treated with 2 J/cm² is flat and presents an irregular morphology with open tubules and a very small amount of redeposited ablation debris and spherical resolidified droplets (Figure 3.25a). The amount of ablation debris increases with fluence and the surfaces prepared with 7 and 14 J/cm² are covered by a layer of ablation debris and resolidified droplets aggregated in relatively large clusters (Figure 3.25c and 3.24e). The size of the clusters increases with fluence. The presence of resolidified droplets indicates a more important role of thermal effects in the ablation of dentin at 1 kHz pulse repetition rate as compared to 1 Hz pulse repetition rate (Figure 3.19 – 3.21), probably due to the increased accumulation of laser-induced heat in the ablation surface. Nevertheless, the layer of ablation debris is poorly adherent to the surface and can be removed by ultrasonication (Figure 3.25b, d and f). High magnification SEM images of these specimens are displayed in Figure 3.26. The dentinal structure is now clearly exposed and the tubules remain open. Afterwards, the laser treated specimens were immersed in liquid nitrogen and fractured with a sharp hammer blow on the backside. The cross-section of those

specimens was observed by SEM. The micrographs depicted in Figure 3.27 show that the laser treatments induce no significant damage in the remaining tissue.

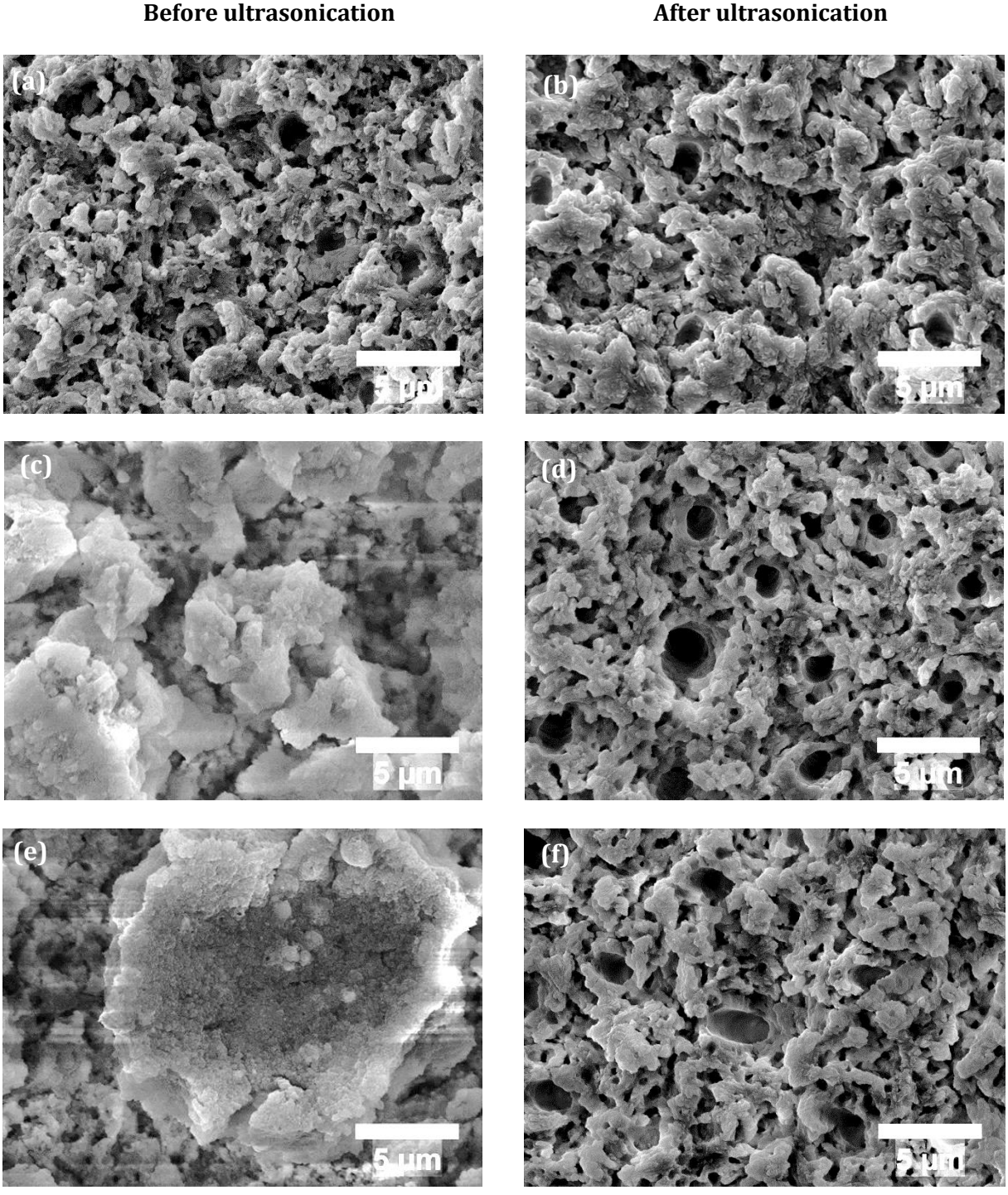

Figure 3.25: Morphology of laser treated dentin surfaces before and after ultrasonication. Fluences 2 J/cm^2 (a, b), 7 J/cm^2 (c, d), and 14 (e, f) J/cm^2. Pulse repetition rate 1 kHz.

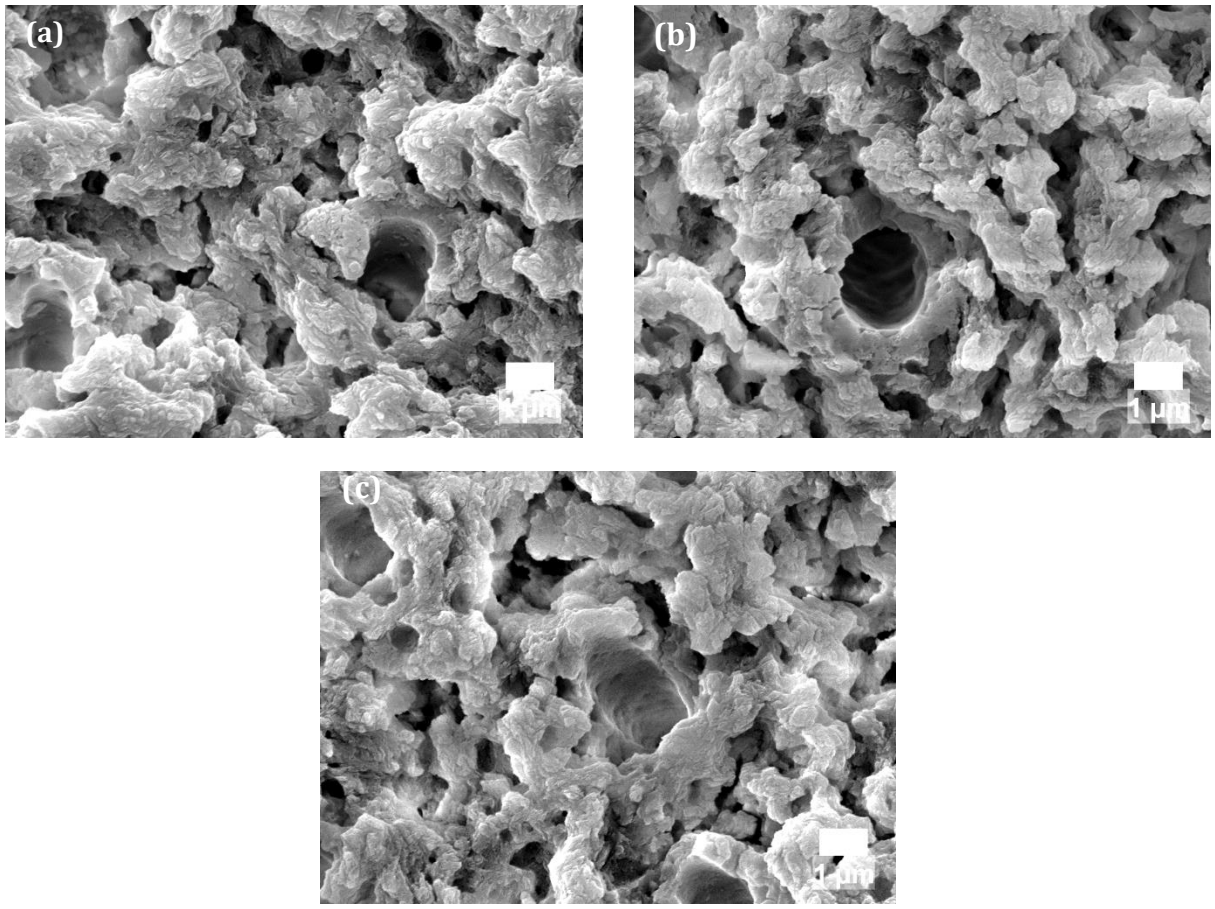

Figure 3.26: 10000X magnification SEM images of laser treated dentin surfaces after ultrasonication. Average fluences 2 J/cm^2 (a), 7 J/cm^2 (b) and 14 J/cm^2 (c). Pulse repetition rate 1 kHz.

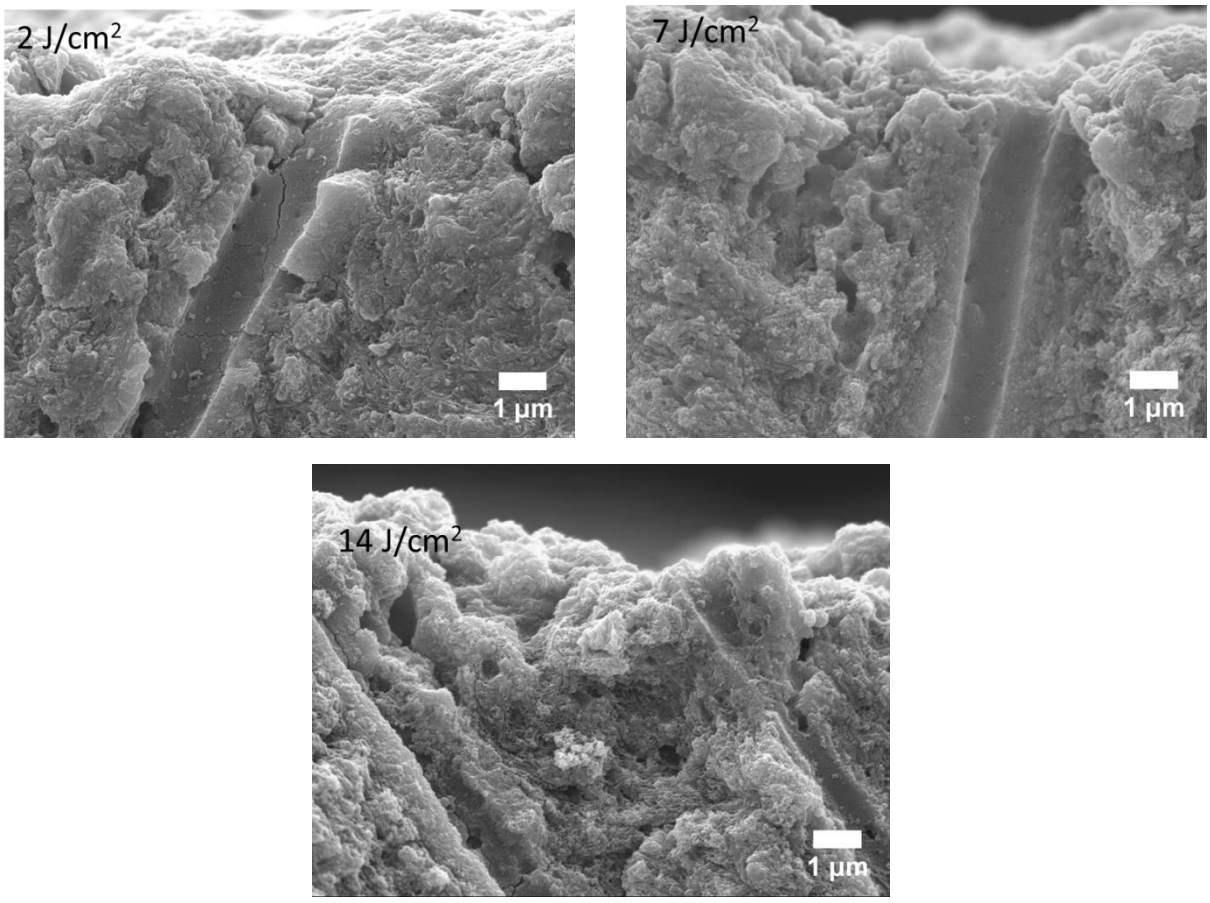

Figure 3.27: Cross sectional SEM images of dentin specimens treated with average fluences of 2 J/cm^2, 7 J/cm^2, 14 J/cm^2 and at 1 kHz pulse repetition rate.

3.2.2.c. Surface constitution

The constitution of laser treated dentin specimens was studied by FTIR spectroscopy, which presents lower depth of analysis and better sensitivity to collagen than microRaman spectroscopy (Section 2.3.3.b). The IR spectra of polished and laser treated dentin specimens are shown in Figure 3.28. They were normalized to the largest amplitude peak, at 1005 cm $^{-1}$, which corresponds to the ν_3 vibrational mode of the phosphate group of hydroxyapatite[14,142]. The peak at 960 cm^{-1} can be assigned to the ν_1 vibrational mode of the same anion, while the peak at 875 cm^{-1} corresponds to the ν_2 vibrational mode of the carbonate anions and the peaks at 1415 and 1430 cm^{-1} to the ν_3 vibrational mode of the same anions substituted in B-type PO_4^{3-} and A-type OH^- anionic sites,

respectively [14,142]. The bands between 1680 and 1600 cm^{-1}, and 1580 and 1510 cm^{-1} correspond to the vibrational modes of amide I (C=O stretching) and amide II (C-N stretching and N-H deformation modes) groups of collagen, respectively [14]. The assignments of dentin IR bands are summarized in Table 3.2.

Table 3.2: Band assignments for dentin IR spectra

Band position (cm^{-1})	Assignment
Phosphates [14,143]	
875	ν_2 mode of CO_3^{2-}
960	ν_1 mode of PO_4^{3-} (symmetric stretch)
1005	ν_3 mode of PO_4^{3-} in apatitic environment (asymmetric stretch)
1020	ν_3 mode of PO_4^{3-} in nonstoichiometric apatites containing HPO_4^{2-} and/or CO_3^{2-}
1030	ν_3 mode of PO_4^{3-} in stoichiometric apatites
1109	Found in poorly crystalline apatites
1123	Found in HPO_4^2 containing apatites
1415	ν_3 mode of CO_3^{2-} substituted in B-type PO_4^{3-} anionic sites
1430	ν_3 mode of CO_3^{2-} substituted in A-type OH^- anionic sites
Organics [143,144]	
1238, 1248	Amide III, β-sheet
1350	CH_2 wagging of the proline side chain
1400	ν COO^{2-}
1454	δ CH_3^-
1540	Amide II, α-helix
1634	Collagen random coil
1650	Amide I, α-helix

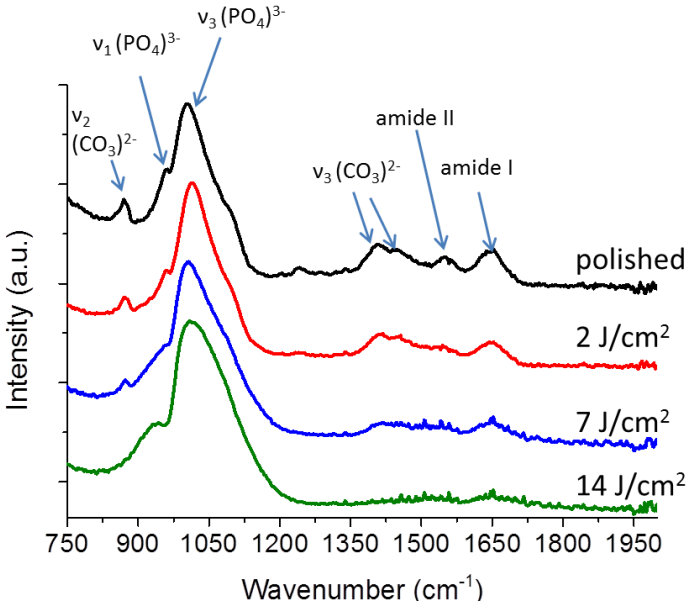

Figure 3.28: Infrared spectra of polished and dentin specimens treated at 1 kHz pulse repetition rate and fluences of 2, 7 and 14 J/cm².

The FTIR spectrum of the specimen treated with 2 J/cm² is similar to the spectrum of the polished specimen, showing that laser ablation with this low fluence does not change significantly the constitution of dentin. On the contrary, the spectra of the specimens treated with 7 and 14 J/cm² present some significant differences as compared to those of untreated dentin. On one hand, the amplitude of the peaks corresponding to the vibrational modes of CO_3^{2-} and to the amides decreases after a laser treatment with 7 J/cm² and these peaks disappear when the surface treatment is performed with 14 J/cm². On the other hand, the width of the phosphate band at 1005 cm⁻¹ increases and the narrow phosphate peak at 960 cm⁻¹, which appears in the spectra of the polished specimen and of the specimens treated with 2 and 7J/cm² is replaced by a broad peak at 950 cm⁻¹ in the spectrum of the specimen treated at 14 J/cm². Interestingly, the FTIR spectra of the specimens treated with 14 J/cm² are similar to the spectrum of amorphous calcium phosphate (ACP)[145,146] indicating that this compound is the main constituent of the dentin surface after laser treatment with this fluence. ACP peaks are also observed in the spectra of the specimens treated with 7 J/cm²,

but their amplitudes are lower, indicating that the proportion of this compound in the surface layer decreased.

After removing the ablation debris by ultrasonication, the spectra of the specimens treated with 7 and 14 J/cm^2 become similar to the spectrum of the polished specimen (Figure 3.29), indicating that the amorphous calcium phosphate exists mainly in the redeposited ablation debris and resolidified droplets (Figure 3.25) and that the tissue underneath was unaffected by the ablation process. It should be emphasized that the depth of sampling of the FTIR spectroscopy method used, estimated assuming that the refractive index of dentin is 1.54 [130] for the IR absorption spectral region of collagen (1650 cm^{-1}) is approximately 0.6 μm.

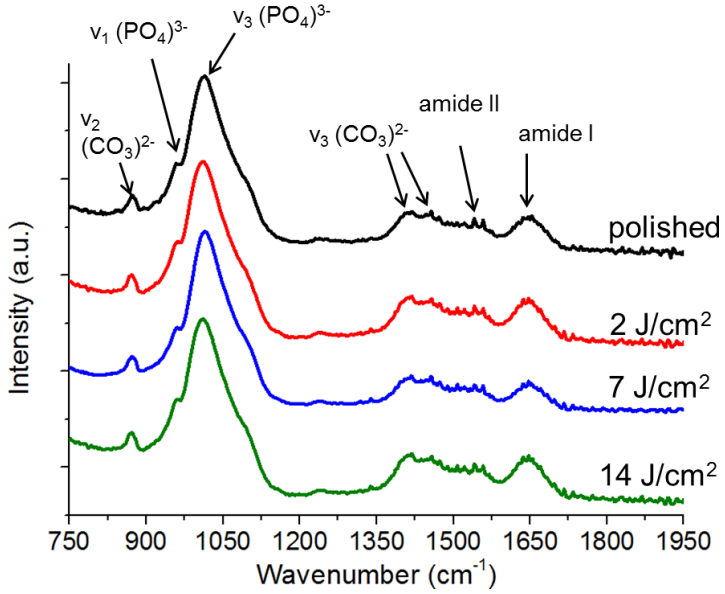

Figure 3.29: Infrared spectra of laser treated specimens after ultrasonication.

3.2.3. Heating of the teeth during laser treatments and influence of external cooling

Despite the lack of major thermal effects induced in dentin by femtosecond lasers, heat transfer to the tooth bulk cannot be avoided, in particular when performing prolonged treatments with high pulse repetition rates and high fluences, particular settings that are required to achieve high material removal rates[23,117]. In this section, heating of the teeth induced by the femtosecond laser

was studied by measuring temperature in the pulpal chamber during the laser treatments. The set-up for the temperature measurements was described in Section 2.2.2.c. Two healthy molars were used for this experiment. An area 3 x 3.5 mm^2 was treated on one of the teeth in non-stationary conditions with 5 mm/s scanning velocity, 1 kHz pulse repetition rate and radiation fluences of 2, 7 and 14 J/cm^2 to investigate the influence of fluence on the temperature rise. The duration of each laser treatment was 240s. A similar laser treatment was performed on the second tooth with an average fluence of 14 J/cm^2, without cooling and with external cooling by an air jet and water irrigation (Section 2.2.2.b). After each laser treatment the tooth was cooled to its initial temperature and rehydrated by irrigation with flowing water. The excess of water was removed with a clean absorbing paper tissue before the following laser treatment. The room temperature during these experiments was 23.5^oC. The area laser treatments with external cooling were also performed on polished dentin disks to investigate the morphology and chemical constitution of dentin surfaces treated in these conditions by SEM and FTIR spectroscopy, respectively.

3.2.3.a. Temperature measurement

The variation of the pulpal chamber temperature during a laser treatment without external cooling, an average fluence of 7 J/cm^2 and a pulse repetition rate of 1 kHz is depicted in Figure 3.30a. Despite the short pulse duration and the moderate pulse repetition rate, heat accumulates in the tooth leading to a rapid increase of the temperature, which reaches 34.5°C after 65 s, then remains approximately constant during the full duration up to the end of the laser treatment (175 s more). The temperature decreases after stopping the laser irradiation, but the cooling rate is quite low due to the low thermal diffusivity of dentin[35]. The behavior is similar for the other fluences tested. The temperature variation increases with fluence from approximately 3.1°C for 2 J/cm^2 to 17.5°C for 14 J/cm^2 and for 240s laser treatments (Figure 3.30b).

The maximum temperature reached during laser treatments performed with 14 J/cm², without and with forced cooling are summarized in Table 3.3. The maximum temperature observed without external cooling in this set of experiments was 39.3 ± 0.5°C. Cooling with an air jet leads to a decrease of the maximum temperature to 34.3 ± 1.0°C, while for water irrigation the maximum temperature is 30.1 ± 2.3°C.

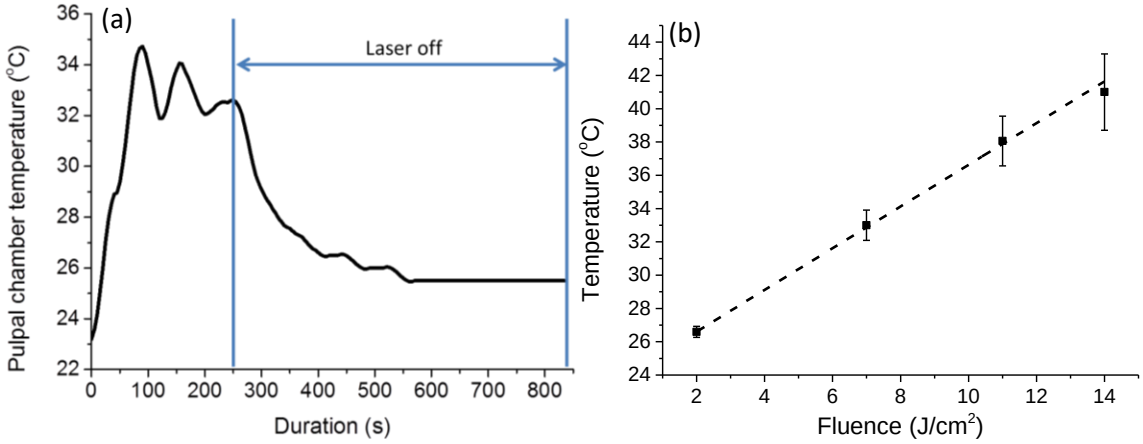

Figure 3.30: (a) Variation of the pulpal temperature during laser treatment performed in air with 7 J/cm² and (b) Variation of the maximum pulpal temperature with fluence.

Table 3.3: Influence of external cooling on the maximum pulpal temperature reached during laser treatment with 14 J/cm²

Cooling mode	**Average temperature (°C)**
No cooling	39.3 ± 0.5
Air jet	34.3 ± 1.0
Air jet + water irrigation	30.1 ± 2.3

3.2.3.b. Surface morphology

The surface morphology of dentin specimens treated with external cooling is depicted in the SEM micrographs of Figure 3.31. The surface prepared with air cooling and fluence of 2 J/cm² is partially covered by a layer of redeposited ablation debris and a few resolidified droplets, which obstruct the

structure of the underlying tissue (Figure 3.31a). The amount of redeposited material increases with fluence and the ablation debris form a continuous layer for surfaces treated with 7 and 14 J/cm^2 (Figure 3.31c and e). This layer can be observed in cross-section depicted in Figure 3.32. Its thickness increases with fluence (approximately 2 and 4 μm for 7 and 14 J/cm^2, respectively). However the structure of the dentin below this layer was not affected by the ablation process within this fluence range. As compared to the ablation surfaces produced without cooling (Figure 3.25), those treated with air cooling present significantly higher amount of resolidified droplets in the redeposited material. This result might be explained by the dehydration of dentin by the air stream, leading to reduced heat capacity of the tissue[147], and, hence, more important role of thermal effects in the ablation process. On the contrary, water – cooled specimens present rougher surfaces and the amount of redeposited debris is smaller than with air jet cooling. The layer of redeposited material is discontinuous for 2 and 7 J/cm^2, leaving the dentinal tubules exposed (Figure 3.31b and d). For 14 J/cm^2 the ablation debris layer is continuous and it obstructs the dentinal structure (Figure 3.31f). Regardless of the external cooling method used, the ablation debris can be easily removed by ultrasonication, revealing that the structure of the underlying dentin was not affected by the laser treatment (Figure 3.33).

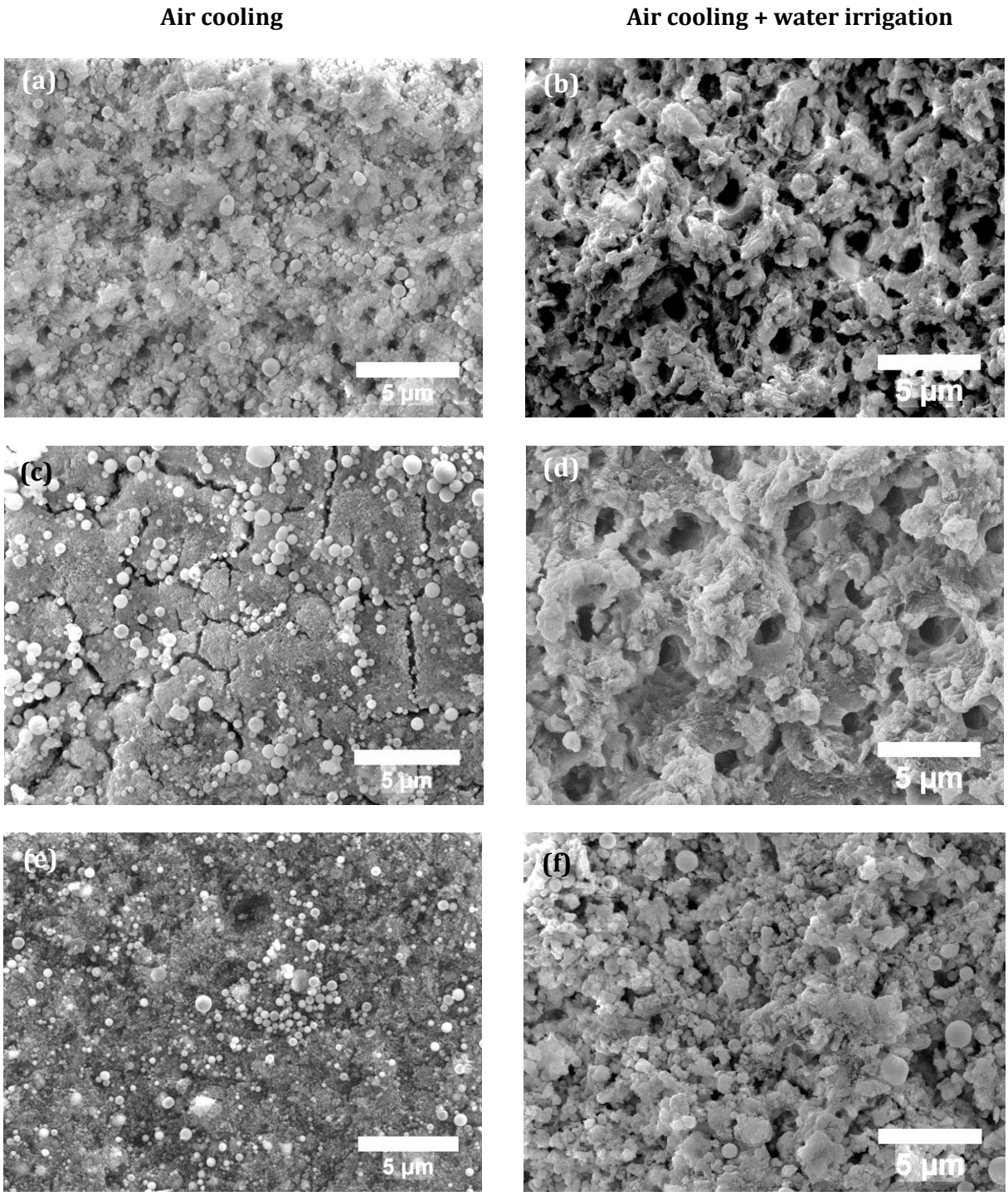

Figure 3.31: Morphology of dentin surfaces treated with air and water cooling. Fluences 2 J/cm^2 (a, b), 7 J/cm^2 (c, d), and 14 (e, f) J/cm^2.

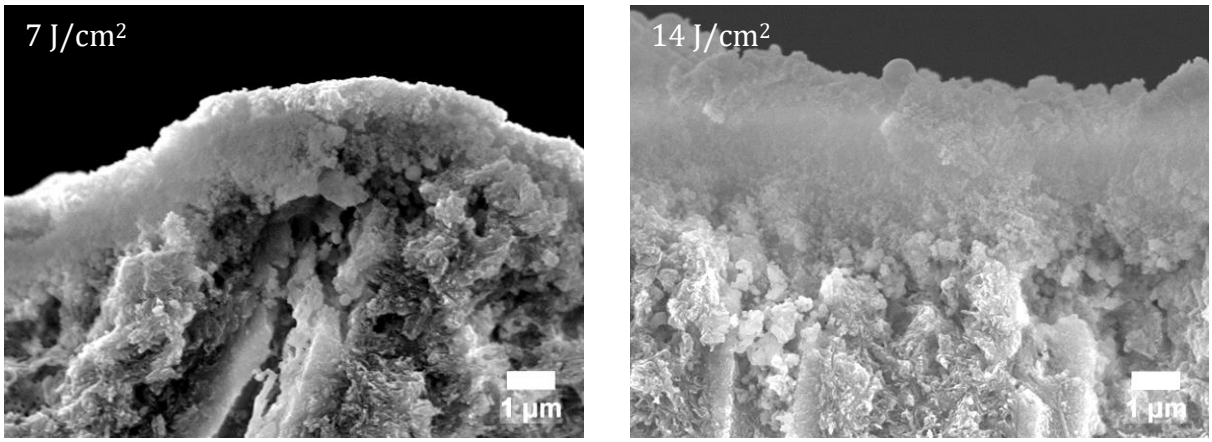

Figure 3.32: Cross sectional SEM images of specimens treated with air jet.

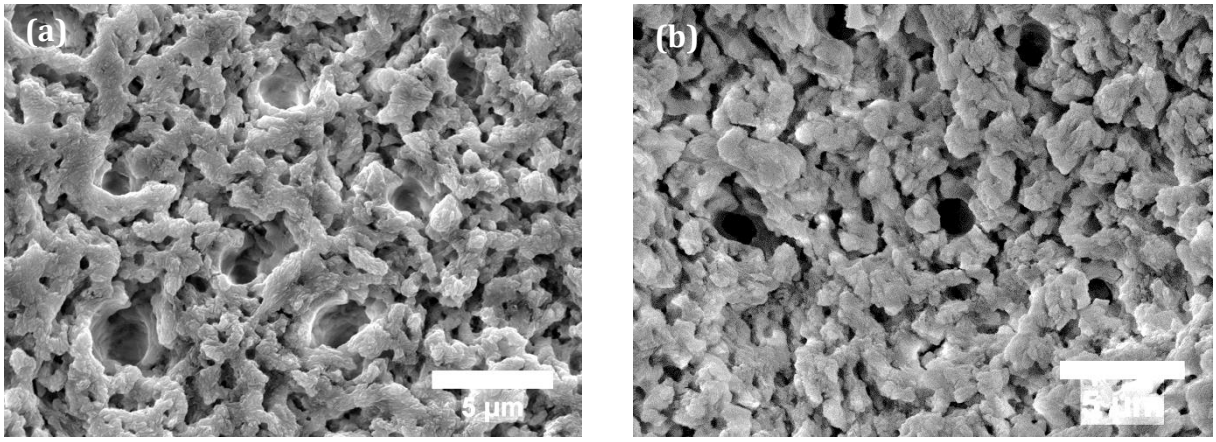

Figure 3.33: Morphology of dentin surfaces treated with 14 J/cm^2 after removal of the debris layer by ultrasonication: (a) air cooling and (b) water cooling.

3.2.3.c. Surface constitution

The IR spectra of the laser treated specimens are shown in Figure 3.34 together with the spectrum of a polished sample, used as a reference. All the spectra were normalized to the largest amplitude peak, centered at 1005 cm $^{-1}$, which corresponds to ν_3 vibrational mode of the phosphate group of hydroxyapatite. The spectrum of the specimen treated with 2 J/cm^2 and cooled with air is similar to the spectrum of the polished specimen, but differences are observed after laser treatments with 7 and 14 J/cm^2 indicating that the surface constitution of dentin is modified after a laser treatment in this fluence range. The most important differences are as follows:

(a) the peaks corresponding to the CO_3^{2-} and to the amides group vanish;

(b) the width of the phosphate band at 1005 cm^{-1} increases and the narrow phosphate peak, which appears at 960 cm^{-1} in the spectra of the polished specimen and after laser treatment with 2 J/cm^2 is replaced by a broad band centered at 950 cm^{-1}.

When the water irrigation is used alterations are only observed for the specimen treated with 14 J/cm^2 and they are less conspicuous, showing that water cooling minimizes changes to the specimen surface constitution. Regardless of the cooling method and the fluence used, the spectra of the laser treated specimens after ultrasonication are similar to the reference spectrum, indicating that the alterations of constitution observed by the FTIR is only due to the redeposited ablation debris, the constitution of the underlying tissue remaining unaltered (Figure 3.35).

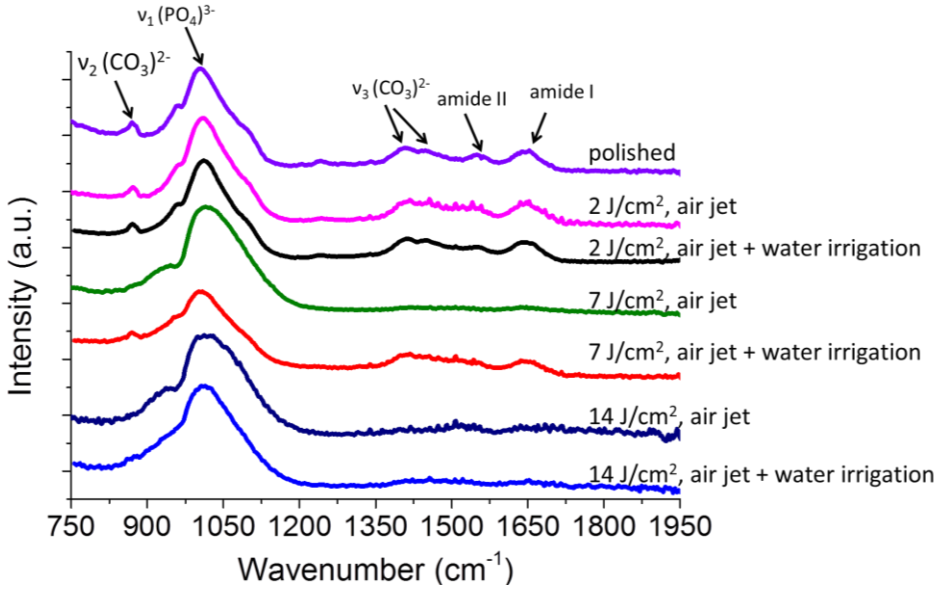

Figure 3.34: Infrared spectra of polished and laser treated dentin specimens.

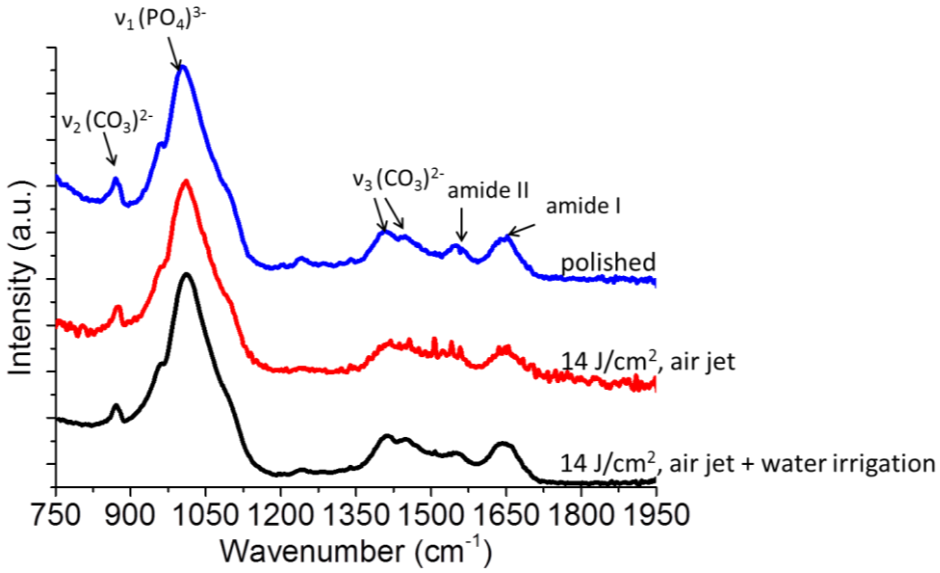

Figure 3.35: Infrared spectra of polished specimen and

laser treated specimens after ultrasonication.

3.2.3.d. Influence of external cooling in the ablation rate of dentin

The ablation rate of dentin with external cooling was determined by measuring the depth of the laser treated areas on dentin surface by optical microscopy using a 100X objective (NA 0.9). The measurement was also performed on dentin disks treated without external cooling for comparison. The laser treated specimens were ultrasonicated before the optical microscope observation. The microscope was focused at the bottom of the treated area and at the surrounding polished surface consecutively, the ablation depth being calculated as the difference of the two vertical coordinates. Since the depth of focus of the microscope, which is 1 and 1.2 μm at 532 and 633 nm radiation wavelengths, respectively, is much lower than the surface roughness at the bottom of the craters, the measurement error was estimated by the standard deviation of the measured values. The ablation volume was then determined from the measured depth, length and width of the treated surface. The ablation rate per pulse was calculated by dividing the ablation volume by the number of laser pulses required. The variation of the ablation rate with average fluences in the range 2 – 14

J/cm² for different cooling methods is plotted in the graph of Figure 3.36. The result shows an increase of ablation rate with radiation fluence, regardless of the cooling method used. In addition, external cooling has a negligible influence on the ablation rate for fluences in the tested fluence range.

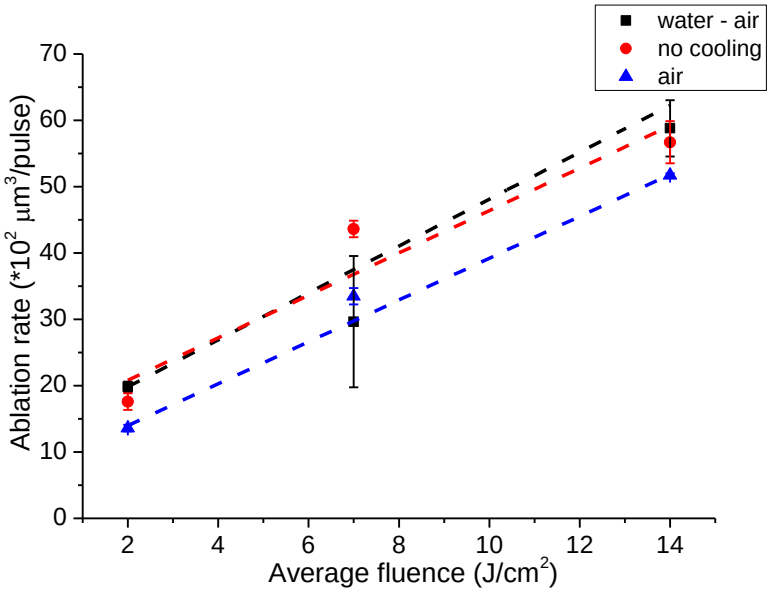

Figure 3.36: Variation of the ablation rate with fluences for different cooling methods.

3.3. Adhesion of Adhese Universal self-etch adhesive to laser treated dentin surfaces

This part of the study aimed at evaluating the bond strength of dental restorative adhesives to dentin surfaces prepared by femtosecond laser treatment and comparing it with the bond strength to surfaces prepared with a tungsten carbide burr. The method used for the preparation of dentin surfaces with the burr was described in Section 2.4.1. The morphology of dentin surfaces prepared by drilling was investigated by SEM while the etching behavior of dentin surfaces prepared with the burr and by laser treatment was studied by SEM and FTIR spectroscopy. Etching was performed with a silica-thickened gel (Scotchbond Universal Etchant®, 3M Deutschland GmbH, Germany), which contains 32 wt.% H_3PO_4 and present a pH of 0.1. The bond strength of the self-etch adhesive

(Adhese Universal ®, Ivoclar Vivadent ©, Lithuania) to the dentin surfaces was evaluated by shear tests. The failure mechanisms were investigated by observing the fracture surfaces by SEM. The adhesive system and the setup used for the shear tests were described in detail in Section 2.4.1.

3.3.1. Dentin surfaces prepared by tungsten carbide burr

The morphology of dentin surfaces prepared with a 1 mm diameter tungsten carbide burr is presented in Figure 3.37. The surface is covered by a smear layer consisting of debris produced by the abrasion of dentin by the burr, which obstructs the dentinal tubules. Cracks are observed on the surface, but they are limited to the smear layer, as shown in the SEM micrograph of the specimen cross section (Figure 3.37c). No mechanical damage occurs in the underlying dentin. The observed smear layer has a thickness in the range 1 – 2 μm.

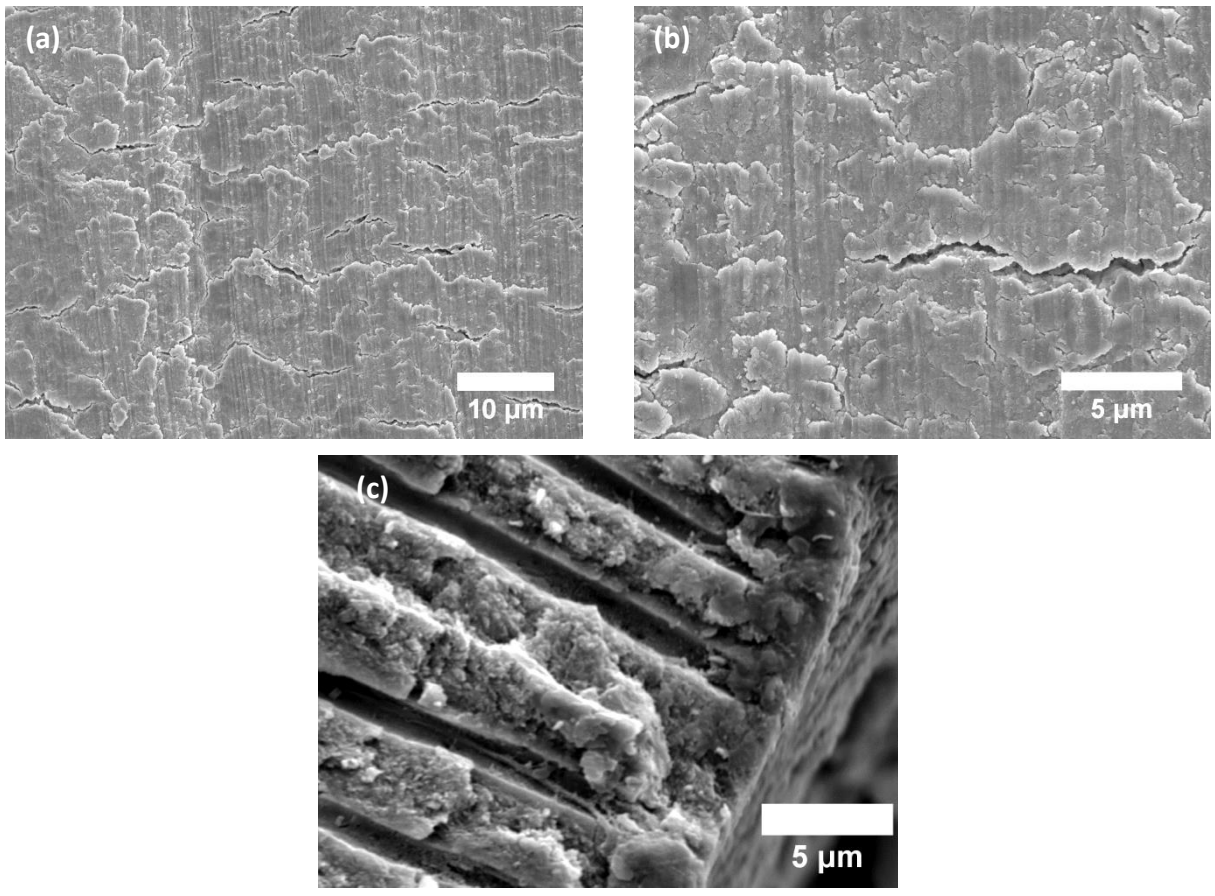

Figure 3.37: SEM micrographs of dentin surface prepared by tungsten carbide burr. (a), (b) top-view and (c) cross-section.

3.3.2. Etching behavior of treated dentin surfaces

The etching behavior was studied on surfaces prepared by laser treatment, with fluences of 2 and 14 J/cm^2 at 1 kHz pulse repetition rate, and by drilling with a tungsten carbide burr. These surface treatments were performed on polished dentin disks. The treated surfaces were etched by direct contact with the etching gel during 15 s, according to the supplier's instruction, followed by rinsing with a copious water flow. SEM micrographs of the dentin surfaces after etching are presented in Figure 3.38. The etchant dissolves completely the smear layer and hydroxyapatite in a layer of dentin underneath it (Figure 3.38a and b). The dissolution of hydroxyapatite leads to the disappearance of the peritubular dentin surrounding the dentinal tubules and to the exposure of the collagen fibers of the intertubular dentin. These fibers collapsed in the SEM micrographs of Figure 3.38 due to the dehydration in the vacuum environment in the SEM. When the specimens are kept in water, they form a continuous layer of collagen fibrils[70]. When etching is performed after the laser treatment the etched surfaces present an irregular morphology with numerous sub-micron sized voids, regardless of the laser fluence used. The presence of these voids in the exposed collagen layer shows that the sub-superficial collagen molecules in those specimens were partially removed by the laser treatments. Collagen may have been removed by photothermal or photochemical laser ablation mechanisms[11,109], or simply denatured due to the temperature increase in the surface layer of dentin during the laser treatment[74]. Regardless of the surface treatment, clusters of silica particles are observed on the etched surfaces. These particles are a constituent of the etching gel, used to increase its viscosity[148] and have a negligible influence on the bond strength of restorative adhesives to dental hard tissues surface[148].

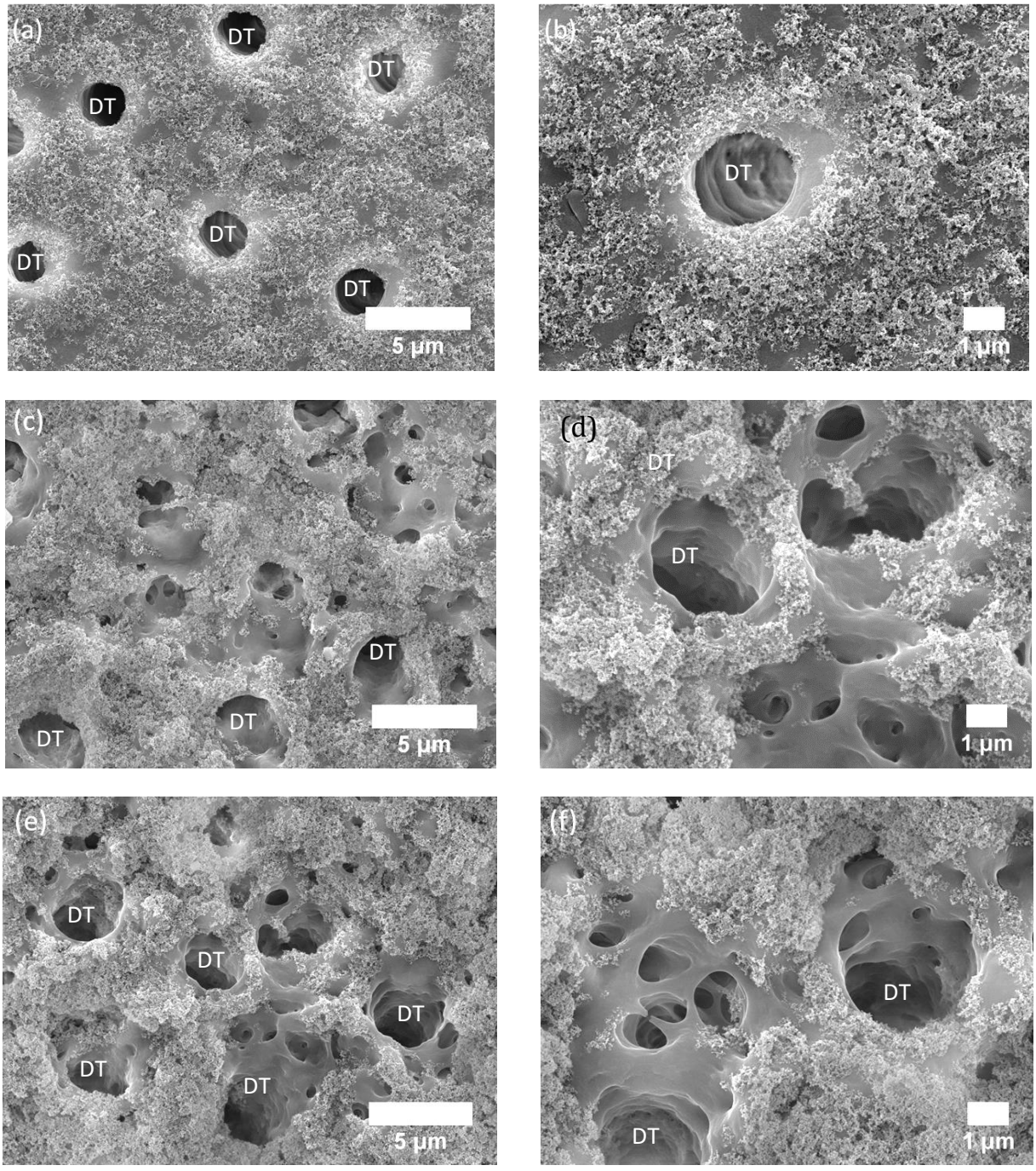

Figure 3.38: Morphology of dentin surfaces prepared by tungsten carbide burr (a, b) and laser treatments with 2 J/cm^2 (c, d), and 14 J/cm^2 (e, f) after acid etching. Legend: DT – dentinal tubules.

The thickness of the demineralized layer was investigated by SEM observation at the cross section of etched specimens. The dentin specimens were immersed in liquid nitrogen and fractured with a

sharp hammer blow on the backside. The SEM micrographs of the fractured surfaces are depicted in Figure 3.39. They show that the demineralization affected a surface layer 1 – 2 μm thick. The thickness of this layer does not depend on the specimen preparation method. Since the specimens were dehydrated by exposure to vacuum during the SEM observation, the collagen fibers in the demineralized layer collapsed, so the thickness of this layer as observed in the SEM micrographs is lower than the thickness of the demineralized dentin available for infiltration by the adhesive resin to form the hybrid layer.

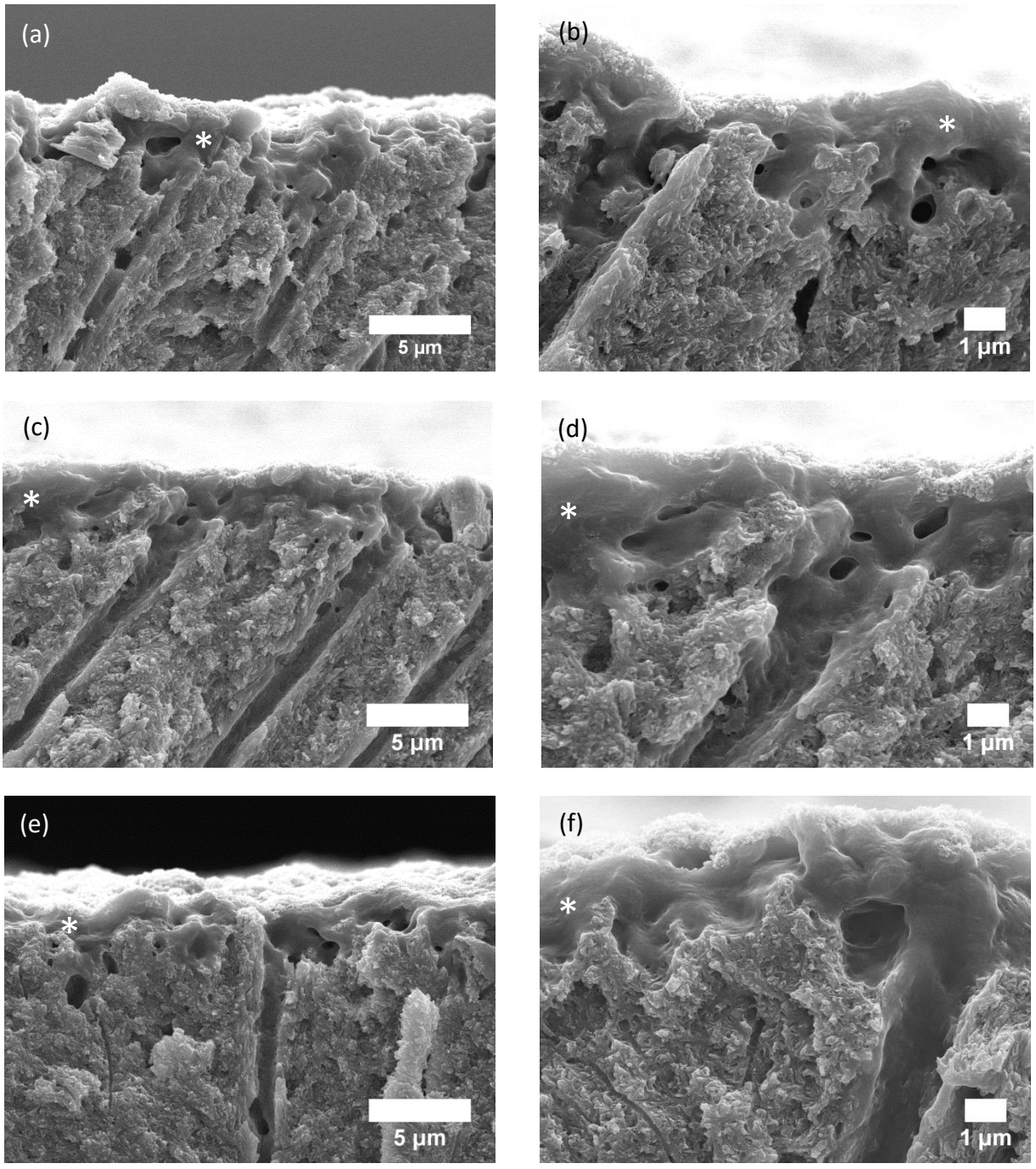

Figure 3.39: SEM micrographs of the cross sections of dentin surfaces prepared by tungsten carbide burr (a, b) and laser treatment with 2 J/cm^2 (c, d) and 14 J/cm^2 (e, f) after acid etching. The demineralized layer is indicated by asterisks (*).

The chemical constitution of the demineralized dentin was analyzed by FTIR spectroscopy. The spectra obtained are presented in Figure 3.40. The assignment of the IR bands is indicated in Table 3.2. The spectra were normalized to the highest amplitude peak at ca. 1640 cm^{-1}. This peak corresponds to the amide I group of collagen. Compared to the IR spectrum of polished dentin (Figure 3.28), the spectra of etched dentin present a significantly lower spectral intensity in the range 800 – 1200 cm^{-1}. The peaks at 850, 960 and 1005 cm^{-1} are not observed in the spectra of surfaces prepared by laser treatment with 2 J/cm^{-1} and by drilling with the tungsten carbide burr, indicating that dentin hydroxyapatite was completely removed by the acid etchant. On the contrary, those peaks are still discernible in the spectrum of specimen treated with 14 J/cm^2, indicating that the thickness of the demineralized layer is lower in this specimen than in other specimens. In addition, a shift of the peak corresponding to ν_1 vibrational mode of PO_4^{3-} anions from 1005 cm^{-1} to ca. 1020 cm^{-1} can be clearly observed in the specimen treated with 14 J/cm^2 after etching. This difference can be explained by the replacement of the phosphate anions by HPO_4^{2-} due to the exposure to the acidic environment[149,150]. The intensity of this peak in the spectrum of the specimen treated with 14 J/cm^2 is lower than its intensity in the spectra of the other etched specimens. The observation confirms that the demineralized layer in the specimen treated with 14 J/cm^2 has lower thickness than in the other etched specimens. The difference might be explained by the removal of the sub-surface collagen molecules by thermal denaturation ($T_{denaturation} \sim 160^oC$[151]) due to the increase of dentin temperature during the surface treatment, which is probably more significant with 14 J/cm^2 than with 2 J/cm^2 and with the burr. The substantial heat accumulation induced in dentin during the laser treatment with 14 J/cm^2 can also cause the release of CO_2 from the carbonated hydroxyapatite present in dentin, which often occurs in the temperature range ($T = 100 – 650^oC$[66,134,152,153]). This decomposition of carbonated hydroxyapatite enhances the acid resistance of the mineral phase in dentin[66,152]. Consequently, the demineralization of the surface treated with 14 J/cm^2 occurred at a lower rate than the surfaces treated with 2 J/cm^2 and with the burr. The low

dissolution rate of the specimen treated with 14 J/cm^2 also contributes to the low thickness of the exposed collagen layer in this specimen after etching.

The intensity of the peak observed at ca. 1080 cm^{-1} in the IR spectra of the etched specimens is not significantly influenced by the surface treatment. This peak can be assigned to either the ν_3 vibration mode of PO_4^{3-} [143] or to the Si – O – Si ν_1 stretching mode of silica[154]. The latter assignment is more likely, due to the presence of silica particles on the etched dentin surfaces (Figure 3.38 and Figure 3.39), and because the other prominent peaks of PO_4^{3-} anions are not observed. The bands observed in the range 1200 – 1800 cm^{-1} of the spectra presented in Figure 3.40 are similar to those observed in the spectra of pristine collagen[155], showing that the molecular structure of the collagen present near the surface was not significantly modified by the surface treatment method performed.

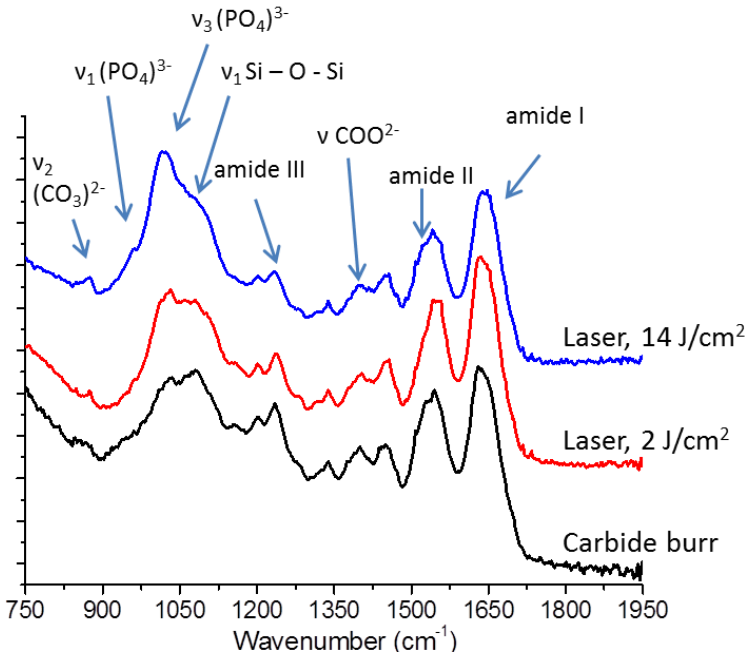

Figure 3.40: Infrared spectroscopy of treated specimens after acid etching.

3.3.3. Analysis of the adhesive – dentin interface

The adhesive – dentin interfaces in the specimens prepared by laser treatment or drilling with the tungsten carbide burr were observed by scanning electron microscopy. The bonding procedures

and preparation of specimens for SEM analysis were described in detail in Chapter 2. The SEM micrographs for specimens bonded with etching (total-etch mode) and without etching (self-etch mode) are depicted in Figure 3.41 and Figure 3.42, respectively. In the specimens bonded in the total-etch mode the adhesive resin infiltrates the dentinal tubules, leading to the formation of resin tags, regardless of the surface treatment (Figure 3.41). A layer of material that shows signs of degradation under prolonged electron beam irradiation is observed at the adhesive – dentin interface in those specimens (indicated by the red lines). According to Van Meerbeek et al.[156,157] and Armstrong et al.[158] this layer is formed by the infiltration of the adhesive resin in the partially demineralized dentin layer at the surface and it is called hybrid layer. The thickness of the hybrid layer is lower in the specimen treated with 14 J/cm^2 (~ 1 – 2 μm) as compared to the specimens treated with 2 J/cm^2 and tungsten carbide burr (~ 2 – 3 μm), but the difference is not significant, due to the large variations of the thickness of this layer.

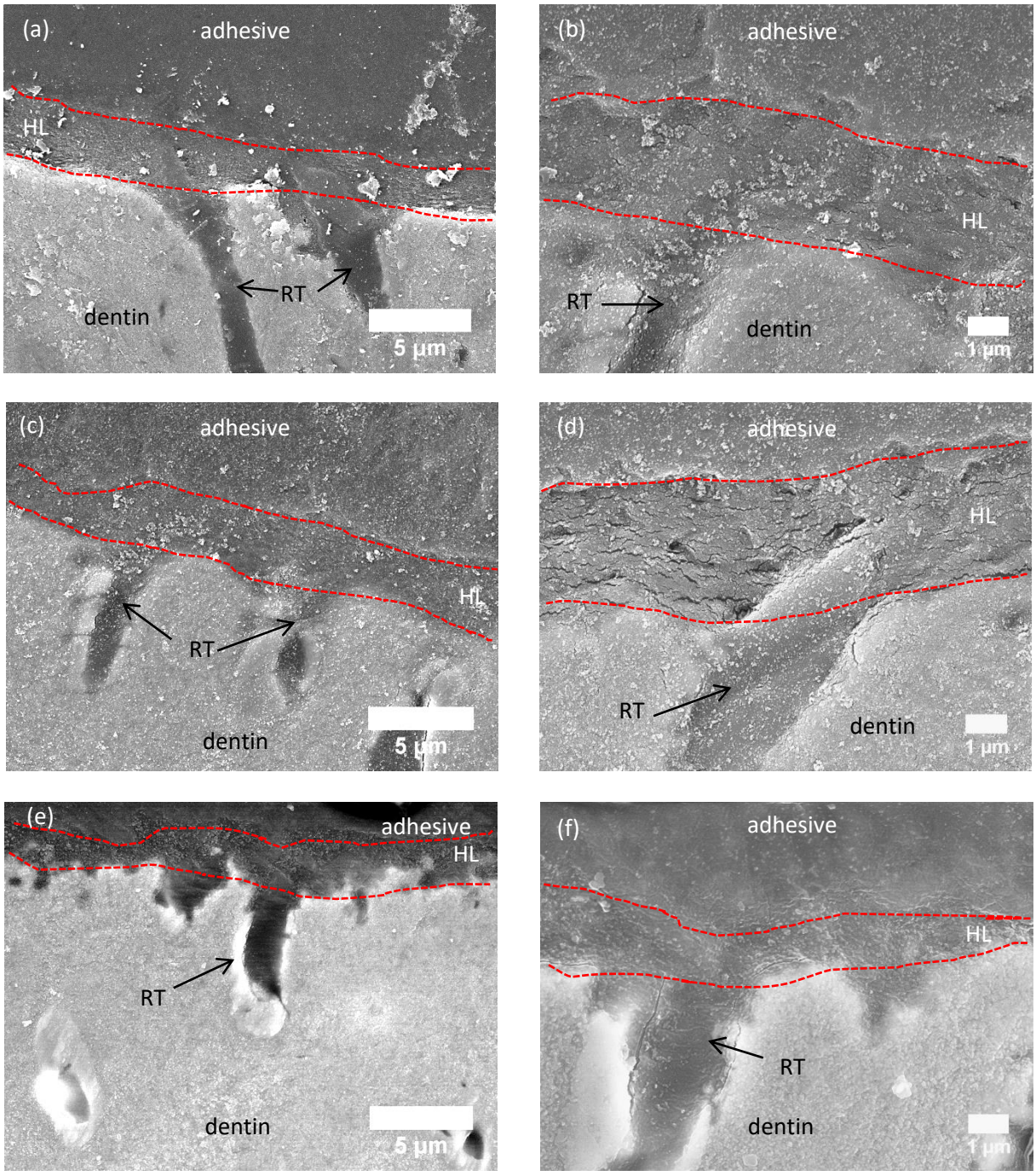

Figure 3.41: SEM micrographs of the adhesive - dentin interface in specimens bonded in total-etch mode. Surface preparation was performed by tungsten carbide burr (a and b) and laser treatment with 2 J/cm^2 (c and d) and 14 J/cm^2 (d and f). Legend: HL – hybrid layer, RT – resin tag.

Resin tags are also detected in the specimens prepared by laser treatment and bonded in self-etch mode, but no well-defined hybrid layer is observed in this case (Figure 3.42). The adhesive – dentin interface in the specimen treated with 14 J/cm^2 presents a layer in which hydroxyapatite was partially dissolved and infiltrated by the adhesive resin (Figure 3.42e and f). The elemental composition of the interfacial material layer was investigated by EDX mapping (Section 2.3.1). The distributions of Ca, P and O (the main constituents of hydroxyapatite), and of C (the main constituent of the adhesive resin) are presented in Figure 3.43. The layer of material at the interface consists mainly of calcium phosphate. The particles of calcium phosphate observed in the SEM micrographs of (Figure 3.42e and f) present a rounded elongated shape, indicating that they do not originate from the redeposited resolidified droplets formed by the laser ablation, which are spherical in shape. The temperature increase caused by the laser treatment with 14 J/cm^2 may be sufficient to cause chemical modifications in dentin such as the decomposition of carbonated hydroxyapatite and its partial melting. These modifications of hydroxyapatite can enhance the resistance of the calcium phosphate against acid etching[152], forming a layer of calcium phosphate particles that are not completely dissolved by the adhesive, as observed in Figure 3.42e and f. On the contrary, the specimens prepared with the mechanical burr and bonded in self-etch mode present hollow dentinal tubules (Figure 3.42a and b), indicating that the adhesive resin failed to infiltrate the dentinal structure underneath the smear layer. No hybrid layer is observed in the micrographs of these specimens.

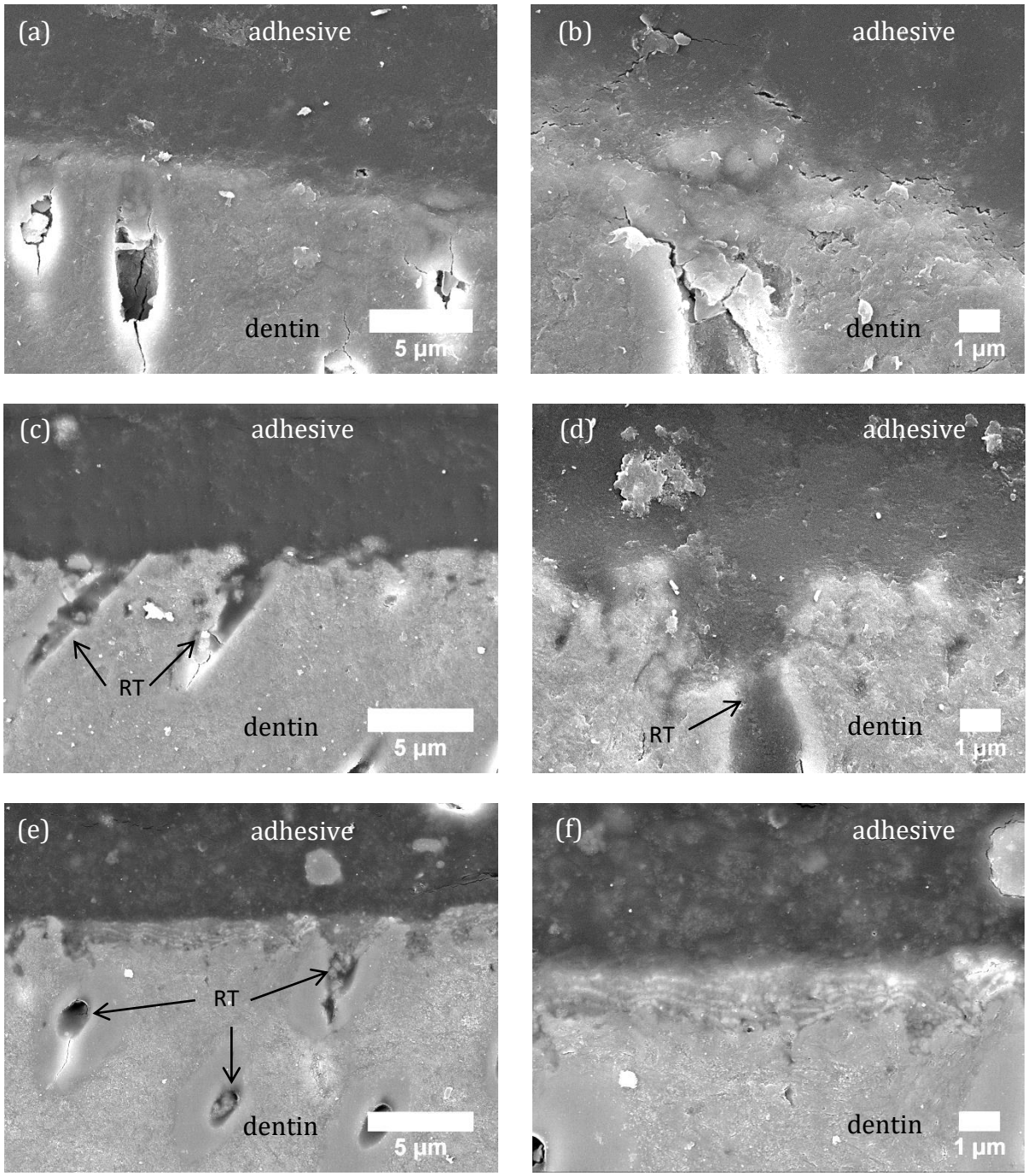

Figure 3.42: SEM micrographs of the adhesive - dentin interface in specimens prepared by (a, b) tungsten carbide burr and laser treatment with 2 J/cm^2 (c, d) and 14 J/cm^2 (e, f) and bonded in self-etch mode. Legend: RT – resin tags.

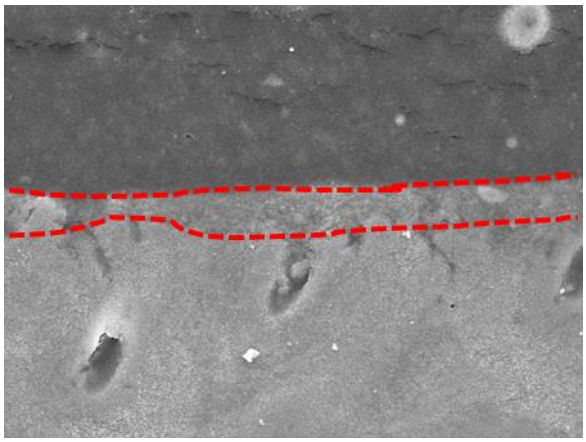

(a) SEM micrograph

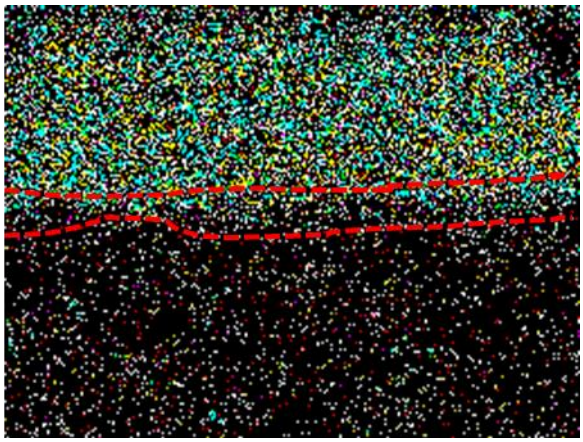

(b) C distribution

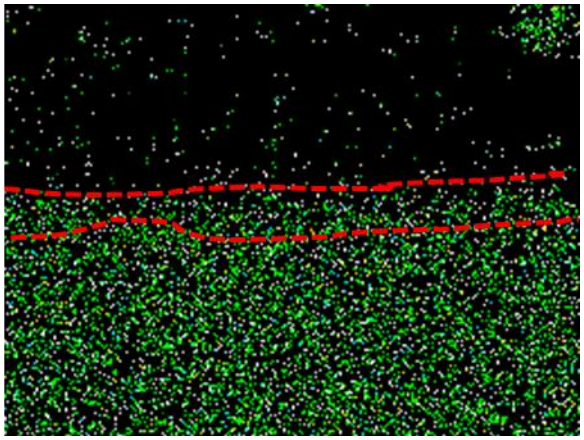

(c) Ca distribution

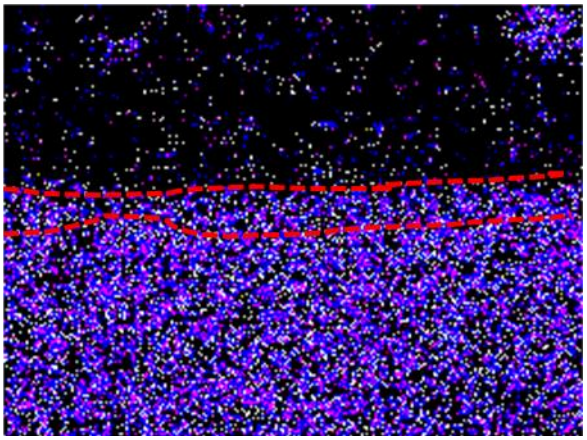

(d) P distribution

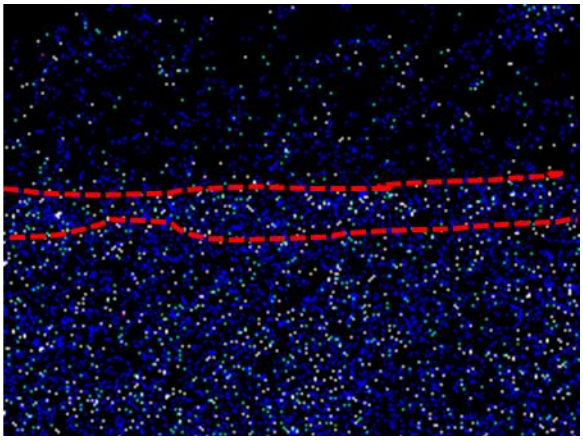

(e) O distribution

Figure 3.43: (a) SEM micrograph of the adhesive – dentin interface in the specimens treated with 14 J/cm^2 and bonded in self-etch mode and the 2D distributions of C (b), Ca (c), P (d) and O (e) elements as analyzed by EDX. The layer of material containing nanoparticles at the adhesive – dentin interface is indicated by the dashed red lines.

3.3.4. Shear test results

The average shear bond strength and the corresponding standard deviation of the mechanical tests of specimens prepared with different surface preparation methods are presented in Figure 3.44. The highest average bond strength (15.29 ± 3.38 MPa) is achieved for the specimens prepared by laser treatment with 14 J/cm² and etched before the adhesive application (total-etch mode). The specimens prepared with the mechanical burr and bonded without acid etching (self-etch mode) present the lowest average bond strength (9.18 ± 3.25 MPa). Average bond strengths in the range 11 – 12 MPa (± 2 – 4 MPa) are observed for all other specimens. The shear tests results of the experimental groups were statistically compared in pairs by t-test with a significance level of 5%. The statistical analysis results confirm that the bond strength of the specimens prepared by the burr and bonded in self-etch mode is significantly lower than the bond strength of those treated with a fluence of 14 J/cm² and bonded in total-etch mode but the other differences are not statistically meaningful due to the large standard deviations in the bond strength values.

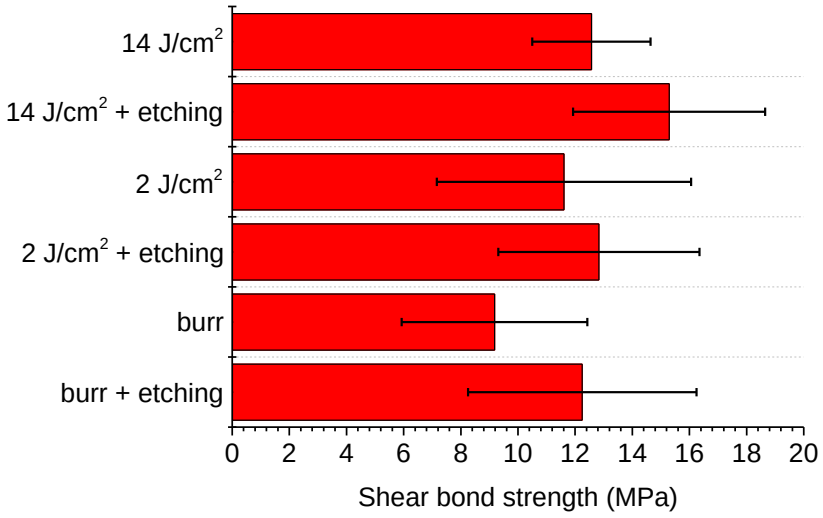

Figure 3.44: A comparison of shear bond strengths of dentin specimens prepared by tungsten carbide and by laser treatments with fluences of 2 and 14 J/cm² (N=10).

3.3.5. Analysis of the fracture mechanism

The fracture surfaces of the specimens in each experimental group were analyzed by SEM to identify the predominant failure mode. Micrographs of representative fracture surface morphologies are depicted in Figure 3.45 to Figure 3.47. The macroscopic cracks observed occasionally in those micrographs are mainly due to the dehydration process performed before the SEM observation. The morphology of the fracture surfaces can be categorized as follows:

- type A: the fracture surface presents traces of the adhesive and the underlying dentin is partially exposed. Removal of dentin from the substrate is negligible. This morphology indicates that the crack propagated mainly within the adhesive resin and a very thin surface region of the dentin substrate. Consequently, the mechanical failure in the shear test is a mixture of cohesive failure in the adhesive layer and adhesive failure at the adhesive – dentin interface[159].
- type B: the fracture surface is largely covered by adhesive, which shows signs of fracture. The area of the underlying dentin exposed is negligible. This morphology indicates that the crack propagated through the adhesive and the mechanical failure in the shear test occurred predominantly by cohesive failure in the adhesive.
- type C: a large proportion of the bond area presents traces of dentin fracture. Craters up to 1 mm deep are observed. The areas of adhesive resin remaining are negligible. This morphology indicates that the crack propagated within the dentin substrate and in the adhesive layer as well. Consequently, the mechanical failure in the shear test is a mixture of cohesive failure of dentin and adhesive failure, with the first one being predominant.

The propagation pathways of the fracture associated with the observed fracture surface morphologies are schematically described in Figure 3.48.

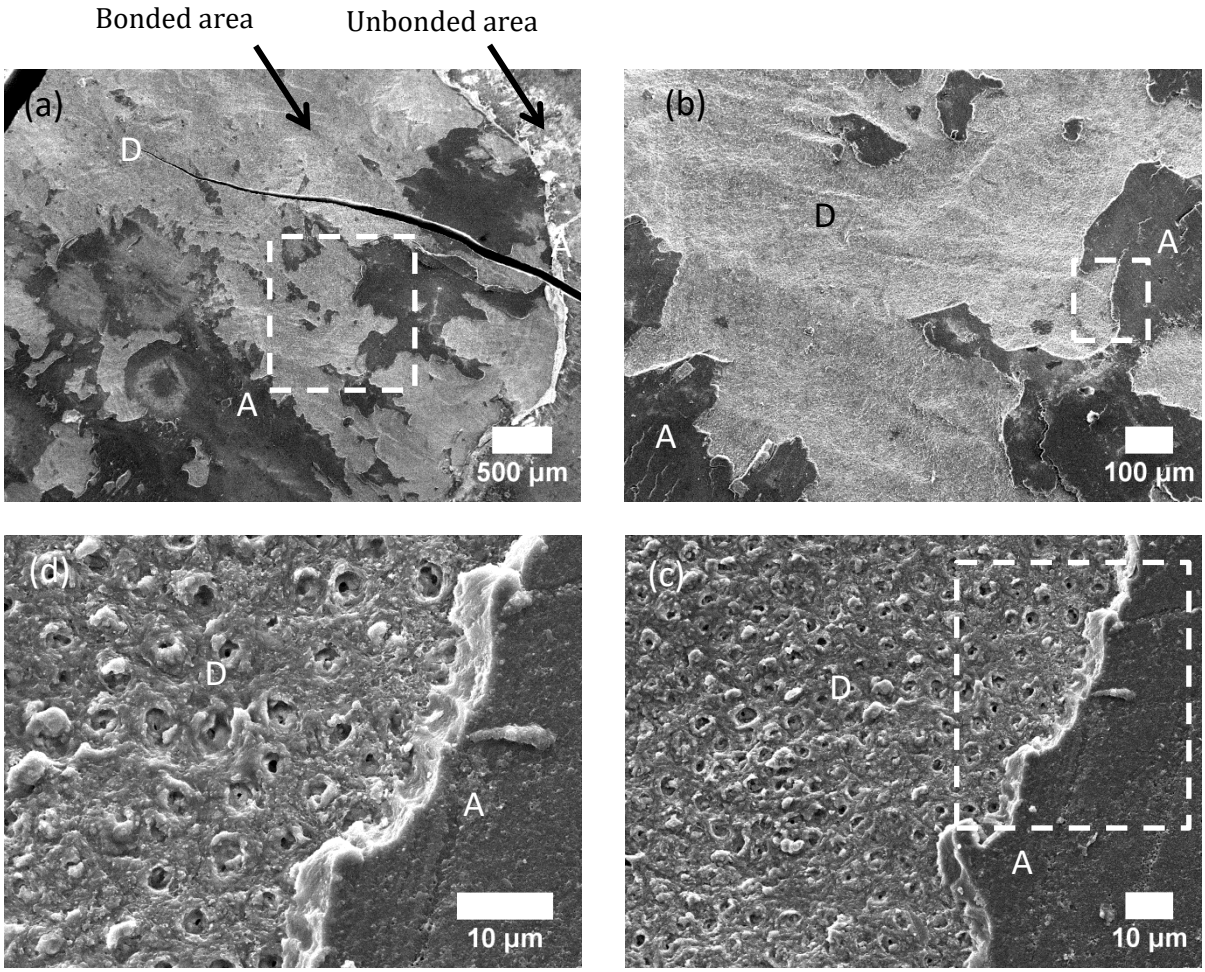

Figure 3.45: Representative SEM micrographs with a magnification of 25 (a), 100 (b), 1000 (c) and 2000X (d) of the type A fracture surface morphology. The areas depicted in Figures b, c and d are indicated by the dashed rectangles in Figures a, b and c, respectively. A portion of the fracture surface is still covered by the adhesive resin while the rest of it presents the exposure of the dentin surface with negligible signs of cohesive failure in the dentin. The exposed dentin surface appears bright while the adhesive resin remains appear dark in the micrographs.

Legend: A – adhesive, D –dentin.

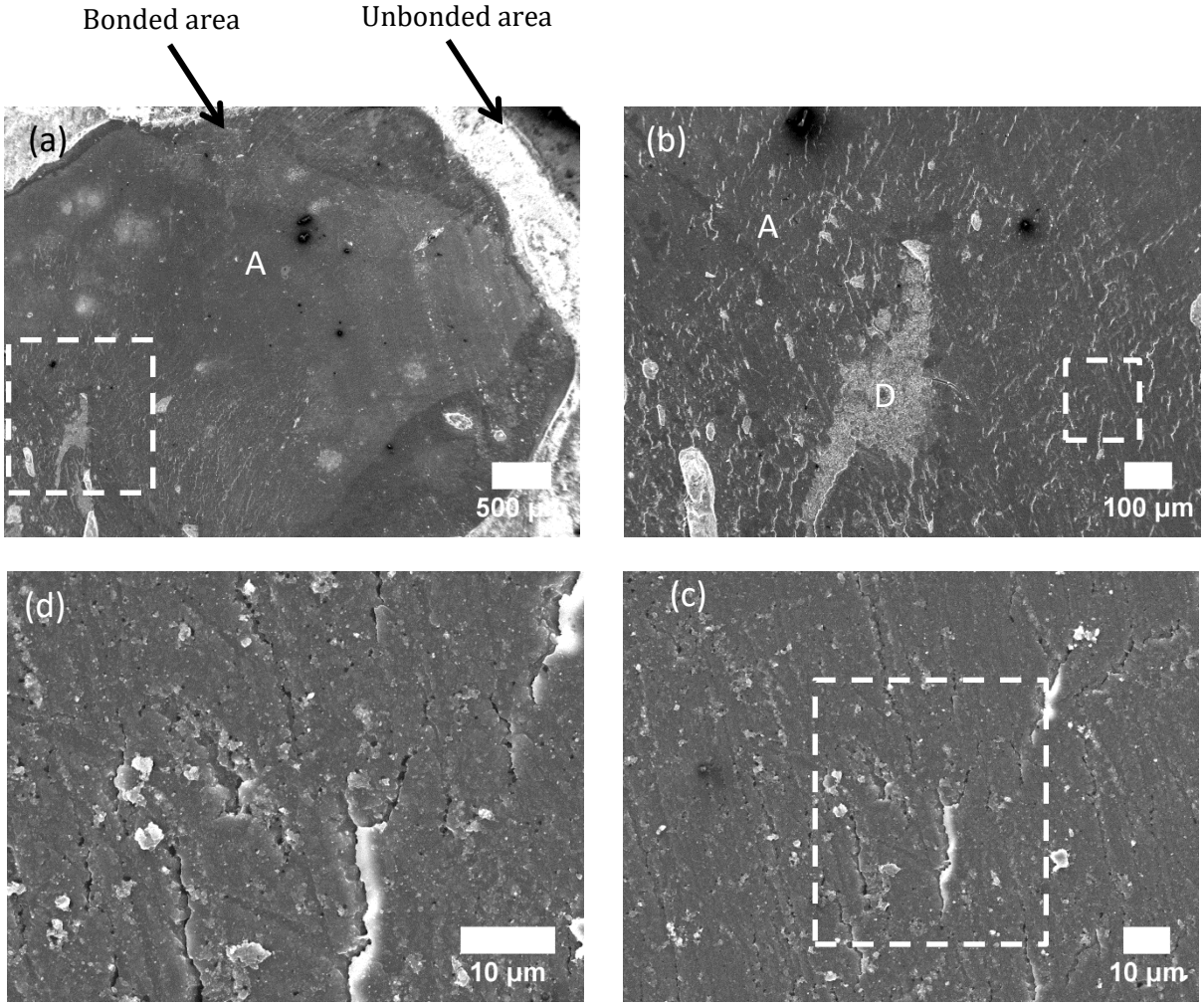

Figure 3.46: Representative SEM micrographs with a magnification of 25 (a), 100 (b), 1000 (c) and 2000X (d) of the type B fracture surface morphology. The areas depicted in Figures b, c and d are indicated by the dashed rectangles in Figures a, b and c, respectively. The fracture surface is largely covered by the adhesive resin layer that shows signs of fracture within the layer. The exposed dentin surface can only be observed in a small portion of the fracture surface. The exposed dentin surface appears bright while the adhesive resin remains appear dark in the micrographs.

Legend: A – adhesive, D –dentin.

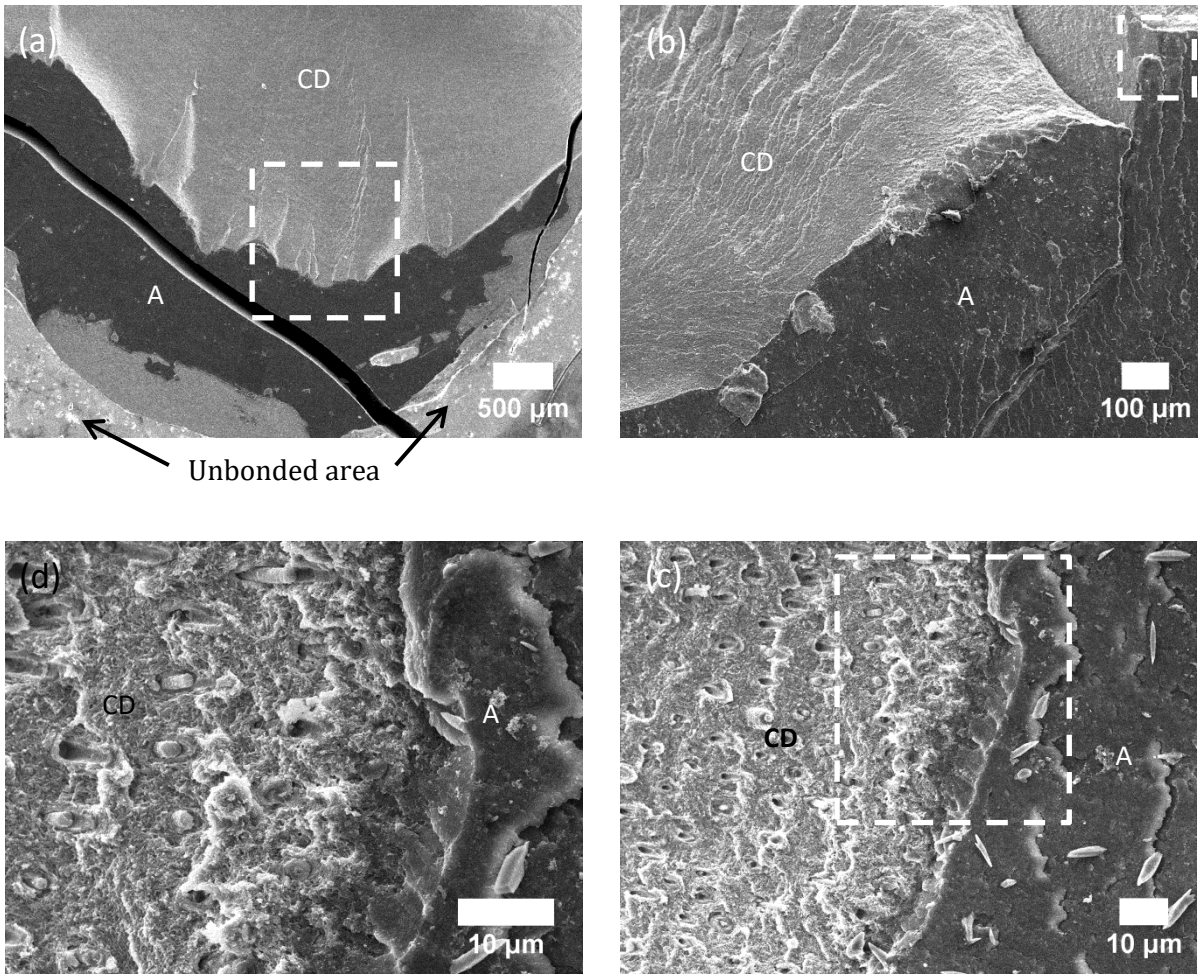

Figure 3.47: Representative SEM micrographs with a magnification of 25 (a) , 100 (b), 1000 (c) and 2000X (d) of the type C fracture surface morphology. The areas depicted in Figures b, c and d are indicated by the dashed rectangles in Figures a, b and c, respectively. A large portion of the fracture surface presents cohesive failure in dentin, which leads to the removal of a large amount of material in the dentin substrate at the bonded area. Traces of the adhesive resin are also observed but only at a small portion of the fracture surface. The exposed dentin surface appears bright while the adhesive resin remains appear dark in the micrographs. Legend: A – adhesive, CD – cohesively fractured dentin.

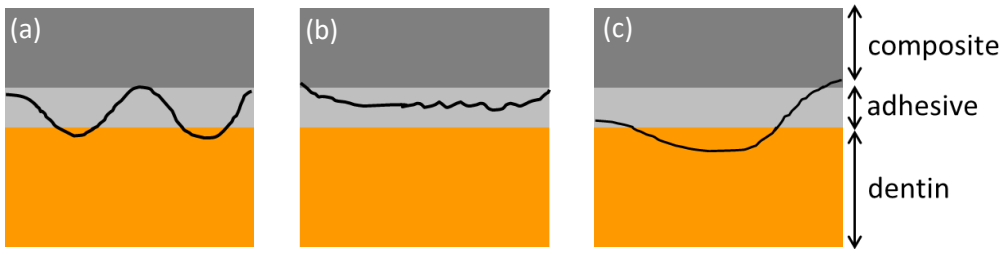

Figure 3.48: Schematic diagram of the propagation of the crack induced by the shear stress associated with type A (a), B (b) and C (c) fracture surface morphology.

Adapted from Scherrer et al.[159].

In the present work, the type A failure mode is mainly observed in the specimens prepared with the burr and bonded without acid etching. Most of the specimens of the other groups present a dominance of type C failure mode. The distribution of the failure modes observed in the present work is listed in Table 3.4.

Table 3.4: The distribution of the main failure modes in the specimens subjected to the shear tests (N=10)

Main failure mode	Burr + etching	Burr	2 J/cm² + etching	2 J/cm²	14 J/cm² + etching	14 J/cm²
Adhesive failure (type A)	2	7	1	0	0	2
Mixed failure predominated by cohesive fracture in the adhesive resin (type B)	2	2	2	2	3	2
Mixed failure predominated by cohesive fracture in the dentin (type C)	6	1	7	8	7	6

4. General discussion

The discussion of the experimental results obtained in the present work is organized as follows:

- Ablation threshold and incubation coefficient of enamel and dentin
- Morphological, structural and constitutional modifications of enamel and dentin surfaces induced by the femtosecond laser treatment.
- Ablation mechanisms of enamel and dentin.
- Ablation rate of enamel and dentin.
- Laser – induced heating of teeth during the laser treatment and effect of external cooling on the temperature increase and on the morphology and chemical constitution of laser treated dentin surfaces.
- Adhesion of restorative materials to dentin surfaces treated by femtosecond laser.

4.1. Ablation threshold and incubation coefficient

In the present work, the single pulse ablation thresholds of enamel and dentin, determined by the D^2 method, are 2.72 ± 0.30 and 1.49 ± 0.13 J/cm^2, respectively. The ablation threshold decreases with increasing number of laser pulses. A similar evolution of the ablation threshold with the number of laser pulses was observed for other materials and is usually explained by the generation of chemical/structural defects in the material even for radiation fluences below the ablation threshold [14,94,106,160,161]. Since the electronic energy levels of such defects lie within the band gap of the material, their presence allows electrons to be excited by absorption of a lower number of photons than those required for a intraband excitation process, increasing the coefficient of absorption of the radiation by the material. The fluence required to start the ablation process decreases with increasing number of laser pulses because the laser-induced defects are created by each laser pulse and accumulate in the material. The incubation effect, demonstrated in Figure 4.1, is characterized by the incubation coefficient S, proposed by Jee et al.[106]. In the present work, the incubation

coefficients of enamel and dentin calculated by using equations 2.7 and 2.8 are 0.74 ± 0.03 and 0.79 ± 0.01, respectively.

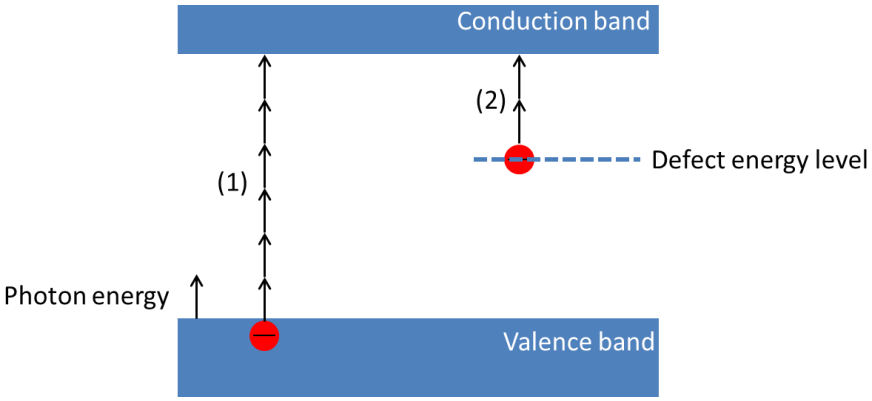

Figure 4.1: A schematic diagram of the electronic structure of a dielectric material. The electron excitation by multiphoton absorption process is demonstrated for the intrinsic material (1) as well as for the material with the presence of laser-induced defects (2). The arrows indicate the photon energy of the laser radiation.

The values of the ablation threshold of dental hard tissues found in the literature were determined by wide range of different methods including the D^2 method[123] used in the present work, ablation rate regression[15,16] and microscopic observation of the ablation surface[17,162]. The ablation rate regression method is based on the assumption that a specific ablation mechanism predominates for a particular material and affects the relation between the ablation rate and the radiation fluence. The ablation threshold is then determined by extrapolating the ablation rate to 0 in a plot of ablation rate versus fluence[15,16]. The determination of ablation threshold based on microscopic observation of the ablation surface relies on the observation of a threshold fluence at which the surface damage can be observed by optical or electron microscopy. The different methods of ablation threshold determination can lead to different values of the threshold[163]. The large dispersion of the ablation threshold values reported in the literature is also caused by differences in specimen preparation methods and differences in some laser processing parameters (radiation

wavelength, laser pulse duration etc.), which can significantly affect the radiation absorption of the tissues. Therefore, any comparison of the ablation threshold values obtained in the present work with those reported in the literature is hazardous. Nevertheless, the observation that the ablation threshold of enamel is significantly higher than that of dentin agrees with the results reported by other authors[18,25]. The difference might be explained by the difference in the ablation mechanisms of dentin and enamel, which will be discussed in detail in the following section. Moreover, the values of the incubation factor determined in the present work for the dental hard tissues are in good agreement with the values reported for cortical bone[14,20], a tissue with a constitution similar to dentin.

4.2. Characterization of the ablation surfaces and the ablation mechanisms of dental tissues

The SEM micrographs of craters produced on enamel (Figures 3.4 – 3.7) at 1 Hz pulse repetition rate show the presence of a resolidified material layer. This layer exists even for 5 laser pulses and an average fluence of 4 J/cm^2, approximately 2 times higher than the ablation threshold of enamel in this condition (1.86 J/cm^2, Section 3.1.1a). This observation indicates that the ablation of enamel is dominated by thermal processes, involving heating of the tissue surface to a temperature higher than 1600^{o}C, the melting temperature of carbonated hydroxyapatite[134,164], followed by the ablation by either phase explosion or liquid spallation. The pores and traces of bubbles observed in the resolidified layer show that the liquid decomposed, resulting in the release of gases. According to Holcomb et al.[165] and Fowler et al.[133], enamel decomposes at temperatures above 100^{o}C, much lower than its melting point[134,165], releasing gaseous water and CO_2. These reactions cannot occur in the present case due to the extremely fast heating rate and decomposition of enamel only occurs after melting, leading to gas release within the liquid.

On the contrary, no signs of resolidified material are observed in the SEM micrographs of the dentin ablation surfaces produced with similar laser processing conditions. The structure of dentin can be observed in the laser ablation craters, regardless of the fluence and number of laser pulses used, indicating that the thermal effects involved in the ablation process of dentin are negligible, as opposed to what happens with enamel. This difference is certainly due to the different structure of these tissues. While enamel consists mainly of hydroxyapatite (96% wt.%), dentin is a composite material consisting of hydroxyapatite nanocrystals dispersed in a network of collagen fibrils. Despite the fact that the predominant phase of dentin is hydroxyapatite (~ 70 wt.% in average), its cohesive strength is ensured by the collagen fibrils[29]. These fibrils consist of long molecular chains in which the atoms are bonded by covalent bonds, connected to one another by weak Van der Waals forces. As a result, collagen presents lower thermal stability[52] and lower ablation threshold for femtosecond laser radiation (0.06 J/cm^2)[141] than enamel, which consists entirely of hydroxyapatite (3.3 J/cm^2) [166]. Collagen can be decomposed for relatively low radiation intensities. The removal of collagen reduces the cohesive strength of dentin and facilitates its ablation by a predominant photomechanical mechanism for radiation intensities much lower than those required to ablate hydroxyapatite-rich enamel and crystalline hydroxyapatite, which are ablated by liquid spallation or phase explosion, depending on the laser processing parameters[11,16,166]. This photomechanical ablation mechanism was initially proposed by Eugenio et al.[11] for the ablation of dentin by 248 nm laser radiation and, more recently, by Domke et al.[119] for the ablation of dentin by femtosecond laser on the basis of pump-probe experiment results.

The influence of collagen on the ablation of dentin was studied by immersing a dentin specimen in NaOCl solution to partially remove collagen from its surface region before the laser ablation experiments. Traces of resolidified material can be observed in the ablation craters even for an average fluence as low as 2 J/cm^2, 1 Hz pulse repetition rate and 5 laser pulses. Even though the amount of resolidified material observed in those craters is much lower than that observed in the

craters created on enamel surface using similar laser parameters, this result clearly indicates that once collagen is removed, laser ablation of dentin occurs by melting, followed by liquid ejection and vaporization.

At 1 kHz pulse repetition rate, a large amount of redeposited ablation debris is observed on the laser treated dentin and enamel surfaces. MicroRaman and FTIR analysis show that the ablation debris consist mainly of amorphous calcium phosphate, formed due to the rapid cooling of calcium phosphate from the vapor and the liquid phase[167]. The observation indicates the contribution of thermal mechanisms such as liquid spallation and phase explosion in the ablation of the dental hard tissues at high repetition rates [101,103]. For enamel, a layer of resolidified material is observed on the laser treated surfaces after the removal of the redeposited debris but its thickness is negligible in the specimens treated with 4 and 9 J/cm^2 and measurable in the specimen treated with 14 J/cm^2 (~1.5 μm). The structure and chemical constitution of the enamel below this layer is unaltered, as indicated by SEM, GI-XRD and microRaman analysis. Since the thickness of the resolidified layer is lower than the depth of analysis of microRaman spectroscopy (4.6 μm, Section 2.3.3a) and GI-XRD (5 μm, Section 2.3.2), these analytical methods probe both the laser modified layer and the substrate and it is difficult to analyze only the altered layer. The presence of the resolidified droplets at the laser treated dentin surfaces indicates that melting of the hydroxyapatite occurs during dentin ablation at 1 kHz laser pulse repetition rate, but, as before, the structure and constitution of the dentin at the surfaces are not significantly altered, even for an average fluence of 14 J/cm^2. Considering that the depth of analysis of the FTIR is 0.6 μm for the spectral region of collagen (1250 – 1650 cm^{-1}), the similarity between the spectra of polished and laser treated specimens indicates that the laser – modified region in dentin is lower than 0.6 μm.

4.3. Ablation rate of dentin and enamel

In the present work, the ablation rate of dentin and enamel was studied for average fluences in the range 2 – 14 J/cm^2, a pulse repetition rate of 1 kHz and an average number of laser pulses per surface location of 14. Within this range of laser processing conditions, the amount of material ablated per laser pulse is significantly higher for dentin than for enamel, in good agreement with the observation reported by others[18,25,117]. This result can be explained by the presence of organic compounds and water, which have lower bond energy than hydroxyapatite[11], with higher content in dentin than in enamel. In addition, the evolution of enamel ablation rate with fluence presents a saturation for average fluences higher than 8 J/cm^2 (Figure 3.9), which is not observed for dentin (Figure 3.24). Some authors suggested that the ablation rate can be expressed as a function of $\ln(F/F_{th})$ based on the assumption that the radiation penetration depth in a material can be described by the Lambert-Beer law[95,105,168]. However, this suggestion does not take into consideration the progressive increase of the depth and the curvature of the ablation surfaces, which can significantly affect the effective radiation fluence. Therefore, deviations from the suggested $\ln(F/F_{th})$ dependence are expectable in the present work, where the depth of the ablation craters (7 – 35 μm) is higher than the maximum depths of 0.9 and 3 μm obtained by Ben-Yakar et al.[168] and Semaltianos et al.[105], respectively, which imply a more significant increase of the ablation surface area. Further studies are needed to investigate the observed difference in the evolution of ablation rate with fluence between dentin and enamel.

The volume of material removed per second (mm^3/s) by the femtosecond laser can be determined from the ablation volume per laser pulse by taking into consideration the pulse repetition rate used in the experiments. The maximum removal rate found in the present work is $0.44 * 10^{-2}$ mm^3/s and $0.25 * 10^{-2}$ mm^3/s for dentin and enamel, respectively, for an average fluence of 14 J/cm^2. It must be emphasized that the values were obtained for healthy tissues. Engelbach et al.[169] reported that the ablation rate of carious tissues by ultrashort pulsed lasers is 2 -3 times higher than that of healthy

tissues, due to the absence of hydroxyapatite and the abundance of water and organic matters in the carious tissues[170]. Nevertheless, the material removal rates obtained for ultrashort pulsed lasers are significantly lower than the value obtained by drilling (~1 mm^3/s)[117,169], indicating the need to increase the radiation fluence and the pulse repetition rate to make femtosecond lasers suitable for clinical applications. Despite the possibility to achieve high ablation rate, the ablation of dental tissues in such conditions needs to be systematically studied before being used for dental treatments since the thermal effects induced during the ablation process increase with the laser pulse repetition rate as well as fluence.

4.4. Laser-induced heating of the teeth and the influence of external cooling

A study on the femtosecond laser ablation of cortical bone, a tissue with a constitution similar to dentin, carried out by Cangueiro et al.[23], showed that, despite the absence of thermal degradation of the tissue, during prolonged laser treatments heat accumulates in the tissue and large temperature increases occur if no external cooling is provided. A substantial increase of temperature was observed for pulse repetition rates and average fluences as low as 50 Hz and 2 J/cm^2, respectively. This increase in the tissue average temperature leads to an increasing presence of thermal effects, such as liquid droplet ejection and thermal exfoliation of the tissue[23]. At a pulse repetition rate of 2 kHz, the laser treated surface presented signs of carbonization and cracking due to excessive heating. The same problem occurred for the ablation of dentin or dental enamel. The redeposition of resolidified droplets was observed on the tissues surfaces treated by the femtosecond laser in the average fluence range 2 – 14 J/cm^2 and pulse repetition rate of 1 kHz. The observation indicates a large influence of thermal effects in the ablation of the tissues in these processing conditions and the possibility of undesirable heat accumulation in the teeth, which can cause irreversible damage to the soft tissues in the pulpal chamber[171,172]. Zach et al.[171] observed pulp necrosis when the temperature in the pulp reaches 42.5°C, a value 5.5°C higher than the initial temperature of 37°C.

The present work showed that the temperature increase in the pulp may reach 17.5°C for laser treatments with a pulse repetition rate of 1 kHz and 14 J/cm^2 average fluence if no external cooling is used. The average temperature increase in the pulpal chamber was 3.1, 9.5 and 14.6°C for laser treatments performed with average fluences of 2, 7 and 11 J/cm^2, respectively. Bello – Silva et al.[31] observed a temperature increase of up to 4.2°C at the surface of 1 mm thick dentin disks treated on the opposite face with 500 fs duration laser pulse of 1045 nm radiation at an average fluence of 4.4 J/cm^2 and pulse repetition rate of 100 kHz [31]. The authors did not indicate the duration of the laser treatment so a direct comparison with the present results is impossible. Pike et al.[173] and Chang et al.[174] also measured the temperature rise on dentin surfaces irradiated with femtosecond laser pulses and compared the experimental values with mathematical simulation results, but these studies were performed with fluences lower than the ablation threshold of dentin and, therefore, are not relevant for comparison. It must be emphasized that the increase of the pulpal chamber temperature due to the laser treatment depends on a wide range of factors, including the laser processing parameters, the laser treatment duration, specimen geometry and dimensions, distance between the laser treated surface and the pulpal cavity, thermal properties of the tooth, etc.. In a clinical situation, the temperature increase will also be affected by the flow of dentinal fluid in the teeth, a factor not considered in the present work as well in the work of Bello – Silva et al.[117,175]. Therefore, differences are expected between the results obtained in the laboratory and in clinical practice. Nevertheless, the results obtained in the present study as well as those reported by Bello – Silva et al.[117] show that external cooling is mandatory to avoid the necrosis of the pulp, in particular when high fluences and high repetition rates are employed to achieve large material removal rates or if the treatment is carried out in the vicinity of the pulpal chamber.

The influence of external cooling by air jet and water irrigation was studied since these cooling methods are commonly used in the clinical caries removal treatments with burrs used with a turbine or with Er:YAG and Er, Cr:YSGG lasers. The results show that the cooling effect of the air jet

is insufficient and this cooling method leads to a significant redeposition of ablation debris, which form a continuous poorly adherent layer for high average fluences (7 and 14 J/cm^2). This layer must be removed before the restoration to prevent it to reduce the adhesion between restorative materials and dentin. The chemical analysis performed showed that, within the range of processing parameters used, the constitution and structure of dentin are not affected by the laser treatment and that chemical changes only affect the ablation debris. The FTIR spectra of these debris are similar to those of amorphous calcium phosphate (ACP)[145,146], indicating that this is the main constituent of the debris. The large amount of redeposited debris formed with air cooling indicates that thermal effects are more important in these conditions, as suggested by Cangueiro et al.[23] for cortical bone. The flow of air impinging on the specimen's surface seems to dehydrate the tissue, reducing the dentin's heat capacity, due to the higher heat capacity of water (4.18 J/g^{o}C) as compared to that of hydroxyapatite (0.71 J/g^{o}C)[147].

Water irrigation reduces significantly the temperature increase observed during the laser treatment, by improving heat dissipation. It also reduces the amount of redeposited ablation debris, which are carried away by the flowing water, and the tendency of dentin to dehydrate during the laser treatment, thus reducing thermal effects during ablation[23]. Contrarily to the observations of Bello – Silva et al.[117] and Cangueiro et al.[23], in the present work the ablation rate was not significantly reduced with the water cooling. The reductions observed by those authors were due to the absorption of radiation by water[34], in particular when this water contains significant proportions of ablation debris in suspension. In the present case, radiation absorption by water film was decreased by directing a complimentary air jet to the laser interaction region, allowing high ablation rates to be achieved.

4.5. Adhesion of self-etch adhesive to laser treated dentin surfaces

In the present work, the adhesion of restorative materials to dentin surfaces prepared by laser treatment was studied and compared with the adhesion to dentin surfaces prepared by conventional drilling. The surface preparation and bonding procedures are described in detail in Section 2.4.1.

The dentin surfaces prepared by the burr are covered by a dense smear layer 1 – 2 μm thick, which also extends approximately 1 – 2 μm into the underlying dentinal tubules. It is reported that this layer consists mainly of calcium phosphate debris and collagen fragments formed by the abrasion of the tissue and has low adhesion to the underlying dentin substrate[70,80]. When the etchant gel was used (total – etch mode), the smear layer was completely removed and the underlying dentin was partially demineralized, allowing the formation of the resin tags and a hybrid layer 2 – 3 μm thick as indicated in the SEM micrographs of the adhesive – dentin interface (Figures 3.41a and b). As a result, strong adhesion between the adhesive and the dentin substrate (12.25 ± 4.00 MPa) was achieved mainly by a micromechanical interlocking mechanism[70,74]. On the contrary, no resin tags were observed in the specimens prepared with the burr when the adhesive resin was applied directly without acid etching (self - etch mode). Moreover, no hybrid layer was observed in these specimens. This observation is in good agreement with the results of Mine et al.[77] and Koshiro et al.[176] for dentin surfaces bonded by ultramild self – etch adhesives (pH ~2.0 – 2.9, similar to the adhesive resin used in the present work pH ~2.5 – 3.0). The authors showed that, in these conditions, the smear layer was not completely dissolved, but was impregnated in the adhesive resin to form a resin - smear complex at the interface. The hybrid layer at the dentin surface was less than 100 nm thick[77,176] and, therefore, could not be resolved by the SEM method used in the present work. In addition, only few resin tags formed due to the incomplete dissolution of the smear plugs. The authors suggest that the adhesive – dentin adhesion in this case is a combination of submicron mechanical interlocking and of the chemical interaction between the

methacryloyloxydecyl dihydrogen phosphate (MDP) monomers existing in the adhesive resin molecules and hydroxyapatite[70,77]. This adhesion mechanism is expected for the Adhese Universal ® adhesive tested in the present work since it also contains MDP monomers. The shear bond strength obtained by the self – etch mode (9.18 ± 3.25 MPa) was slightly lower than the shear bond strengths obtained with the total – etch mode (12.25 ± 4.00 MPa), indicating that acid etching before bonding is required to improve adhesion between the adhesive and dentin. The present results are in good agreement with those reported by previous authors[78,177,178]. Those authors also recommend the use of acid etching in the case of ultramild self-etch adhesives to ensure high bond strengths. It must be emphasized that the bond strength of ultramild self-etch adhesives can be overestimated if the dentin surfaces are prepared by polishing with SiC abrasive papers, a method sometimes used due to the ease of preparation[9,74,77,87]. Mine et al.[77] showed that the smear layer produced by polishing with SiC papers is less dense and, hence, can be better dissolved by the self-etch adhesives than the smear layer produced by burrs. As a result, the adhesive resin can infiltrate better the dentin surface, leading to better adhesion.

Contrarily to dentin surfaces prepared with burrs, the structure of dentin after laser treatment was well-preserved and the tubules remained open. When etching was performed on the laser treated surfaces, the demineralized layer presented micron sized holes, regardless of the fluence used (Figure 3.38). The observation indicates that the subsurface collagen molecules may have been partially removed by laser ablation via photothermal or photochemical mechanisms[109,111,179] or simply thermally denatured due to the surface temperature increase during the laser treatment[23]. The FTIR and cross sectional SEM analysis of the demineralized layer showed that the thickness of this layer is lower in the specimens treated with 14 J/cm^2 than in the specimens treated with 2 J/cm^2 or prepared with burrs. The difference might be explained by the substantial heat accumulation induced in dentin during the laser treatment with 14 J/cm^2, which was sufficient for thermal denaturation of collagen near the surface ($T_{denaturation} \sim 160\ ^oC$[23,151]), leading to lower

content of surface collagen after etching. At the denaturation temperature of collagen, decomposition of carbonate anions in carbonated hydroxyapatite could also occur ($T_{decomposition}$ ~ 100 – 650 ^{o}C[133,152]), which increased dentin´s resistance to acids, leading to a demineralization rate of dentin lower in the specimens treated with 14 J/cm^2 than in the specimens treated with 2 J/cm^2 or prepared with burrs. The denaturation of collagen and the decomposition of carbonate ions in the laser treated specimens was limited to a surface region with thickness lower than the probing depth of FTIR (~ 0.7 μm and 0.6 μm for 1415 cm^{-1} carbonate peak and 1650 cm^{-1} amide I peak, Section 2.3.3.b).

The demineralization of laser treated dentin surfaces allowed forming hybrid layers 2 – 3 μm and 1 – 2 μm thick in the specimens treated with 2 and 14 J/cm^2, respectively (Figure 3.41). Resin tags are also observed in those specimens. The shear bond strength obtained for the specimens treated with 14 J/cm^2 (15.29 ± 3.38 MPa) was slightly higher than for the specimens treated with 2 J/cm^2 (12.83 ± 3.55 MPa) or prepared with burrs (12.25 ± 4.00 MPa) and etched prior to adhesive application. When the bonding was performed without etching, resin tags formed in laser treated specimens because the dentinal tubules remained open. However, the hybrid layer could not be distinguished in the specimens treated with 2 J/cm^2, probably due to its low thickness[77]. On the contrary, the specimens treated with 14 J/cm^2 presented a layer consisting of calcium phosphate nanoparticles at the adhesive – dentin interface, which is partially dissolved and impregnated in the adhesive resin. This layer was certainly formed because the thermal decomposition of carbonate ions in a superficial layer of dentin resulted in an increase of the resistance of the phosphate to acids. The formation of this layer had no negative effects on the adhesive-dentin adhesion. The bond strength for the specimens treated with 14 and 2 J/cm^2 (12.57 ± 2.08 MPa and 11.61 ± 4.45 MPa, respectively) and bonded without etching are similar.

In the present study, the adhesive-dentin bond strength obtained after laser treatment, regardless of the radiation fluence and bonding method, is comparable to that obtained with the burrs after

etching. On the contrary, lower bond strengths are obtained for burr – cut dentin when the adhesive is applied without etching. In this case, the adhesive fail to penetrate the weakly attached smear layer to bond to the underlying dentin, leading to lower adhesion and crack propagation, in the mechanical tests, predominantly at the interface. On the contrary, the specimens in other groups show mainly cohesive failures in dentin in the mechanical tests, but this does not imply mechanical weakening of dentin due to the laser treatment as suggested by Domke et al.[119] because the cracks do not propagate through the superficial region of the laser treated surface (Figure 3.27).

The strong bond strength of the laser – treated specimens observed in the present work is in contradiction with the results reported by Portillo et al.[87]. These authors reported that the bond strength obtained for dentin surfaces prepared by polishing is significantly higher than for dentin treated with a Ti:sapphire laser with radiation wavelength of 780 nm, pulse duration of 120 fs, operating at pulse repetition rate of 1 kHz, and a laser fluence of 39.8 J/cm^2. It is likely that the low bond strength observed by Portillo et al. [87] is due to the use of high fluences, which may cause structural and constitutional alterations of dentin or formation of a layer of redeposited ablation debris covering the dentin surface. As shown in the present work, this layer consists mainly of resolidified droplets formed by melting and rapid resolidification of hydroxyapatite, which have high acid resistance due to the absence of carbonate anions in their structure[133,152,180]. Consequently, the redeposited materials must be removed prior to bonding to ensure good adhesion. The present work shows that these debris can be completely removed by ultrasonication.

The adhesion study performed in the present work confirms the potential of this technology as an alternative to Er:YAG, Er,Cr:YSGG lasers and to conventional burr drilling. Burrs offer higher material removal rates but induce pain due to the mechanical stimulation, leading to the need of anesthesia[64]. In addition, acid etching is required prior to adhesive application to remove the smear layer and achieve high bond strength between the adhesive and dentin. On the other hand, Er:YAG and Er,Cr:YSGG lasers, the main type of lasers presently used in clinics, cause negligible pain and the

ablation dentin surface presents a micro-retentive morphology with open tubules, seemingly suitable for the adhesive/dentin adhesion[83,125,181,182]. Several authors reported that the bond strength obtained for dentin treated by these lasers, even without acid etching, was comparable to the bond strength obtained for dentin prepared with burrs[84,85]. On the contrary, other authors showed that, for a certain range of laser processing conditions, the laser treatment had a negative impact on the adhesive/dentin adhesion[8,9,42,74,86], which was explained by the structural and constitutional alteration of the tissue by the laser. Ceballos et al.[74] and Moretto et al.[9] observed a 3 – 5 μm thick collagen depleted layer, followed by another layer about 1μm thick containing partially denatured collagen on surfaces treated with Er:YAG (23 J/cm^2 and 2 Hz)[74] and Er, Cr:YSGG (90 J/cm^2 and 20 Hz)[9]. These alterations decrease the bond strength[86] and limit the infiltration of collagen by the adhesive to form a hybrid layer[9,74]. Moreover, sub-superficial cracks parallel to the surface are observed in samples treated with Er:YAG laser with radiation fluence of 31.45 J/cm^2, 10 Hz pulse repetition rate[183] and with Er, Cr:YSGG laser with radiation fluence of 90 J/cm^2 and repetition rate of 20 Hz[9], which formed due to the shockwave created by the explosive evaporation of water. These cracks reduce the mechanical strength of the tissue and facilitate cohesive failures in the adhesion test[9,184].

5. Conclusion

The general aim of the present work was to study the ablation of dental hard tissues, enamel and dentin by femtosecond lasers and to evaluate the potential of this technology in dental caries removal treatment.

The single pulse ablation threshold values of enamel and dentin were determined to be 2.72 ± 0.30 and 1.49 ± 0.13 J/cm^2, respectively. The ablation threshold decreased with increasing number of laser pulses, a variation explained by the accumulation of radiation – induced defects in the materials, which could facilitate the radiation absorption by the material. The incubation coefficients of enamel and dentin were 0.74 ± 0.03 and 0.79 ± 0.01, respectively. The analysis of the laser treated surfaces indicated that the ablation of enamel was accompanied by melting, regardless of the laser processing parameter used (average fluences in the range 4 – 14 J/cm^2 and pulse repetition rates of 1 and 1000 Hz), but melting was limited to thin surface region of the treated specimens. The layer of resolidified material in the specimens treated with 14 J/cm^2 and 1 kHz pulse repetition rate was less than 1.5 μm thick. The chemical constitution and structure of enamel below the resolidified material was not altered. The ablation surfaces of dentin showed no signs of resolidified material even for the laser treatments performed with 14 J/cm^2 and 1 kHz pulse repetition rate. The chemical constitution and structure of dentin were well-preserved within the ranges of laser parameters used (average fluences in the range 2 – 14 J/cm^2 and pulse repetition rates of 1 and 1000 Hz).

The difference in the ablation mechanism of dentin and enamel can be explained by the preferential ablation of collagen in dentin, which occurs at lower fluences than hydroxyapatite and reduces significantly the cohesive strength of the tissue, facilitating dentin ablation predominantly by a photomechanical solid spallation instead of photothermal ablation mechanism of enamel.

The bond strength of the tested self-etch adhesive product, measured by shear tests, to dentin surfaces treated by the femtosecond laser with average fluences of 2 and 14 J/cm^2, regardless of

acid etching, is similar to the bond strength to dentin surfaces prepared with a tungsten carbide burr and etched before adhesive application. On the contrary, the burr – cut specimens that were bonded without acid etching presented relatively lower bond strength, probably due to the low etching capability of the adhesive resin tested, which caused incomplete dissolution of the smear layer needed for the bonding of the adhesive to the underlying dentin substrate.

The temperature measurement performed in the present work showed that the laser – induced heat transfer to the tooth bulk cannot be avoided, despite the negligible contribution of thermal effects in the femtosecond laser ablation of dental hard tissues. An increase of the pulpal cavity temperature of human molars of 3.1°C was observed when the laser treatment was performed with 2 J/cm^2, 1 kHz pulse repetition rate, 5 mm/s scanning velocity and during 240 s duration. The temperature rise reached a value of 17.5 °C during the laser treatment performed with 14 J/cm^2. The result shows that external cooling must be systematically used during laser treatments, especially when the treatments are performed with high fluences and pulse repetition rates to achieve high material removal rates. In the present work, the use of a lateral air jet and a combination of the air jet and water irrigation during the laser treatments allowed remarkable reduction of the temperature rise in the pulpal chamber without significant influence on the ablation rate. The temperature increase observed during the laser treatment with 14 J/cm^2 with a lateral air jet and with a combination of the air jet and water irrigation was 10.8 °C and 6.6 °C, respectively.

The present work demonstrates that femtosecond lasers can be considered as an alternative method for the dental caries removal treatment. The negligible contribution of thermal effects in the ablation process, in particular for dentin, allows preserving the structure and constitution of the tissues. Dentin specimens treated by the laser within the tested range of laser parameters can form adequate adhesion with the restorative adhesive resin. Nevertheless, the number of specimens in each experimental group for the adhesion tests was relatively low (N=10). Due to the large sample-to-sample variations usually observed for biological samples, the future adhesion test should be

performed with a higher number of specimens to increase the precision of the bond strength evaluation. In addition, several adhesive products should be tested to obtain a better assessment of the potential of femtosecond lasers in dental caries removal treatment.

The potential of femtosecond lasers for clinical applications can be improved if higher material removal rates can be achieved. Pulse repetition rates and fluences higher than the values tested in the present work are needed to obtain a removal rate comparable to that obtained for drilling. The ablation of dental hard tissues in those conditions needs to be performed in the future work.

Bibliography

1. Maiman, T. H. Stimulated Optical Radiation in Ruby. *Nature* **187,** 493–494 (1960).
2. Goldman, L., Gray, J. A., Goldman, J., Goldman, B. & Meyer, R. Effect of laser beam impacts on teeth. *J. Am. Dent. Assoc.* **70,** 601–606 (1965).
3. Goldman, L., Hornby, P., Meyer, R. & Goldman, B. Impact of the laser on dental caries. *Nature* **203,** 417 (1964).
4. Sanchez, F., Espana Tost, A. J. & Morenza, J. L. ArF excimer laser irradiation of human dentin. *Lasers Surg. Med.* **21,** 474–479 (1997).
5. Fried, D., Seka, W., Glena, R. E. & Featherstone, J. D. B. Thermal response of hard dental tissues to 9- through 11-μm CO2-laser irradiation. *Opt. Eng.* **35,** 1976–1984 (1996).
6. Armengol, V., Jean, A. & Marion, D. Temperature rise during Er : YAG and Nd : YAP laser ablation of dentin. *J. Endod.* **26,** 138–141 (2000).
7. Camerlingo, C., Lepore, M., Gaeta, G. M., Riccio, R., Riccio, C., De Rosa, A. & De Rosa, M. Er : YAG laser treatments on dentine surface: micro-Raman spectroscopy and SEM analysis. *J. Dent.* **32,** 399–405 (2004).
8. Cardoso, M. V, Coutinho, E., Ermis, R. B., Poitevin, A., Van Landuyt, K., De Munck, J., Carvalho, R. C. R., Lambrechts, P. & Van Meerbeek, B. Influence of Er,Cr : YSGG laser treatment on the microtensile bond strength of adhesives to dentin. *J. Adhes. Dent.* **10,** 25–33 (2008).
9. Moretto, S. G., Azambuja Jr., N., Arana-Chavez, V. E., Reis, A. F., Giannini, M., Eduardo Cde, P. & De Freitas, P. M. Effects of ultramorphological changes on adhesion to lased dentin-Scanning electron microscopy and transmission electron microscopy analysis. *Microsc. Res. Tech.* **74,** 720–726 (2011).
10. Hashiguchi, K. & Hashimoto, K. Effects of KrF excimer laser irradiation on human dental enamel. *Okajimas Folia Anat Jpn* **76,** 321–333 (2000).
11. Eugenio, S., Sivakumar, M., Vilar, R. & Rego, A. M. Characterisation of dentin surfaces

processed with KrF excimer laser radiation. *Biomaterials* **26,** 6780–6787 (2005).

12. Ishida, T., Tonami, K., Araki, K. & Kurosaki, N. Properties of human dentin surface after ArF excimer laser irradiation. *J. Med. Dent. Sci.* **55,** 155–161 (2008).
13. Sivakumar, M., Oliveira, V., Vilar, R. & Rego, A. M. KrF Excimer Laser Ablation of Human Enamel. *Mater. Sci. Forum* **587–588,** 42–46 (2008).
14. Cangueiro, L. T., Vilar, R., Botelho do Rego, A. M. & Muralha, V. S. Femtosecond laser ablation of bovine cortical bone. *J. Biomed. Opt.* **17,** 125005 (2012).
15. Rode, A. V., Gamaly, E. G., Luther-Davies, B., Taylor, B. T., Dawes, J., Chan, A., Lowe, R. M. & Hannaford, P. Subpicosecond laser ablation of dental enamel. *J. Appl. Phys.* **92,** 2153–2158 (2002).
16. Kruger, J., Kautek, W. & Newesely, H. Femtosecond-pulse laser ablation of dental hydroxyapatite and single-crystalline fluoroapatite. *Appl. Phys. A-Materials Sci. Process.* **69,** S403–S407 (1999).
17. Alves, S., Oliveira, V. & Vilar, R. Femtosecond laser ablation of dentin . *J. Phys. D. Appl. Phys.* **45,** 245401 (2012).
18. Ji, L. F., Li, L., Devlin, H., Liu, Z., Jiao, J. & Whitehead, D. Ti:sapphire femtosecond laser ablation of dental enamel, dentine, and cementum. *Lasers Med. Sci.* **27,** 197–204 (2012).
19. Niemz, M. H., Kasenbacher, A., Strassl, M., Backer, A., Beyertt, A., Nickel, D. & Giesen, A. Tooth ablation using a CPA-free thin disk femtosecond laser system. *Appl. Phys. B-Lasers Opt.* **79,** 269–271 (2004).
20. Nicolodelli, G., Lizarelli Rde, F. & Bagnato, V. S. Influence of effective number of pulses on the morphological structure of teeth and bovine femur after femtosecond laser ablation. *J. Biomed. Opt.* **17,** 48001 (2012).
21. Lizarelli, R. F. Z., Kurachi, C., Misoguti, L. & Bagnato, V. S. Characterization of enamel and dentin response to Nd : YAG picosecond laser ablation. *J. Clin. Laser Med. Surg.* **17,** 127–131 (1999).

22. Liu, Y. & Niemz, M. Ablation of femural bone with femtosecond laser pulses - A feasibility study. *Lasers Med. Sci.* **22,** 171–174 (2007).

23. Cangueiro, L. T. & Vilar, R. Influence of the pulse frequency and water cooling on the femtosecond laser ablation of bovine cortical bone. *Appl. Surf. Sci.* **283,** 1012–1017 (2013).

24. Lorenzo, M. C., Portillo, M., Moreno, P., Montero, J., Castillo-Oyague, R., Garcia, A. & Albaladejo, A. In vitro analysis of femtosecond laser as an alternative to acid etching for achieving suitable bond strength of brackets to human enamel. *Lasers Med. Sci.* **29,** 897–905 (2014).

25. Schelle, F., Polz, S., Haloui, H., Braun, A., Dehn, C., Frentzen, M. & Meister, J. Ultrashort pulsed laser (USPL) application in dentistry: basic investigations of ablation rates and thresholds on oral hard tissue and restorative materials. *Lasers Med. Sci.* **29,** 1775–1783 (2014).

26. Pearson, G. J. & Mcdonald, A. V. Invited Review Use of Infrared and Ultra-Violet Lasers in the Removal of Dental Hard-Tissue. *Lasers Med. Sci.* **9,** 227–237 (1994).

27. Hillson, S. *Teeth*. (Cambridge University Press, 2005).

28. Maas, M. C. & Dumont, E. R. Built to last: The structure, function, and evolution of primate dental enamel. *Evol. Anthropol. Issues, News, Rev.* **8,** 133–152 (1999).

29. Imbeni, V., Kruzic, J. J., Marshall, G. W., Marshall, S. J. & Ritchie, R. O. The dentin-enamel junction and the fracture of human teeth. *Nat. Mater.* **4,** 229–232 (2005).

30. Mjor, I. A., Sveen, O. B. & Heyeraas, K. J. Pulp-dentin biology in restorative dentistry. Part 1: normal structure and physiology. *Quintessence Int.* **32,** 427–446 (2001).

31. Pashley, D. H., Walton, R. E. & Slavkin, H. C. in *Endodontics* (eds. Ingle, J. I. & Baklands, L. K.) (BC Decker Inc, 2002).

32. Arana-Chavez, V. E. & Massa, L. F. Odontoblasts: the cells forming and maintaining dentine. *Int. J. Biochem. Cell Biol.* **36,** 1367–1373 (2004).

33. Simmer, J. P. & Fincham, A. G. Molecular mechanisms of dental enamel formation. *Crit. Rev. Oral Biol. Med.* **6,** 84–108 (1995).

34. Kapner, M. Tooth anatomy. Available at:

https://www.nlm.nih.gov/medlineplus/ency/imagepages/1121.htm. (Accessed: 22nd February 2016)

35. LeGeros, R. Z., Bonel, G. & Legros, R. Types of 'H2O' in human enamel and in precipitated apatites. *Calcif. Tissue Res.* **26,** 111–118 (1978).

36. He, L. H. & Swain, M. V. Understanding the mechanical behaviour of human enamel from its structural and compositional characteristics. *J. Mech. Behav. Biomed. Mater.* **1,** 18–29 (2008).

37. Ang, S. F., Saadatmand, M., Swain, M. V, Klocke, A. & Schneider, G. A. Comparison of mechanical behaviors of enamel rod and interrod regions in enamel. *J. Mater. Res.* **27,** 448–456 (2012).

38. Featherstone, J. D. B. & Fried, D. Fundamental Interactions of Lasers with Dental Hard Tissues. *Med. Laser Appl.* **16,** 181–194 (2001).

39. Brown, W. S., Dewey, W. A. & Jacobs, H. R. Thermal properties of teeth. *J. Dent. Res.* **49,** 752–755 (1970).

40. Schneider, G. A., He, L. H. & Swain, M. V. Viscous flow model of creep in enamel. *J. Appl. Phys.* **103,** (2008).

41. Ryou, H., Romberg, E., Pashley, D. H., Tay, F. R. & Arola, D. Importance of age on the dynamic mechanical behavior of intertubular and peritubular dentin. *J. Mech. Behav. Biomed. Mater.* **42,** 229–242 (2015).

42. De Munck, J., Van Meerbeek, B., Yudhira, R., Lambrechts, P. & Vanherle, G. Micro-tensile bond strength of two adhesives to Erbium:YAG-lased vs. bur-cut enamel and dentin. *Eur. J. Oral Sci.* **110,** 322–329 (2002).

43. Bertassoni, L. E., Stankoska, K. & Swain, M. V. Insights into the structure and composition of the peritubular dentin organic matrix and the lamina limitans. *Micron* **43,** 229–236 (2012).

44. Weiner, S., Veis, A., Beniash, E., Arad, T., Dillon, J. W., Sabsay, B. & Siddiqui, F. Peritubular Dentin Formation: Crystal Organization and the Macromolecular Constituents in Human Teeth. *J. Struct. Biol.* **126,** 27–41 (1999).

45. Sherman, V. R., Yang, W. & Meyers, M. A. The materials science of collagen. *J. Mech. Behav. Biomed. Mater.* **52,** 22–50 (2015).

46. Shoulders, M. D. & Raines, R. T. Collagen structure and stability. *Annu. Rev. Biochem.* **78,** 929–958 (2009).

47. Strasser, S., Zink, A., Janko, M., Heckl, W. M. & Thalhammer, S. Structural investigations on native collagen type I fibrils using AFM. *Biochem. Biophys. Res. Commun.* **354,** 27–32 (2007).

48. Kirsch, K. M., Zelickson, B. D., Zachary, C. B. & Tope, W. D. Ultrastructure of collagen thermally denatured by microsecond domain pulsed carbon dioxide laser. *Arch. Dermatol.* **134,** 1255–1259 (1998).

49. Zweig, A. D., Meierhofer, B., Müller, O. M., Mischler, C., Romano, V., Frenz, M. & Weber, H. P. Lateral thermal damage along pulsed laser incisions. *Lasers Surg. Med.* **10,** 262–274 (1990).

50. Bonar, L. C. & Glimcher, M. J. Thermal denaturation of mineralized and demineralized bone collagens. *J. Ultrastruct. Res.* **32,** 545–557 (1970).

51. Wright, N. T. & Humphrey, J. D. Denaturation of collagen via heating: an irreversible rate process. *Annu. Rev. Biomed. Eng.* **4,** 109–128 (2002).

52. Armstrong, S. R., Jessop, J. L. P., Winn, E., Tay, F. R. & Pashley, D. H. Denaturation temperatures of dentin matrices. I. Effect of demineralization and dehydration. *J. Endod.* **32,** 638–641 (2006).

53. Hand, A. R. & Frank, M. E. *Fundamentals of Oral Histology and Physiology*. (Wiley-Blackwell, 2014).

54. Rosan, B. & Lamont, R. J. Dental plaque formation. *Microbes Infect.* **2,** 1599–1607 (2000).

55. Gibbons, R. J. & Houte, J. Van. On the Formation of Dental Plaques. *J. Periodontol.* **44,** 347–360 (1973).

56. Featherstone, J. D. B. Dental caries: a dynamic disease process. *Aust. Dent. J.* **53,** 286–291 (2008).

57. LeGeros, R. Z. Calcium phosphates in demineralization/remineralization processes. *J. Clin.*

Dent. **10,** 65–73 (1999).

58. Cury, J. A. & Tenuta, L. M. A. Enamel remineralization: controlling the caries disease or treating early caries lesions? . *Brazilian Oral Research* **23,** 23–30 (2009).

59. Kuboki, Y., Ohgushi, K. & Fusayama, T. Collagen Biochemistry of the two Layers of Carious Dentin. *J. Dent. Res.* **56,** 1233–1237 (1977).

60. Magalhaes, A. C., Wiegand, A., Rios, D., Honorio, H. M. & Buzalaf, M. A. R. Insights into preventive measures for dental erosion. *J. Appl. Oral Sci.* **17,** 75–86 (2009).

61. Banerjee, A., Watson, T. F. & Kidd, E. A. M. Conservative dentistry: Dentine caries excavation: a review of current clinical techniques. *Br. Dent. J.* **188,** 476–482 (2000).

62. Stephens, R. R. The dental handpiece—a history of its development. *Aust. Dent. J.* **31,** 165–180 (1986).

63. Siegel, S. C. & Von Fraunhofer, J. A. Dental cutting: the historical development of diamond burs. *J. Am. Dent. Assoc.* **129,** 740–745 (1998).

64. Neves, A. A., Coutinho, E., Cardoso, M. V, Lambrechts, P. & Van Meerbeek, B. Current concepts and techniques for caries excavation and adhesion to residual dentin. *J. Adhes. Dent.* **13,** 7–22 (2011).

65. Abd-Elmeguid, A. & Yu, D. C. Dental pulp neurophysiology: part 1. Clinical and diagnostic implications. *J. Can. Dent. Assoc.* **75,** 55–59 (2009).

66. Fried, D., Featherstone, J. D. B., Le, C. Q. & Fan, K. Dissolution studies of bovine dental enamel surfaces modified by high-speed scanning ablation with a lambda = 9.3-μm TEA CO(2) laser. *Lasers Surg. Med.* **38,** 837–845 (2006).

67. Marraccini, T. M., Bachmann, L., Wigdor, H. A., Walsh, J. T. J., Stabholtz, A. & Zezell, D. M. Morphological evaluation of enamel and dentin irradiated with 9.6 μm CO2 and 2.94 μm Er:YAG lasers. *Laser Phys. Lett.* **2,** 551 (2005).

68. Arima, M. & Matsumoto, K. Effects of ArF:excimer laser irradiation on human enamel and dentin. *Lasers Surg. Med.* **13,** 97–105 (1993).

69. Turkmen, C., Gunday, M., Karacorlu, M. & Basaran, B. Effect of CO2, Nd:YAG, and ArF excimer lasers on dentin morphology and pulp chamber temperature: an in vitro study. *J. Endod.* **26,** 644–648 (2000).

70. Van Meerbeek, B., De Munck, J., Yoshida, Y., Inoue, S., Vargas, M., Vijay, P., Van Landuyt, K., Lambrechts, P. & Vanherle, G. Buonocore memorial lecture. Adhesion to enamel and dentin: current status and future challenges. *Operative dentistry* **28,** 215–235 (2003).

71. Stansbury, J. W. Curing dental resins and composites by photopolymerization. *J. Esthet. Dent.* **12,** 300–308 (2000).

72. Buonocore, M. G. A simple method of increasing the adhesion of acrylic filling materials to enamel surfaces. *J. Dent. Res.* **34,** 849–853 (1955).

73. Liu, Y., Tjäderhane, L., Breschi, L., Mazzoni, A., Li, N., Mao, J., Pashley, D. H. & Tay, F. R. Limitations in Bonding to Dentin and Experimental Strategies to Prevent Bond Degradation. *J. Dent. Res.* **90,** 953–968 (2011).

74. Ceballo, L., Toledano, M., Osorio, R., Tay, F. R. & Marshall, G. W. Bonding to Er-YAG-laser-treated dentin. *J. Dent. Res.* **81,** 119–122 (2002).

75. Hashimoto, M., Ohno, H., Kaga, M., Sano, H., Tay, F. R., Oguchi, H., Araki, Y. & Kubota, M. Over-etching effects on micro-tensile bond strength and failure patterns for two dentin bonding systems. *J. Dent.* **30,** 99–105 (2002).

76. Tjäderhane, L., Nascimento, F. D., Breschi, L., Mazzoni, A., Tersariol, I. L. S., Geraldeli, S., Tezvergil-Mutluay, A., Carrilho, M., Carvalho, R. M., Tay, F. R. & Pashley, D. H. Optimizing dentin bond durability: strategies to prevent hydrolytic degradation of the hybrid layer. *Dent. Mater.* **29,** 999–1011 (2013).

77. Mine, A., De Munck, J., Cardoso, M. V., Van Landuyt, K. L., Poitevin, A., Van Ende, A., Matsumoto, M., Yoshida, Y., Kuboki, T., Yatani, H. & Van Meerbeek, B. Dentin-smear remains at self-etch adhesive interface. *Dent. Mater.* **30,** 1147–1153 (2014).

78. De Munck, J., Vargas, M., Iracki, J., Van Landuyt, K., Poitevin, A., Lambrechts, P. & Van

Meerbeek, B. One-day bonding effectiveness of new self-etch adhesives to bur-cut enamel and dentin. *Oper. Dent.* **30,** 39–49 (2005).

79. Wang, Y. & Spencer, P. Analysis of acid-treated dentin smear debris and smear layers using confocal Raman microspectroscopy. *J. Biomed. Mater. Res.* **60,** 300–308 (2002).

80. Pashley, D. H., Tao, L., Boyd, L., King, G. E. & Horner, J. A. Scanning electron microscopy of the substructure of smear layers in human dentine. *Arch. Oral Biol.* **33,** 265–270 (1988).

81. Cardoso, M. V, Coutinho, E., Ermis, R. B., Poitevin, A., Van Landuyt, K., De Munck, J., Carvalho, R. C. R. & Van Meerbeek, B. Influence of dentin cavity surface finishing on micro-tensile bond strength of adhesives. *Dent. Mater.* **24,** 492–501 (2008).

82. Rodriguez-Vilchis, L. E., Contreras-Bulnes, R., Olea-Mejia, O. F., Sanchez-Flores, I. & Centeno-Pedraza, C. Morphological and structural changes on human dental enamel after Er:YAG laser irradiation: AFM, SEM, and EDS evaluation. *Photomed. Laser Surg.* **29,** 493–500 (2011).

83. Nishimoto, Y., Otsukii, M., Yamauti, M., Eguchi, T., Sato, Y., Foxton, R. M. & Tagami, J. Effect of pulse duration of Er : YAG laser on dentin ablation. *Dent. Mater. J.* **27,** 433–439 (2008).

84. Bertrand, M.-F., Semez, G., Leforestier, E., Muller-Bolla, M., Nammour, S. & Rocca, J.-P. Er:YAG laser cavity preparation and composite resin bonding with a single-component adhesive system: relationship between shear bond strength and microleakage. *Lasers Surg. Med.* **38,** 615–623 (2006).

85. Ramos, R. P., Chimello, D. T., Chinelatti, M. A., Nonaka, T., Pecora, J. D. & Palma Dibb, R. G. Effect of Er:YAG laser on bond strength to dentin of a self-etching primer and two single-bottle adhesive systems. *Lasers Surg. Med.* **31,** 164–170 (2002).

86. Dunn, W. J., Davis, J. T. & Bush, A. C. Shear bond strength and SEM evaluation of composite bonded to Er:YAG laser-prepared dentin and enamel. *Dent. Mater.* **21,** 616–624 (2005).

87. Portillo, M., Lorenzo, M. C., Moreno, P., García, A., Montero, J., Ceballos, L., Fuentes, M. V & Albaladejo, A. Influence of Er:YAG and Ti:sapphire laser irradiation on the microtensile bond strength of several adhesives to dentin. *Lasers Med. Sci.* **30,** 483–492 (2015).

88. Aoki, A., Ishikawa, I., Yamada, T., Otsuki, M., Watanabe, H., Tagami, J., Ando, Y. & Yamamoto, H. Comparison between Er:YAG laser and conventional technique for root caries treatment in vitro. *J. Dent. Res.* **77,** 1404–1414 (1998).

89. Iida, Y., Tanaka, H., Sugimoto, H. & Kanno, Y. KrF Excimer Laser Ablation of Al2O3 and Al2O3 –TiC Ceramics. *Jpn. J. Appl. Phys.* **47,** 1068 (2008).

90. Cranton, W. M., Key, P. H., Sands, D., Thomas, C. B. & Wagner, F. X. XeCl laser ablation of thin film ZnS. *Appl. Surf. Sci.* **96,** 501–504 (1996).

91. Perry, M. D., Stuart, B. C., Banks, P. S., Feit, M. D., Yanovsky, V. & Rubenchik, A. M. Ultrashort-pulse laser machining of dielectric materials. *J. Appl. Phys.* **85,** (1999).

92. Backus, S., Durfee, C. G., Murnane, M. M. & Kapteyn, H. C. High power ultrafast lasers. *Rev. Sci. Instrum.* **69,** 1207–1223 (1998).

93. Christensen, B. H. & Balling, P. Modeling ultrashort-pulse laser ablation of dielectric materials. *Phys. Rev. B* **79,** 155424 (2009).

94. Balling, P. & Schou, J. Femtosecond-laser ablation dynamics of dielectrics: basics and applications for thin films. *Reports Prog. Phys.* **76,** 36502 (2013).

95. Gamaly, E. G., Rode, A. V, Luther-Davies, B. & Tikhonchuk, V. T. Ablation of solids by femtosecond lasers: Ablation mechanism and ablation thresholds for metals and dielectrics. *Phys. Plasmas* **9,** 949–957 (2002).

96. Anisimov, S. I.; Kapeliovich, B. L.; Perelman, T. L. Electron emission from metal surfaces exposed to ultrashort laser pulses. *Sov. Phys.-JETP* **39,** 375–377 (1974).

97. Bulgakova, N. M., Stoian, R., Rosenfeld, A., Hertel, I. V & Campbell, E. E. B. Electronic transport and consequences for material removal in ultrafast pulsed laser ablation of materials. *Phys. Rev. B* **69,** 54102 (2004).

98. Stoian, R., Ashkenasi, D., Rosenfeld, A. & Campbell, E. E. B. Coulomb explosion in ultrashort pulsed laser ablation of Al2O3. *Phys. Rev. B* **62,** 13167–13173 (2000).

99. Bulgakova, N. M., Burakov, I. M., Meshcheryakov, Y. P., Stoian, R., Rosenfield, A. & Hertel, I. V.

Theoretical Models and Qualitative Interpretations of Fs Laser Material Processing. *J. Laser Micro/Nanoengineering* **2,** 76–86 (2007).

100. Stoian, R., Rosenfeld, A., Ashkenasi, D., Hertel, I. V, Bulgakova, N. M. & Campbell, E. E. B. Surface Charging and Impulsive Ion Ejection during Ultrashort Pulsed Laser Ablation. *Phys. Rev. Lett.* **88,** 97603 (2002).
101. Zhigilei, L. V & Garrison, B. J. Microscopic mechanisms of laser ablation of organic solids in the thermal and stress confinement irradiation regimes. *J. Appl. Phys.* **88,** 1281–1298 (2000).
102. Vogel, A., Linz, N., Freidank, S. & Paltauf, G. Femtosecond-Laser-Induced Nanocavitation in water: Implications for optical breakdown threshold and cell surgery. *Phys. Rev. Lett.* **100,** 38102 (2008).
103. Zhigilei, L. V, Lin, Z. & Ivanov, D. S. Atomistic modeling of short pulse laser ablation of metals: connections between melting, spallation, and phase explosion. *J. Phys. Chem. C* **113,** 11892–11906 (2009).
104. Vogel, A. & Venugopalan, V. Mechanisms of pulsed laser ablation of biological tissues. *Chem. Rev.* **103,** 2079 (2003).
105. Semaltianos, N. G., Perrie, W., French, P., Sharp, M., Dearden, G., Logothetidis, S. & Watkins, K. G. Femtosecond laser ablation characteristics of nickel-based superalloy C263. *Appl. Phys. A* **94,** 999–1009 (2008).
106. Jee, Y., Becker, M. F. & Walser, R. M. Laser-induced damage on single-crystal metal surfaces. *J. Opt. Soc. Am. B* **5,** 648–659 (1988).
107. Cangueiro, L., Le, Q.-T. & Vilar, R. in *Laser Surface Modification of Biomaterials: Techniques and Applications* (ed. Vilar, R.) (Woodhead Publishing, 2016).
108. Srinivasan, R. in *Laser Processing and Diagnostics* (ed. Bäuerle, D.) 343–354 (Springer Berlin Heidelberg, 1984).
109. Vogel, A., Noack, J., Hüttman, G. & Paltauf, G. Mechanisms of femtosecond laser nanosurgery of cells and tissues. *Appl. Phys. B* **81,** 1015–1047 (2005).

110. Serrano, J., Moros, J. & Laserna, J. J. Molecular signatures in femtosecond laser-induced organic plasmas: comparison with nanosecond laser ablation. *Phys. Chem. Chem. Phys.* **18,** 2398–2408 (2016).

111. Hovhannisyan, V., Lo, W., Hu, C., Chen, S.-J. & Dong, C. Y. Dynamics of femtosecond laser photo-modification of collagen fibers. *Opt. Express* **16,** 7958–7968 (2008).

112. Lizarelli, R. F., Kurachi, C., Misoguti, L. & Bagnato, V. S. A comparative study of nanosecond and picosecond laser ablation in enamel: morphological aspects. *J. Clin. laser Med. Surg.* **18,** 151–157 (2000).

113. Chan, A., Rode, A., Gamaly, E., Luther-Davies, B., Taylor, B., Dawes, J., Lowe, M. & Hannaford, P. Ablation of dental enamel using subpicosecond pulsed lasers. *Lasers Dent. Proc.* **1248,** 117–119489 (2003).

114. Neev, J., DaSilva, L. B., Feit, M. D., Perry, M. D., Rubenchik, A. M. & Stuart, B. C. Ultrashort pulse lasers for hard tissue ablation. *IEEE J. Sel. Top. Quantum Electron.* **2,** 790–800 (1996).

115. Rode, A. V, Gamaly, E. G., Luther-Davies, B., Taylor, B. T., Graessel, M., Dawes, J. M., Chan, A., Lowe, R. M. & Hannaford, P. Precision ablation of dental enamel using a subpicosecond pulsed laser. *Aust. Dent. J.* **48,** 233–239 (2003).

116. Domke, M., Gavrilova, A., Rapp, S., Frentzen, M., Meister, J. & Huber, H. P. Time-resolved microscopy reveals the driving mechanism of particle formation during ultrashort pulse laser ablation of dentin-like ivory. *J. Biomed. Opt.* **20,** 76005 (2015).

117. Bello-Silva, M. S., Wehner, M., Eduardo, C. de P., Lampert, F., Poprawe, R., Hermans, M. & Esteves-Oliveira, M. Precise ablation of dental hard tissues with ultra-short pulsed lasers. Preliminary exploratory investigation on adequate laser parameters. *Lasers Med. Sci.* **28,** 171–184 (2013).

118. Martin, S., Hertwig, A., Lenzner, M., Krüger, J. & Kautek, W. Spot-size dependence of the ablation threshold in dielectrics for femtosecond laser pulses. *Appl. Phys. A* **77,** 883–884 (2003).

119. Domke, M., Wick, S., Laible, M., Rapp, S., Kutnesova, J., Homann, C., Huber, H. P. & Sroka L. and Sroka, R., R. E. D.-L. Investigations of the damage mechanisms during ultrashort pulse laser ablation of dental tissue. in *Proc. SPIE 9542, Medical Laser Applications and Laser-Tissue Interactions VII, 95420Q* (Optical Society of America, 2015).

120. Bello - Silva, M. S. Evaluation of dental hard tissues irradiated with ultra-short pulsed lasers Influence on surface morphology and microtensile bond strength. (Rheinisch-Westfälischen Technischen Hochschule Aachen, 2010).

121. Shaheen, M. E., Gagnon, J. E. & Fryer, B. J. Evaluation of ablation efficiency and surface morphology of human teeth upon irradiation with femtosecond laser pulses. *Laser Phys.* **24,** 116001 (2014).

122. Yalçin, M., Barutcigil, Ç., Sisman, R., Yavuz, T. & Oruçoglu, H. Evaluation of the sealing ability of pulp capping agents against leakage on direct pulp capping with a computerized fluid filtration meter. *J. Restor. Dent.* **2,** 46–50 (2014).

123. Liu, J. M. Simple technique for measurements of pulsed Gaussian-beam spot sizes. *Opt. Lett.* **7,** 196–198 (1982).

124. Fried, D., Ashouri, N., Breunig, T. & Shori, R. Mechanism of water augmentation during IR laser ablation of dental enamel. *Lasers Surg. Med.* **31,** 186–193 (2002).

125. Colucci, V., Lucisano Botelho do Amaral, F., Pécora, J. D., Palma-Dibb, R. G. & Milori Corona, S. A. Water flow on erbium:yttrium–aluminum–garnet laser irradiation: effects on dental tissues. *Lasers Med. Sci.* **24,** 811–818 (2009).

126. Lloyd, G. E. Atomic number and crystallographic contrast images with the SEM: a review of backscattered electron techniques. *Mineral. Mag.* **359,** 3–19 (1987).

127. Cullity, B. D. *Elements of X-ray Diffraction*. (Addison-Wesley Publishing Company, 1978).

128. Birkholz, M. in *Thin Film Analysis by X-Ray Scattering* 143–182 (Wiley-VCH Verlag GmbH & Co. KGaA, 2005). doi:10.1002/3527607595.ch4

129. Hubbell, J. H. & Seltzer, S. M. Tables of X-Ray Mass Attenuation Coefficients and Mass Energy-

Absorption Coefficients (version 1.4). (2004). Available at: https://www.nist.gov/pml/x-ray-mass-attenuation-coefficients.

130. Meng, Z., Yao, X. S., Yao, H., Liang, Y., Liu, T., Li, Y., Wang, G. & Lan, S. Measurement of the refractive index of human teeth by optical coherence tomography. *J. Biomed. Opt.* **14,** 34010 (2009).

131. Munoz, M. A., Luque, I., Hass, V., Reis, A., Loguercio, A. D. & Bombarda, N. H. C. Immediate bonding properties of universal adhesives to dentine. *J. Dent.* **41,** 404–411 (2013).

132. Schneider, C. A., Rasband, W. S. & Eliceiri, K. W. NIH Image to ImageJ: 25 years of image analysis. *Nat. Methods* **9,** 671–675 (2012).

133. Fowler, B. O. & Kuroda, S. Changes in Heated and in Laser-Irradiated Human Tooth Enamel and Their Probable Effects on Solubility. *Calcif. Tissue Int.* **38,** 197–208 (1986).

134. Kuroda, S. & Fowler, B. O. Compositional, structural, and phase changes in in vitro laser-irradiated human tooth enamel. *Calcif. Tissue Int.* **36,** 361–369 (1984).

135. Kivrak, N. & Taş, A. C. Synthesis of Calcium Hydroxyapatite-Tricalcium Phosphate (HA-TCP) Composite Bioceramic Powders and Their Sintering Behavior. *J. Am. Ceram. Soc.* **81,** 2245–2252 (1998).

136. Weinlaender, M., Beumer III, J., Kenney, E. B., Moy, P. K. & Adar, F. Raman microprobe investigation of the calcium phosphate phases of three commercially available plasma-flame-sprayed hydroxyapatite-coated dental implants. *J. Mater. Sci. Mater. Med.* **3,** 397–401 (1992).

137. Mihály, J., Gombás, V., Afishah, A. & Mink, J. FT-Raman investigation of human dental enamel surfaces. *J. Raman Spectrosc.* **40,** 898–902 (2009).

138. Penel, G., Delfosse, C., Descamps, M. & Leroy, G. Composition of bone and apatitic biomaterials as revealed by intravital Raman microspectroscopy. *Bone* **36,** 893–901 (2005).

139. Miro, S., Costantini, J. M., Bardeau, J. F., Chateigner, D., Studer, F. & Balanzat, E. Raman spectroscopy study of damage induced in fluorapatite by swift heavy ion irradiations. *J. Raman Spectrosc.* **42,** 2036–2041 (2011).

140. Saber-Samandari, S., Alamara, K., Saber-Samandari, S. & Gross, K. A. Micro-Raman spectroscopy shows how the coating process affects the characteristics of hydroxylapatite. *Acta Biomater.* **9,** 9538–9546 (2013).

141. Oraevsky, A. A., Da Silva, L. B., Rubenchik, A. M., Feit, M. D., Glinsky, M. E., Perry, M. D., Mammini, B. M., Small, W. & Stuart, B. C. Plasma mediated ablation of biological tissues with nanosecond-to-femtosecond laser pulses: relative role of linear and nonlinear absorption. *IEEE Journal of Selected Topics in Quantum Electronics* **2,** 801–809 (1996).

142. Rehman, I. & Bonfield, W. Characterization of hydroxyapatite and carbonated apatite by photo acoustic FTIR spectroscopy. *J. Mater. Sci. Mater. Med.* **8,** 1–4 (1997).

143. Paschalis, E. P., DiCarlo, E., Betts, F., Sherman, P., Mendelsohn, R. & Boskey, A. L. FTIR microspectroscopic analysis of human osteonal bone. *Calcif. Tissue Int.* **59,** 480–487 (1996).

144. Gadaleta, S. J., Paschalis, E. P., Betts, F., Mendelsohn, R. & Boskey, A. L. Fourier transform infrared spectroscopy of the solution-mediated conversion of amorphous calcium phosphate to hydroxyapatite: new correlations between X-ray diffraction and infrared data. *Calcif. Tissue Int.* **58,** 9–16 (1996).

145. Combes, C. & Rey, C. Amorphous calcium phosphates: synthesis, properties and uses in biomaterials. *Acta Biomater.* **6,** 3362–3378 (2010).

146. Skrtic, D., Antonucci, J. M. & Eanes, E. D. Amorphous Calcium Phosphate-Based Bioactive Polymeric Composites for Mineralized Tissue Regeneration. *J. Res. Natl. Inst. Stand. Technol.* **108,** 167–182 (2003).

147. Zezell, D. M., Ana, P. A., Pereira, T. M., Correa, P. R. & Velloso, W. J. in *Developments in Heat Transfer* (ed. Bernardes, M. A. D. S.) 227–246 (InTech, 2011).

148. Perdigao, J., Lambrechts, P., van Meerbeek, B., Tome, A. R., Vanherle, G. & Lopes, A. B. Morphological field emission-SEM study of the effect of six phosphoric acid etching agents on human dentin. *Dent. Mater.* **12,** 262–271 (1996).

149. Markovic, M., Fowler, B. O. & Tung, M. S. Preparation and Comprehensive Characterization of

a Calcium Hydroxyapatite Reference Material. *J. Res. Natl. Inst. Stand. Technol.* **109,** 553–568 (2004).

150. Bertacci, A., Lucchese, A., Taddei, P., Gherlone, E. F. & Chersoni, S. Enamel structural changes induced by hydrochloric and phosphoric acid treatment. *J. Appl. Biomater. Funct. Mater.* **12,** 240–247 (2014).

151. Bozec, L. & Odlyha, M. Thermal Denaturation Studies of Collagen by Microthermal Analysis and Atomic Force Microscopy. *Biophys. J.* **101,** 228–236 (2011).

152. Cecchini, R. C. M., Zezell, D. M., Oliveira, E., Freitas, P. M. & Eduardo, C. P. Effect of Er:YAG laser on enamel acid resistance: morphological and atomic spectrometry analysis. *Lasers Surg. Med.* **37,** 366–372 (2005).

153. Fox, J. L., Yu, D., Otsuka, M., Higuchi, W. I., Wong, J. & Powell, G. L. Initial dissolution rate studies on dental enamel after CO2 laser irradiation. *J. Dent. Res.* **71,** 1389–1398 (1992).

154. Almeida, R. M. & Pantano, C. G. Structural investigation of silica gel films by infrared spectroscopy. *J. Appl. Phys.* **68,** (1990).

155. Chang, M. C. & Tanaka, J. FT-IR study for hydroxyapatite/collagen nanocomposite cross-linked by glutaraldehyde. *Biomaterials* **23,** 4811–4818 (2002).

156. Van Meerbeek, B., Mohrbacher, H., Celis, J. P., Roos, J. R., Braem, M., Lambrechts, P. & Vanherle, G. Chemical Characterization of the Resin-Dentin Interface by Micro-Raman Spectroscopy. *J. Dent. Res.* **72,** 1423–1428 (1993).

157. Van Meerbeek, B., Inokoshi, S., Braem, M., Lambrechts, P. & Vanherle, G. Morphological aspects of the resin-dentin interdiffusion zone with different dentin adhesive systems. *J. Dent. Res.* **71,** 1530–1540 (1992).

158. Armstrong, S. R., Keller, J. C. & Boyer, D. B. Mode of failure in the dentin-adhesive resin-resin composite bonded joint as determined by strength-based (muTBS) and fracture-based (CNSB) mechanical testing. *Dent. Mater.* **17,** 201–210 (2001).

159. Scherrer, S. S., Cesar, P. F. & Swain, M. V. Direct comparison of the bond strength results of the

different test methods: a critical literature review. *Dent. Mater.* **26,** e78-93 (2010).

160. Bonse, J., Sturm, H., Schmidt, D. & Kautek, W. Chemical, morphological and accumulation phenomena in ultrashort-pulse laser ablation of TiN in air. *Appl. Phys. A* **71,** 657–665 (2000).

161. Raciukaitis, G., Brikas, M., Gecys, P. & Gedvilas, M. Accumulation effects in laser ablation of metals with high-repetition-rate lasers. in *SPIE 7005, High-Power Laser Ablation VII, 70052L* **7005,** (2008).

162. Stuart, B. C., Feit, M. D., Herman, S., Rubenchik, A. M., Shore, B. W. & Perry, M. D. Nanosecond-to-femtosecond laser-induced breakdown in dielectrics. *Phys. Rev. B* **53,** 1749–1761 (1996).

163. Sanner, N., Utéza, O., Bussiere, B., Coustillier, G., Leray, A., Itina, T. & Sentis, M. Measurement of femtosecond laser-induced damage and ablation thresholds in dielectrics. *Appl. Phys. A* **94,** 889–897 (2009).

164. Mayer, I., Schneider, S., Sydney-Zax, M. & Deutsch, D. Thermal decomposition of developing enamel. *Calcif. Tissue Int.* **46,** 254–257 (1990).

165. Holcomb, D. W. & Young, R. A. Thermal decomposition of human tooth enamel. *Calcif. Tissue Int.* **31,** 189–201 (1980).

166. Le, Q.-T., Bertrand, C. & Vilar, R. Femtosecond laser ablation of enamel. *J. Biomed. Opt.* **21,** 65005 (2016).

167. Heimann, R. B. & Wirth, R. Formation and transformation of amorphous calcium phosphates on titanium alloy surfaces during atmospheric plasma spraying and their subsequent in vitro performance. *Biomaterials* **27,** 823–831 (2006).

168. Ben-Yakar, A. & Byer, R. L. Femtosecond laser ablation properties of borosilicate glass. *J. Appl. Phys.* **96,** 5316–5323 (2004).

169. Engelbach, C., Dehn, C., Bourauel, C., Meister, J. & Frentzen, M. Ablation of carious dental tissue using an ultrashort pulsed laser (USPL) system. *Lasers Med. Sci.* **30,** 1427–1434 (2015).

170. Niemz, M. H. *Laser Tissue Interactions: Fundamentals and Application*. (Springer Berlin Heidelberg, 2007).

171. Zach, L. & Cohen, G. Pulp response to externally applied heat. *Oral Surg. Oral Med. Oral Pathol.* **19,** 515–530 (1965).

172. Baldissara, P., Catapano, S. & Scotti, R. Clinical and histological evaluation of thermal injury thresholds in human teeth: a preliminary study. *J. Oral Rehabil.* **24,** 791–801 (1997).

173. Pike, P., Parigger, C., Splinter, R. & Lockhart, P. Temperature distribution in dental tissue after interaction with femtosecond laser pulses. *Appl. Opt.* **46,** 8374–8378 (2007).

174. Chang, K. P., Tsai, T. W., Huang, K. Y., Huang, C. H., Wang, S. Y., Cheng, C. W., Chen, J. K. & Tzou, D. Y. Thermal response of a dental tissue induced by femtosecond laser pulses. *Appl. Opt.* **52,** 6626–6635 (2013).

175. Lin, M., Luo, Z. Y., Bai, B. F., Xu, F. & Lu, T. J. Fluid Mechanics in Dentinal Microtubules Provides Mechanistic Insights into the Difference between Hot and Cold Dental Pain. *PLoS One* **6,** e18068 (2011).

176. Koshiro, K., Sidhu, S. K., Inoue, S., Ikeda, T. & Sano, H. New concept of resin-dentin interfacial adhesion: the nanointeraction zone. *J. Biomed. Mater. Res. B. Appl. Biomater.* **77,** 401–408 (2006).

177. Ermis, R. B., De Munck, J., Cardoso, M. V., Coutinho, E., Van Landuyt, K. L., Poitevin, A., Lambrechts, P. & Van Meerbeek, B. Bond strength of self-etch adhesives to dentin prepared with three different diamond burs. *Dent. Mater.* **24,** 978–985 (2017).

178. Van Meerbeek, B., Peumans, M., Poitevin, A., Mine, A., Van Ende, A., Neves, A. & De Munck, J. Relationship between bond-strength tests and clinical outcomes. *Dent. Mater.* **26,** e100-21 (2010).

179. Hovhannisyan, V., Ghazaryan, A., Chen, Y.-F., Chen, S.-J. & Dong, C.-Y. Photophysical mechanisms of collagen modification by 80 MHz femtosecond laser. *Opt. Express* **18,** 24037–24047 (2010).

180. Eugenio, S., Osorio, R., Sivakumar, M., Vilar, R., Monticelli, F. & Toledano, M. Bond strength of an etch-and-rinse adhesive to KrF excimer laser-treated dentin. *Photomed. Laser Surg.* **28,**

97–102 (2010).

181. Visuri, S. R., Walsh, J. T. & Wigdor, H. A. Erbium laser ablation of dental hard tissue: Effect of water cooling. *Lasers Surg. Med.* **18,** 294–300 (1996).

182. Lee, B. S., Hung, Y. L. & Lan, W. H. Compositional and morphological changes of human dentin after Er : YAG laser irradiation. *Lasers Dent. Proc.* **1248,** 143–152489 (2003).

183. Delme, K. I. M., Cardoso, M. V., Mine, A., De Moor, R. J. G. & Van Meerbeek, B. Transmission electron microscopic examination of the interface between a resin-modified glass-ionomer and Er:YAG laser-irradiated dentin. *Photomed. Laser Surg.* **27,** 317–323 (2009).

184. Staninec, M., Meshkin, N., Manesh, S. K., Ritchie, R. O. & Fried, D. Weakening of dentin from cracks resulting from laser irradiation. *Dent. Mater.* **25,** 520–525 (2009).

Appendix

Table A-1: The shear bond strength values (MPa) obtained with the tested treatment conditions and with the self-etch adhesive Adhese Universal® (Ivoclar Vivadent ©, Lieschtenstein).

Burr (MPa)	Burr + etching (MPa)	2 J/cm² (MPa)	2 J/cm² + etching (MPa)	14 J/cm² (MPa)	14 J/cm² + etching (MPa)
5.61	12.74	8.50	8.94	13.28	16.75
13.76	8.87	10.19	10.70	15.24	10.19
12.74	10.19	7.75	16.10	11.60	15.29
10.7	10.7	5.12	20.20	12.54	19.87
5.66	9.68	12.80	10.20	10.19	13.10
3.57	17.32	15.29	11.16	11.21	19.87
8.92	16.56	20.10	15.10	8.60	16.38
8.90	20.38	17.35	9.81	13.45	18.33
12.74	6.37	9.61	10.10	15.44	12.37
12.79	9.68	9.37	15.95	14.11	10.75